Microstructural analysis of coal-bearing deformation bands at Wangaloa, New Zealand

MASTER THESIS

BASIN AND RESERVOIR STUDIES

REBECCA ERTESVÅG

DEPARTMENT OF EARTH SCIENCE

UNIVERSITY OF BERGEN

November, 2021

Abstract

Deformation bands are defined as tabular, millimeter to centimeter wide zones of localized strain that commonly form in porous granular rock. Deformation bands have been studied in great detail over the last four decades and are known to potentially influence the fluid flow in reservoirs. This MSc thesis attempts to characterize deformation bands with coal entrainment in siliciclastic sandstones from the Taratu Formation at Wangaloa Beach, SE New Zealand. Two sample sets were collected; sample set 1 along a deformation band cluster, with samples collected at different increments of cluster thickness, sample set 2 along two single deformation bands with samples collected at different increments of displacement. Results from extensive analysis of microscopic observations were used to determine the controlling factors on deformation mechanisms/kinematics and the microstructural evolution, as well as the microstructures of the coal and its effect on fluid flow. The main observations in both sample sets are: i) visibly reduced grain size inside the deformation band, ii) high number of survival grains inside the deformation bands, with main fracture mechanism being grain flaking and intragranular fractures. Increased pore space is observed inside the deformation bands of sample set 1 while decreased pore space is observed inside deformation bands of sample set 2. These findings suggest that the deformation mechanisms in both sample sets are an interplay between particulate flow and cataclasis. The deformation bands in sample set 1 are kinematically classified as dilatant shear bands, while deformation bands in sample set 2 are classified as compactional shear bands. Pore filling authigenic clay is present in all samples, with preferential precipitation in the host rock. This greatly affects the porosity measurements and is suggested to contribute to the increased porosity in the bands of sample set 1. Mm-thin coal seams are smeared by the deformation bands, reaching displacements up to 20 mm. BSE-SEM images reveal that the coal mainly fractures in a brittle manner depending on the coal maceral, which can result in an extensive fracture network. Increased pore space caused by volume shrinkage of the coal during burial is observed surrounding the coal fragments. These findings result in higher porosity inside the deformation band where coal is present. The coal in this study is therefore concluded to have little influence on fluid flow and does not have the same sealing potential as a clay smear. This study can contribute to a better understanding of fluid flow in reservoirs, as little mentioning of coal entrainment in deformation bands are found in the literature. That can be of relevance to projects related to production of hydrocarbons in reservoirs, CO_2 storage, groundwater aquifers and geothermal reservoirs.

Acknowledgements

This thesis is part of my MSc degree in structural geology at the Department of Earth Science, University of Bergen. It was made possible by the help and contributions of several people that I would like to express my deepest gratitude towards. First and foremost, I would like to thank my main supervisor Prof. Atle Rotevatn for exceptional guidance and support throughout my thesis work. Covid kept us apart, but we still had inspiring discussions over Zoom and you kept me motivated and focused throughout these unusual times.

I would also like to express my sincere gratitude to my co-supervisors Dr. Steven Smith at the University of Otago for the valuable help with my field work and Matteo Demurtas at the University of Bergen for providing new perspectives and taking your time to read through my work. Both of your help is highly valued and appreciated

Other people at the University of Otago that deserve praise are Brent Pooley for preparing excellent thin sections for this study and Dr. Marianne Negrini for her guidance in the Scanning Electron Microscope and helping me with digital image analysis using ImageJ. I also send my thanks to Tilly Hill for letting me rent her room during my stay in Dunedin.

A special thanks to Irene Heggestad and Leif-Eirk Rydland Pedersen for assistance regarding the Scanning Electron Microscope and optical microscope in Bergen. Thank you to Knut Ringen Viten for assisting me with making figures in Rstudio and thank you to Anita Torabi for providing assistance with exceedance frequency plots.

Last but not least, I would like to thank my friends and family for excellent support and motivation through these two long years. Sitting at home alone and writing a thesis can be hard and unmotivating, but friends and family have kept me focused and cheered me up when needed. I appreciate you all.

Rebecca Ertesvåg

Klepp, November 2021

Contents

1. Introduction

1.1 Rationale

Deformation bands are defined as tabular, millimeter to centimeter wide zones of localized strain that form in porous granular rock (e.g., Aydin, 1978; Antonellini et al., 1994, Fossen et al., 2007). Deformation bands in siliciclastic sandstones have been extensively researched (Fossen et al., 2007; and references therein) since they were first described by Aydin (1978) in the Entrada and Navajo Sandstone in the San Rafael Desert, Utah (USA). They can occur as single structures or in clusters of deformation bands (Fossen et al., 2007; Nicols et al., 2013). The evolution and microstructure of deformation bands has been of particular interest as deformation bands can provide important information on how faults form in porous sandstones. Deformation bands also tend to have enhanced cohesion and reduced permeability and porosity, thus having the potential to influence fluid flow in reservoirs (Fisher and Knipe, 2001; Sternlof et al., 2006; Fossen and Bale, 2007; Fossen et al., 2007; Rotevatn et al., 2013; Ogilvie et al., 2001). However, deformation bands show large spatial variation moving along dip of permeability and porosity, hence their significance to reservoir productivity is not yet fully understood. Over the last decades there has been more studies on the spatial variation of deformation bands (e.g., Antonellini et al., 1994; Torabi and Fossen, 2009; Ballas et al., 2015). Image analysis of photomicrographs from thin sections comparing host rock and deformation bands have been a useful tool in characterizing the microstructures and evolution of different deformation bands (Rotevatn et al., 2008; Torabi and Fossen, 2009; Elphick et al., 2021). Studies have shown that deformation bands are sensitive to lithological differences in the host rock (Fossen et al., 2007; Torabi and Fossen, 2009). This thesis will attempt to build on the previous knowledge on microstructures in deformation bands, with particular focus on comparing porosity and particle size distribution inside deformation bands and the host rock to classify and understand the deformation mechanisms of the deformation bands. Coal is present in the samples and are found to be entrained and sheared by the deformation bands. No studies, to my knowledge, have addressed how coal entrainment in deformation bands influences the microstructure and porosity of the bands. As coal is commonly found in sandstone reservoirs (Souvick and Corbin, 2001) it can be valuable to know if coal in deformation bands behaves similar as a clay smear in order to more carefully predict fluid flow.

1.2 Aim

The main aim of this thesis is to investigate the changes in microstructures in deformation bands by using thin section analysis to compare the spatial variation of the host rock and deformation bands along a single structure of deformation bands and a cluster of deformation bands. Specifically, the thesis aims to: (i) describe the lithological characteristics of the host rock and deformation band, (ii) determine the changes in particle size distribution and porosity at different increments of displacement of a single structure and at different increments of thickness of a deformation band cluster, (iii) classify the deformation bands based on the main deformation mechanisms and their kinematics, as well as determine how the deformation bands formed, (iiii) investigate the influence of coal entrainment in deformation bands, and how it may affect fluid flow. The aims mentioned above will be reached by the following objectives:

- Collect samples at different increments of displacement and thickness in order to evaluate the effect of displacement and thickness on the evolution of microstructures
- Analyse the samples by using a standard optical microscope and a scanning electron microscope to determine microstructural and lithological characteristics
- Quantitatively assess and compare the particle size distribution and porosity in host rock with the deformation band, and how they evolve along the band and cluster of bands.
- Analyse the characteristics of coal inside and outside of the deformation band and determine its effect on porosity.

1.3 Study area

The study area is located at Wangaloa Beach, south of Dunedin on the eastern side of the South Island in New Zealand (Fig. 1). New Zealand is situated on the boundary between the Australian and Pacific Plate. The Pacific Plate is subducting beneath the Australian Plate in the north and the Australian Plate is subducting beneath the Pacific Plate in the South (Fig. 1a). In between the two subduction zones the plates are sliding past each other along the Alpine Fault in the South Island (King, 2000; Ballance, 2009; Wallace et al., 2012). The South Island consists of fault-bounded terranes from Late Palaeozoic-Mesozoic that make up the basement rock and sedimentary cover rocks that is recording a transgressive-regressive sequence from Mid-Cretaceous to present times (Wandres and Bradshaw, 2005; Mortimer et al., 2014; Robertson et al., 2019). Several NE-SW and NW-SE trending faults are located along the coast south of

Dunedin, with the Titri Fault, Akatore Fault and Livingstone Fault being the largest (Fig. 1b)(Bishop and Turnbull, 1996) The studied deformation bands are found in the Taratu Formation at Wangaloa Beach (Fig. 1c). The Taratu Formation represents a transgressive period in the sedimentary cover rocks and can be studied in detail along the coast, both south and north of Dunedin.

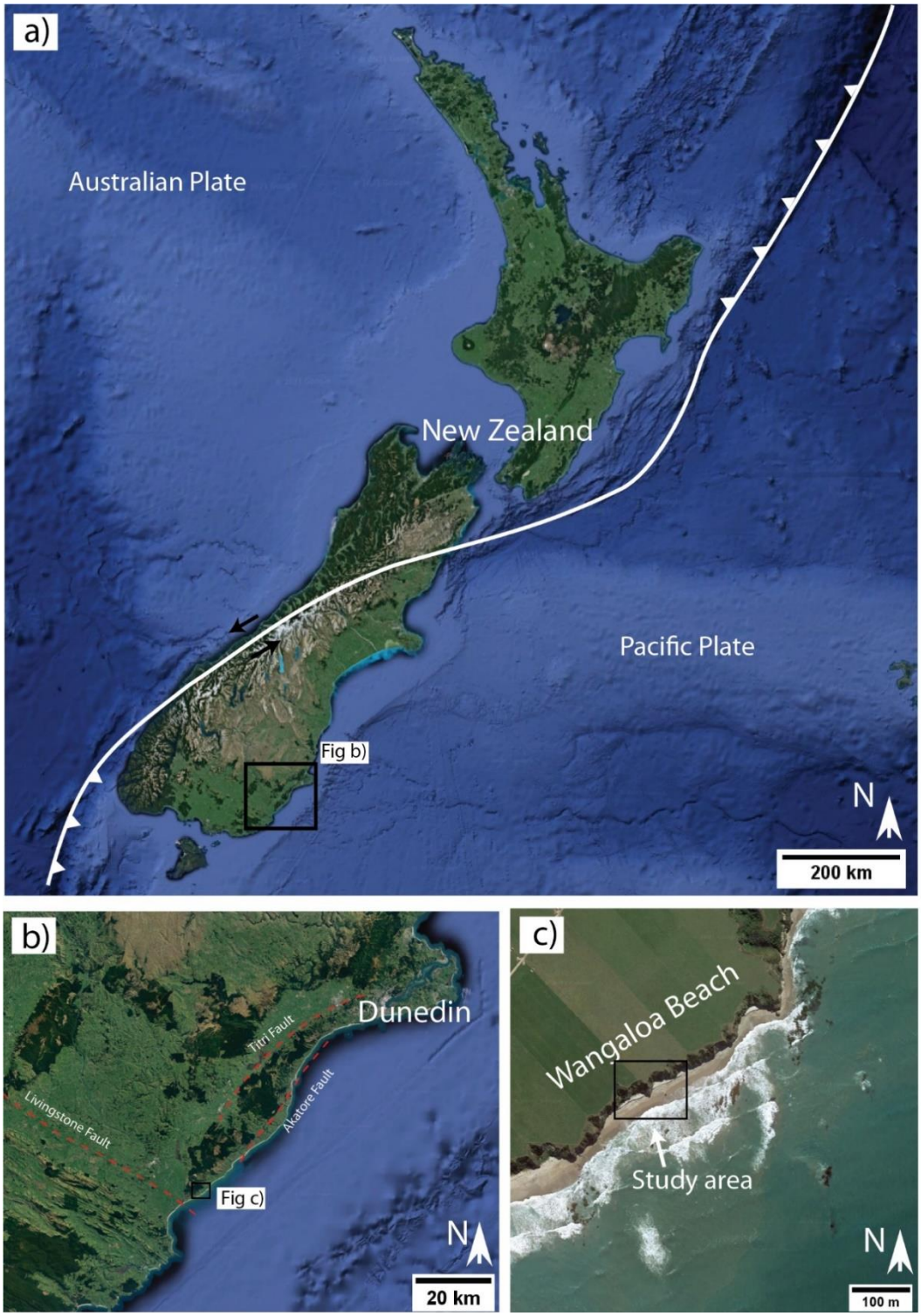

Figure 1.1: a) Satellite image of New Zealand with the plate boundary highlighted, b) Satellite image of the coast south of Dunedin. Main faults in area are marked, c) Satellite image pointing out study area at Wangaloa Beach. Image courtesy of Google Earth.

2 Theoretical background

The focus of this chapter is to introduce the theory, concepts, and terminology of deformation bands in porous rocks as well as a short introduction to coal. The first part of the chapter will present the characteristics of deformation bands, in particular how they are classified and formed based on different kinematics and their main deformation mechanism. The second part will elaborate on deformation bands and their significance to fault growth and fluid flow in reservoirs. The last part will provide some background knowledge on the formation and classification of coal.

2.1 Deformation bands

Deformation bands are a common type of strain localization in deformed porous sandstones and sediments (Fossen and Bale, 2007; Fossen et al., 2007). It is distinguished from a typical fracture forming in low-porosity rocks in several ways. Firstly, it does not exhibit a distinct slip surface, and show smaller offsets than what is seen in extensional fractures or slip surfaces. Secondly, deformation bands tend to maintain or even increase cohesion, as well as exhibit a reduction in porosity and permeability while the opposite is typically seen in fractures. (Fossen et al., 2007). The term deformation band was first applied by Aydin (1978) when studying sandstones in the San Rafael Desert, Utah (USA). Examination of larger faults revealed small faults with no slip surfaces that were referred to as deformation bands. These occurred as secondary structures nearby major faults and were believed to play an important role in the generation of faults (Aydin, 1978). Today, deformation bands are of particular interest to petroleum geologists because of their ability to alter fluid flow in reservoirs.

2.2 Classification of deformation bands

Deformation bands are classified based on their kinematics and by their main deformation mechanism. Kinematically, deformation bands can predominantly be classified as shear bands, dilation bands, compaction bands or a hybrid of the three types (Fig. 2.1). Shear bands display no volume change, while dilation bands involve volume increase and compaction bands involve volume decrease (Aydin et al., 2006; Fossen et al., 2007; Fossen et al., 2017). Common hybrids are compactional shear bands, dilational shear bands, shear enhanced dilation bands and shear enhanced compaction bands (Fig. 2.1). Most deformation bands are dominated by shear displacement with or without a component of compaction or dilation (Fossen et al., 2017). A

more common way of classifying deformation bands is under the terms of the dominant deformation mechanism during their formation. External and internal factors such as mineralogy, grain size, shape, sorting, cementation, porosity, and stress state affect the deformation mechanism, and will produce bands with different petrophysical properties. The principal types of deformation bands are: (1) disaggregation band; (2) phyllosilicate band; (3) cataclastic band; (4) solution and cementation band (Fig. 2.2) (Fossen et al., 2007).

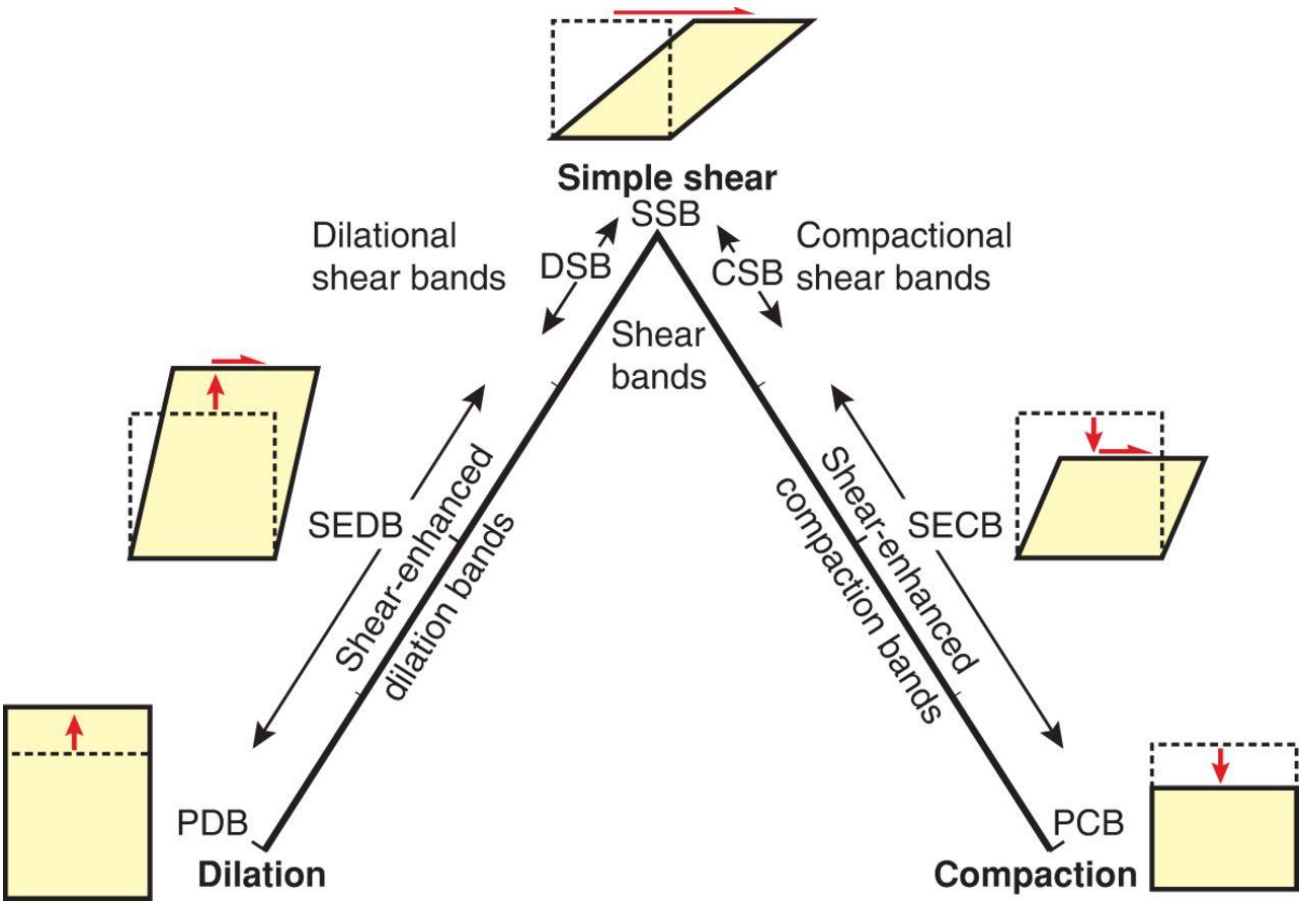

Figure 2.1: Kinematic spectrum of deformation bands between the end members compaction, simple shear, and dilation. Figure from Fossen et al., 2017.

2.2.1 Disaggregation bands

Disaggregation bands are shear-related deformation bands and develop by the means of grain rolling, grain boundary sliding or by breaking of grain bonding cements (Fossen et al., 2007). These processes are referred to as granular flow and there is little to no grain crushing involved

(Twiss and Moores, 1992; Hesthammer and Fossen, 2001). Disaggregation bands are commonly found in sands or poorly consolidated sandstone with low phyllosilicate content and may be only detected when they cross and offset laminae. Their offsets are typically a few centimeters, and thickness varies depending on the grain size of the host rock (Fossen et al., 2007). Zones of disaggregation bands are associated with only very minor decrease in permeability and porosity, depending on whether they are dilational or compactional bands (Hesthammer and Fossen 2001; Fossen et al., 2007).

2.2.2 Phyllosilicate bands

Phyllosilicate bands form in sandstone where the content of clay, mica and other platy minerals exceeds 10-15%. The dominant deformation mechanism is granular flow, which can produce preferential alignments of the grains and clay minerals (Fossen et al., 2007; Maciel et al., 2018). The platy minerals promote frictional grain boundary sliding that counteracts strain hardening from interlocking of grains. That allows for phyllosilicate bands to accumulate greater offsets. Smearing of the platy minerals can give the band a distinctive color which makes them easy to detect (Fossen et al., 2007). Phyllosilicate bands have a high sealing potential and the bands have been found to reduce rock permeability by three orders of magnitude (Hesthammer and Fossen, 2001).

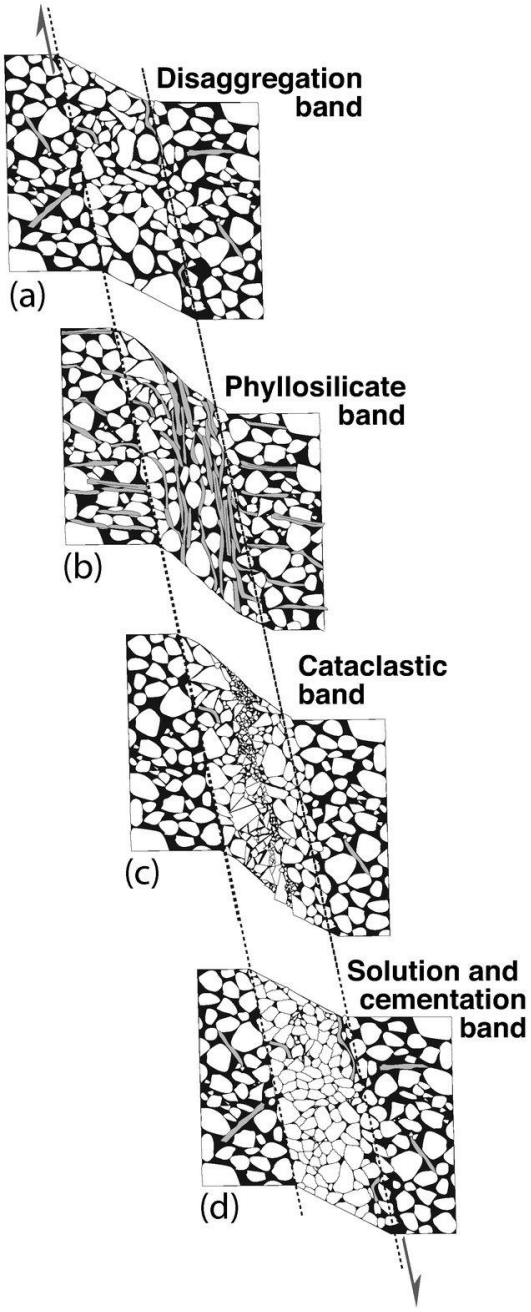

Figure 2.2: Deformation band classification based on the dominant deformation mechanism involved during formation. From Fossen et al., 2007.

2.2.3 Cataclastic bands

Cataclastic bands form by mechanical grain fracturing, and therefore involves a significant amount of grain crushing/fracturing. Cataclastic bands typically consist of a cataclastic core with a volume of compacted rock surrounding it. The core is characterized by a wide grain-size distribution and a distinct reduction of pore space (Aydin, 1978; Fossen et al., 2007). The crushing of grains during cataclasis promotes strain hardening by extensive grain interlocking, and as a result there are smaller displacements observed on cataclastic bands compared to disaggregation and phyllosilicate bands. Cataclastic deformation bands are found throughout the world, but mostly in rocks that have been buried at depths of 1.5-2.5 km (Fossen et al., 2007). The decrease of porosity and permeability in cataclastic bands are controlled by the intensity of cataclasis within the band, and the intensity of cataclasis is again controlled by external factors such as sorting, grain size and grain shape. A well sorted host rock with high porosity and coarse grain size is favorable for higher permeability contrasts (Fossen et al., 2007; Ballas et al., 2015).

2.2.4 Cementation and solution bands

Cementation and solution bands are deformation bands that are formed when there is a significant amount of dissolution and cementation of grain boundaries. Cementation typically occurs during or after deformation at grain-grain contact points. If solution is significant, the term ‘solution band’ is used. Dissolution is a common feature of deformation bands formed at shallower depths, but studies have shown that quartz dissolution and precipitation accelerate after burial and heating to >90 °C (i.e., depths greater than 3 km) (Walderhaug 1996; Fossen et al., 2007)). Cementation is promoted by fresh and highly reactive surfaces formed by cataclastic deformation, particularly in bands where the host sand grains are coated by diagenetic minerals (Hesthammer et al., 2002; Fossen et al., 2007). Cementation and dissolution in deformation bands are reported to result in a significant increase in the reduction of porosity and permeability, but the discontinuous nature of many cements make them a less significant influence on fluid flow (Fisher and Knipe, 2001; Fossen et al., 2007).

2.3 Deformation bands and their significance in fault growth

Deformation bands play an important role in the generation of larger faults in porous sandstones as deformation bands are often the precursors of faults (Aydin, 1978). As mentioned previously, deformation bands can occur as individual deformation bands, zones of deformation bands, or as slip surfaces (Aydin and Johnson, 1983; Fossen et al., 2007). A single deformation band will initially form, but strain hardening will eventually make the band stronger than the host rock. This results in it being easier to form a new band adjacent to the primary band than to keep shearing the primary band (Aydin and Johnson, 1983; Nicols et al., 2013). Over time, a complex zone of multiple, interconnected deformation bands will form (Fossen, 2010). Once the porosity is sufficiently reduced a slip surface can form. Slip surfaces tend to nucleate in small patches and then nucleate and link up to form through-going slip surfaces (Shipton and Cowie, 2001; Fossen et al., 2007) (Fig. 2.3). Once the fault is formed, the already existing zone of deformation bands become the damage zone that surrounds the fault core.

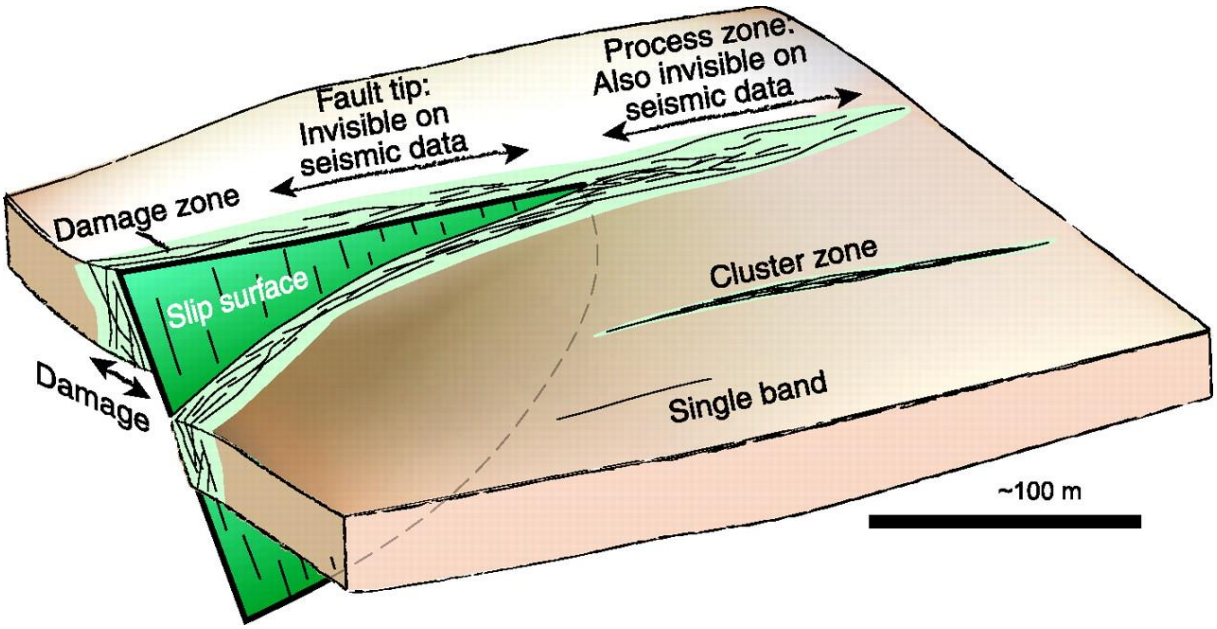

Figure 2.3: Schematic model of fault development in sandstones where deformation bands are considered precursors for faulting. A slip surface is formed in a deformation band cluster, leading to the enclosing volume of deformation beds becoming the damage zone. From Fossen et al., (2007).

2.4 Effect on fluid flow

Several studies have been focusing on the effects of deformation bands in reservoirs, as deformation bands are found in most siliciclastic sandstone reservoir (e.g., Sternlof et al., 2006; Fossen and Bale, 2007; Rotevatn et al., 2013). It is proven that deformation bands can reduce porosity and permeability by several orders and potentially act as barriers of fluid flow, but

their practical effect is not clear (Antonellini and Aydin, 1996; Fossen et al., 2007). Deformation bands can be laterally extensive structures, which in theory should increase their ability to baffle fluid flow. However, studies have shown that there is great lateral variation in porosity and permeability along a single deformation band (e.g., Fossen and Bale, 2007; Torabi and Fossen, 2009). Experiments show that porosity across bands ranged from about 17% in the margin of bands to about 12 % within the central part of the shear zone (Torabi et al., 2007). Permeability measurements can change from zero to two or three orders of magnitude over a short distance within a single band. A single deformation band is therefore regarded as having restricted contribution to the sealing properties of a fault because of its great lateral variation (Torabi and Fossen, 2009). However, thick clusters of cataclastic deformation bands would have the potential to influence the fluid flow at a greater scale (Torabi et al., 2013; Fossen et al., 2017). Conjugate sets of deformation bands may alter the fluid flow path and effectively reduce the general flow rate and the sweep efficiency during injection (Fossen and Bale, 2007; Fossen et al., 2017) Therefore, deformation bands cannot be ignored in a reservoir, and it is important to consider the frequency of deformation bands, the type of band, where they occur relative to faults, their permeability-reducing properties, and their lateral and vertical continuity when considering well productivity (Fossen and Bale, 2007; Fossen et al., 2017).

2. 5 Coal

In order to fully understand the behaviour of the coal in our deformation bands it is necessary to provide some background on coal. Coal is a complex and diverse material, and researchers have argued over how to best classify the different ranks and macerals of coal (Xie, 2015). Coal is divided into two main groups according to the coal-forming plants, humic coals and sapropelic coal. Humic coal is formed by macroscopic plant material, which mainly consists of plant lignin and cellulose. Sapropelic coal is formed by a variety of microscopic plant material, typically algae and plant spores (Thomas, 2012; Xie, 2015). Humic coal is what makes up the largest reserve of coal in the world and is what we typically refer to when we speak of coal (Thomas, 2012; Greb et al., 2017). Therefore, when discussing the formation and classification of coal in the next section it will only include humic coal.

2.5.1 Coal formation

Coal is a sedimentary rock that consist of both organic and inorganic components (McGabe, 1984; Greb et al., 2017). The organic components are mainly derived from plant material that have accumulated in swampy depositional environments and undergone biochemical and geochemical reactions to evolve into peat. Peat deposits are typically coeval with larger sedimentary erosional-depositional systems such as alluvial-delta, barrier-coastal and lake-lagoon environments and are formed in the low-lying, quiet environments of the mentioned systems (Fig. 2.4) (McGabe, 1984; Diessel et al., 2000; Dai et al., 2020). The process of evolution of plants to peat is referred to as the paludification stage and can only take place under certain external conditions (Xie, 2015). A high level of plant accumulation is necessary, as well as an appropriate environment where plant remains can be preserved. Swamps provide such conditions, with poor drainage and high level of plant reproduction (McGabe, 1984; Dai et al., 2020). In the initial stage of paludification the plant material is exposed to air in the shallow parts of the swamp, which leads to oxidative decomposition and hydrolysis reactions. Over the years, the incompletely decomposed plants accumulate in thick layers, and they become progressively isolated from fresh supply of oxygen (McGabe, 1984; Diessel et al., 2000). Products from the decomposition of plants such as hydrogen sulphide and organic acids prevent the activities of aerobic bacteria and fungi. This results in a weak oxidative system or even a reducing environment. If the plant material is buried in an aerobic environment, they will possibly be fully decomposed, which does not lead to peat formation. During the paludification stage, plants can undergo different physical and chemical changes. Water depth and mobility influence the pH and oxidation/reduction potential, which again affect microorganism activity. This gives rise to a large variation of accumulation environment for peat, which results in different compositions, sulphur content, and reduction degree of coal (McGabe, 1984; Xie, 2015).

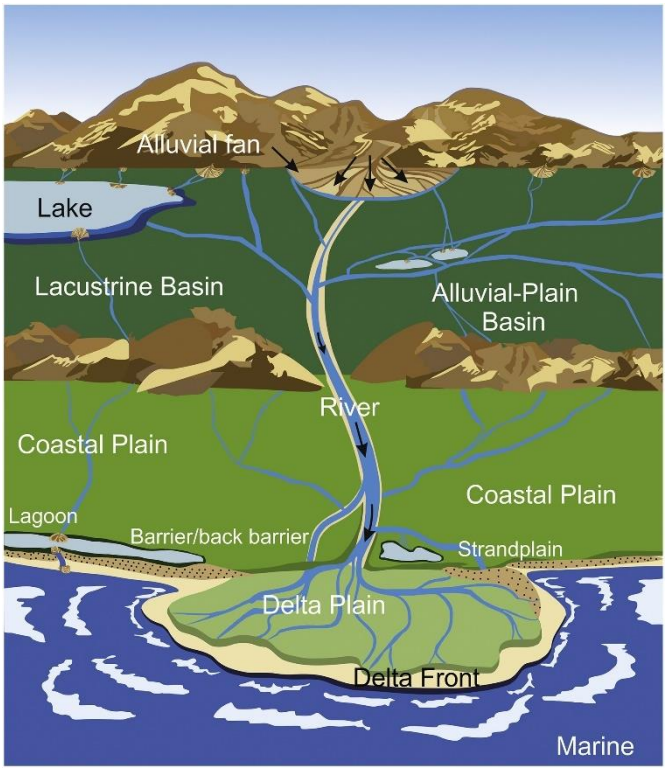

Figure 2.4: A schematic diagram of a generalized depositional system from mountain-front alluvial fans to coastal delta plains. Potential coal forming environments are shown by the light to dark green areas. From Dai et al., 2020.

Eventually, inorganic sediments are deposited on top of the peat, which weakens and gradually stops the biochemical processes that take place during the paludification stage (Xie, 2015). Physical and chemical reactions that transform peat into coal is now driven by changes in temperature and pressure. The transformation is called the coalification stage and can be divided into diagenetic and metamorphic stages (Teichmüller. 1987; Xie, 2015). During the diagenetic stage the peat is subjected to high pressure from overlying sediments, which leads to compaction and dehydration. Remaining plant components from the peat gradually disappear, and the carbon content increases (Teichmüller, 1987; Xie, 2015; Greb et al., 2017). The peat is eventually transformed into lignite. Lignite is the lowest rank of coal and is formed at relatively low temperatures (Sivrikaya, 2014*)*. As the lignite is further buried the temperatures and pressures increases. This is the metamorphic stage, and the lignite is transformed into bituminous coal and anthracite (Xie, 2015). Temperature, pressure, and time are the main factors during the metamorphic stage. Coal has a faster reaction to changes in temperature and pressure than mineral suites in rocks do. Therefore, coal can be used as an indication of low-rank metamorphic degree in sequences where the minerals do not exhibit any changes (Teichmüller, 1987; Thomas, 2012). Increasing temperature is the main factor, which results in the different ranks of coal. The changes in pressure can reduce the porosity and moisture content, make the coal compact, and arrange the coal lithofacies components along a certain direction (Thomas, 2012; Xie, 2015)

2.5.2 Coal classification

Because of the large variations that can be found within coal, a classification system has been necessary for coal petrology. This classification system approaches the coal on both a macro and micro scale. Macroscopic research is based more on the visuals of the coal, such as colour, lustre, fracture, and hardness, as well as vitrinite reflectance and carbon content. This method identifies the different lithotypes of the coal, which is commonly referred to as coal rank (McGabe, 1984).

Rank

Coal rank describes the degree of coalification that the peat has experienced during burial history. It refers to the changes in geochemistry and reflectance that reflect the thermal maturity

of the coal, with higher ranks being more thermally mature. (Ward et al., 2005; Keefe et al., 2013). The three major types that can be distinguished is lignite, bituminous coal, and anthracite. Lignite and subbituminous coal are low rank coal which are commonly referred to as brown coal. Bituminous and anthracite coals are high rank coals which are commonly referred to as black or hard coal (Thomas, 2012). The rank is measured by a progressive increase in carbon content and vitrinite reflectance, as well as a decrease in moisture and volatile functional groups (Ward et al., 2005; Keefe et al., 2013; Xie, 2015). The different characteristics of the ranks are described in table 2.1.

Table 2.1: Characteristics of the different coal ranks. From Xie, 2015.

Characteristic	Peat	Lignite	Bituminous coal	Anthracite
Color	Dark brown	Brown and blackish brown	Black	Grayish black
Luster	No	Mostly no	Certain luster	Metallic luster
Appearance	With dead original plant, earthy	Without dead original plant or obvious stripes	Striped	Without obvious stripes
Color in boiling KOH solution	Brownish red–brownish black	Brown	Colorless	Colorless
Color in dilute HNO_3 solution	Brownish red	Red	Colorless	Colorless
Natural moisture	High	Relatively high	Relatively low	Low
Humic acids	Plenty	Part	No	No
Density (g cm^{-3})	–	1.10–1.40	1.20–1.45	1.35–1.90
Hardness	Extremely low	Low	Relatively high	High
Upon burning	Some smoke	Some smoke	Large amount of smoke	Smokeless

Type

Coal type refers to the depositional origin of the coal, meaning the original peat forming plant debris and plant components (wood, spores, algae etc.) (Ward et al., 2005; Moore and Li., 2006; Keefe et al., 2013). The term maceral is being used to describe coal type and was first introduced by Stopes (1935) as the coal equivalent of minerals in a rock (Scott, 2002). Macerals are microscopic components of coal that represents the altered remains and by-products of the original plant material (McGabe, 1984; Scott, 2002; Greb et al., 2017). They reflect the Eh and pH conditions and the microflora of the peat at the time the organic matter was deposited. Macerals are controlled by the climate and sedimentary input during deposition, meaning that the maceral type is independent of the grade of coal rank and coalification (Keefe et al., 2013).

It simply reflects the relative proportions of the different plant-derived constituents in the coal. Recognition of macerals can help in developing an understanding of the depositional environment (McGabe, 1984). Macerals are classified under three broad groups: liptinites, inertinites and vitrinites. Liptinites are derived from small waxy plant components such as spores, pollens, algaes and leaf cuticles. Inertinites consists mainly of oxidised remains of woody material. Vitrinites are largely derived from well-preserved or gelified wood tissues and structurally resistant plant tissue (McGabe, 1984; Moore and Li, 2006: Dai et al., 2020). For low rank coals, huminite is referred to as the precursor to vitrinite (Greb et al., 2017). The three groups of macerals can be further subdivided into smaller groups based on their original plant components (Table 2.2).

Table 2.2: The different groups and subgroups of macerals and their suspected origins. From Greb et al., 2017.

Low-rank Macerals			Higher-rank Macerals			Origin
Group	Subgroup	Maceral	Group	Subgroup	Maceral	
Huminite	Humotelinite	Texinite →	Vitrinite	Telovitrinite	Telinite	Plant cell walls (with visible structure)
		Ulminite →			Collotelinite	Plant cell walls (gelified, structureless)
	Humotelinite	Attrinite →		Detrovitrinite	Vitrodetrinite	Small particles of attritus (huminitic particles)
		Densinite →			Collodetrinite	Mottled groundmass (originally attritus)
	Humocollinite	Corpohuminite →		Gelovitrinite	Corpogelinite	Primary and secondary cell infillings from humic gels
		Gelinite			Gelinite	Crack infillings of amorphous humic matter
Liptinite		Sporinite			Sporinite	Outer membranes of plant spores and pollen
		Cutinite			Cutinite	Outer coatings (cuticles) of leaves, roots, stems
		Suberinite			Suberinite	Suberinized cell walls of cork in bark and roots
		Resinite			Resinite	Plant resins, balsams, latexes, fats, and waxes
		Alginite			Alginite	Algae (mostly planktonic)
		Bituminite			Bituminite	Amorphous degraded material of algal or bacterial origin
		Exsudatinite*			Exsudatinite	Secondary crack-filling material after oil generation
		Liptodetrinite			Liptodetrinite	Mechanically degraded particles and residues of liptinites
		Chlorophyllinite			X	Chlorophyll-derived material in peat through lignite rank
Inertinite		Fusinite			Fusinite	Fusinization of plant cell walls (fires, decarboxylation, etc.)
		Semifusinite			Semifusinite	Weakly humified and dehydrated plant tissues
		Funginite			Funginite	Fungal spores, sclerotia, and other fungal tissues
		Secretinite			Secretinite	Oxidation of resin and possibly humic gels
		Macrinite			Macrinite	Dehydrated flocculated humic matrix substances
		Inertodetrinite			Inertodetrinite	Fusinization of tiny varied inertinite precursors
		X			Micrinite	Secondary coalification residues of liptinitic substances

3 Geological background

The purpose if this chapter is to introduce and provide an overview of the geological evolution of New Zealand from pre-Cretaceous to present. It will also outline the regional geology and stratigraphy of the study area in SE Otago.

3.1 Tectonic evolution of New Zealand

3.1.1 Part of Gondwana (Pre-Cretaceous)

New Zealand was in pre-Cretaceous times part of the supercontinent Gondwana. Gondwana formed during late Neoproterozoic and included most of South America, Africa, India, Arabia, Madagascar, East Antarctica, and Western Australia (Svensen et al., 2017). Gondwana remained amalgamated until the Mesozoic, when it progressively started to break up into smaller crustal fragments. During this period New Zealand was located on the eastern edge of Gondwana, where it formed part of a typical convergent margin that was characterised by subduction zones and arc magmatism (Fig. 3.1) (Laird and Bradshaw, 2003; Mortimer et al., 2019; Robertson et al., 2019). Rocks formed on the eastern margin, from Permian to Early Cretaceous, comprise incomplete remnants of magmatic arcs, forearc basins and accretionary complexes. Modern geological interpretation recognizes these older rocks as tectonostratigraphic units and refers to them as terranes (Bradshaw, 1989; Cambell and Landis,

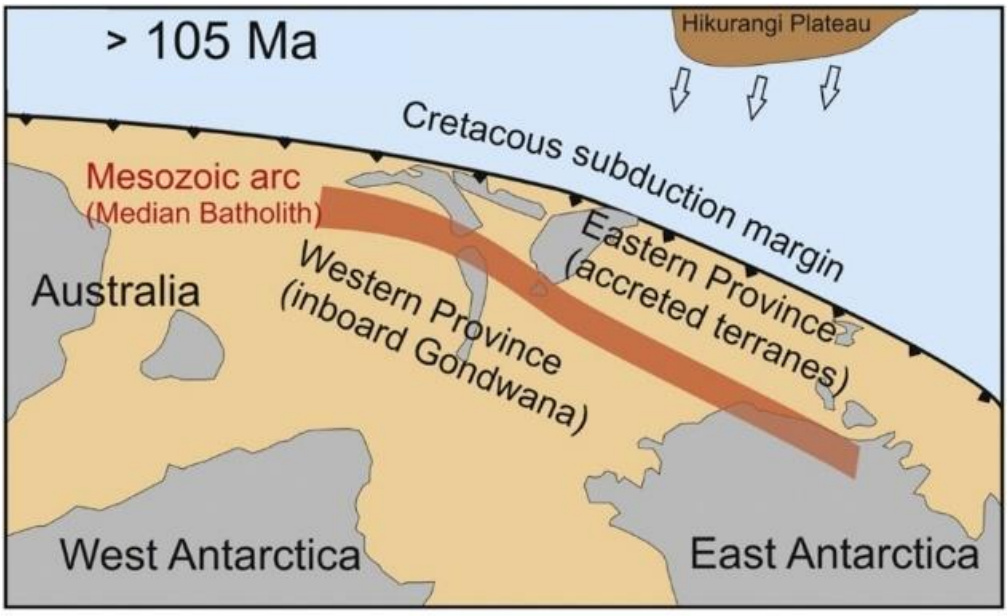

Figure 3.1: Paleogeographic reconstruction of the Eastern Gondwana subduction zone. The location of the Eastern Province and Western Province that form the basement rock of New Zealand is shown, with the Median Batholith separating them. Modified after Van der Meer et al., (2016).

2009; Robertson et al., 2019). A terrane is by definition a fault-bounded slice with its own distinctive geological history (R. A. Cooper, 1989). The terranes formed on the eastern margin of Gondwana make up the present basement rocks of New Zealand and are divided into two contrasting geological provinces: The Early Palaeozoic Western Province and the Late Palaeozoic-Mesozoic Eastern Province (Fig. 3.1 and 3.2b) (Mortimer, 2004; Wandres and Bradshaw, 2005; Robertson et al., 2019).

The Western Province

The Western province comprises the Buller and Takaka Terrane and the Tuhua Intrusives. It is confined to the western part of the South Island, mainly in West Nelson, Westland and Fiordland (Fig. 3.2b) (Mortimer et al., 2004; Robertson et al., 2019). The Western Province consists mostly of metasedimentary and metavolcanic rocks and its extent is much greater offshore and have been found in the Campbell Plateau and Lord Howe Rise (Fig. 3.2a) (Cooper and Tulloch, 1992; Robertson et al., 2019). The Buller Terrane is recognized to be the terrane originating closest to the interior of Gondwana. It consists of metamorphosed siliciclastic sandstones and mudstones, which is inferred to have been deposited on a passive continental margin (Cooper, 1989; Mortimer, 2004). The Takaka Terrane consist of a diverse range of rock types, mainly siliciclastic, carbonates and volcanic rocks. The tectonic setting of deposition of the oldest sediments is believed to be an intra-oceanic island arc from Middle and Late Cambrian. This was succeeded by continental passive margin sedimentation during the Ordovician to Devonian (Cooper and Tulloch, 1992; Mortimer, 2004). The Tuhua Intrusives is a term used for all plutonic rocks in the Western Province (Mortimer et al., 2014). The largest and most voluminous of the Tuhua Intrusives is a Cambrian-Early Cretaceous Cordilleran batholith, the Median Batholith. The Median Batholith forms the boundary between the Western and Eastern Province and has been displaced by the Alpine Fault (Fig. 3.2b) (Wandres and Bradshaw, 2005; Mortimer et al., 2014; Robertson et al., 2019)

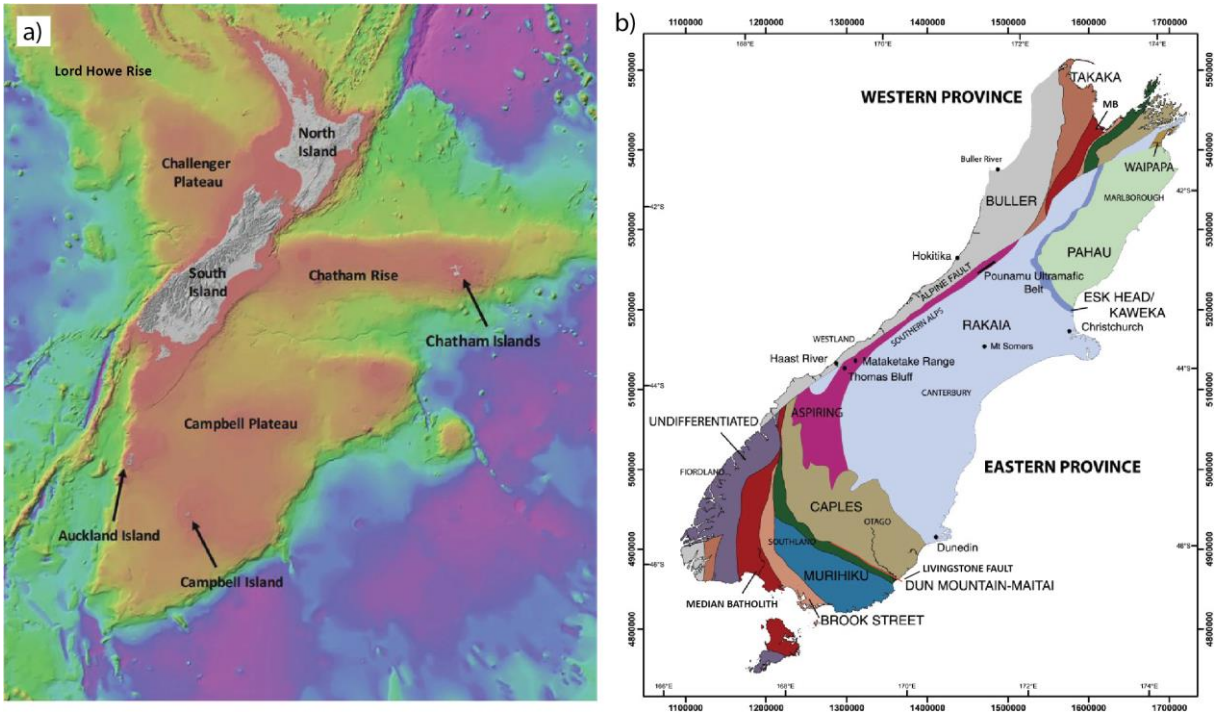

Figure 3.2: a) Bathymetric map of Zealandia. From NIWA (www.niwa.co.nz). b) map of South Island, New Zealand, showing the Western and Eastern Province and their terranes. Modified after Cooper and Ireland, 2003.

Eastern Province

The Eastern Provence is an assemblage of allochthonous terranes that make up most of the North Island and the eastern part of the South Island. The terranes are commonly subdivided into two groups that are separated by the Livingstone Fault (Fig. 3.2b) (Kimbrough et al., 1992; Wandres and Bradshaw, 2005; Cambell et al., 2020). The Brook Street Terrane, Murihiku Terrane, and Dun Mountain (Maitai) Terrane are located southwest of the Livingstone Fault and are structurally simple, with no development of schistosity. The north-eastern terranes are the Caples Terrane, Torlesse Terrane, and Waipapa Terrane. These have undergone multiple phases of deformation, with well-developed schistosity (Wandres and Bradshaw, 2005). The Brook Street Terrane is thought to represent a primitive intraoceanic island arc assemblage in early Permian and consist of moderately metamorphosed submarine volcanics and volcanoclastics of basaltic-andesitic composition (Kimbrough et al., 1992; Mortimer, 2004; Wandres and Bradshaw, 2005; Robertson et al., 2019). The Letham Ridge Thrust separates the Brook Street Terrane from the Murihiku Terrane. The Murihiku Terrane is the least structurally deformed of the basement terranes (Robertson et al., 2019). It comprises the Murihiku supergroup, a volcanoclastic marine sandstone dominated succession from Late Permian to Late Jurassic. Its petrographic and geochemical data imply derivation from a nearby oceanic

arc and is considered to have formed parallel to the Gondwana margin in a forearc setting (Cambell et al., 2003; Mortimer, 2004; Wandres and Bradshaw, 2005). The Dun Mountain-Maitai Terrane consists of the Early Permian Dun Mountain Ophiolite Belt (DMOB) and the Maitai Group. The DMOB comprises mafic and ultramafic rocks from an inferred forearc setting. Overlying the DMOB is a well stratified Late Permian to Middle Triassic volcanoclastic sedimentary succession forming the Maitai Group (Kimbrough et al., 1992; Mortimer, 2004; Cambell et al., 2020). The Dun Mountain-Maitai Terrane marks the border between the structurally simple arc terranes and the highly deformed terranes to the northeast of the Livingstone Fault (Mortimer, 2004; Wandres and Bradshaw, 2005). The Caples terrane stretches from the eastern Otago coast to the Alpine Fault, as well as in the Nelson area where it has been offset by the Alpine fault. It comprises marine volcanoclastic greywacke and argillite from Permian to Triassic that has been weakly metamorphosed from prehnite-pumpellyite facies to lower greenschist facies (Mortimer, 2004; Adams et al., 2009; Robertson et al., 2019). Sedimentation is inferred to have been from submarine fans in lower trench slope basins adjacent to an active arc. The Torlesse terranes constitute the Rakaia Terrane (Older Torlesse Terrane) and Pahau Terrane (Younger Torlesse Terrane) (Mortimer, 2004; Wandres et al., 2004; Mortimer et al., 2014). The Rakaia Terrane is dominated by Permian to Late Triassic turbiditic submarine quartzofeldspathic sandstone-mudstones. Sedimentation is believed to derive from an active continental volcanopluton arc (MacKinnon, 1983; Mortimer 2004). The Pahau Terrane forms the younger part of the Torlesse Terrane. It is very similar to the Rakaia Terrane in terms of its lithologic content and structure, but less metamorphosed. The deposits are of Late-Jurassic-Early Cretaceous and have accumulated on a continent-derived accretionary wedge (Mortimer, 2004; Ballance, 2009)**.** The Waipapa Terrane is mainly found on the North Island, with only a small sliver located in the Marlborough region of the South Island. It consists of a diverse assemblage of mainly terrigenous turbidites (Wandres and Bradshaw, 2005). Figure 3.3 shows a crustal cross-section across New Zealand where the spatial relationship of the terranes is illustrated.

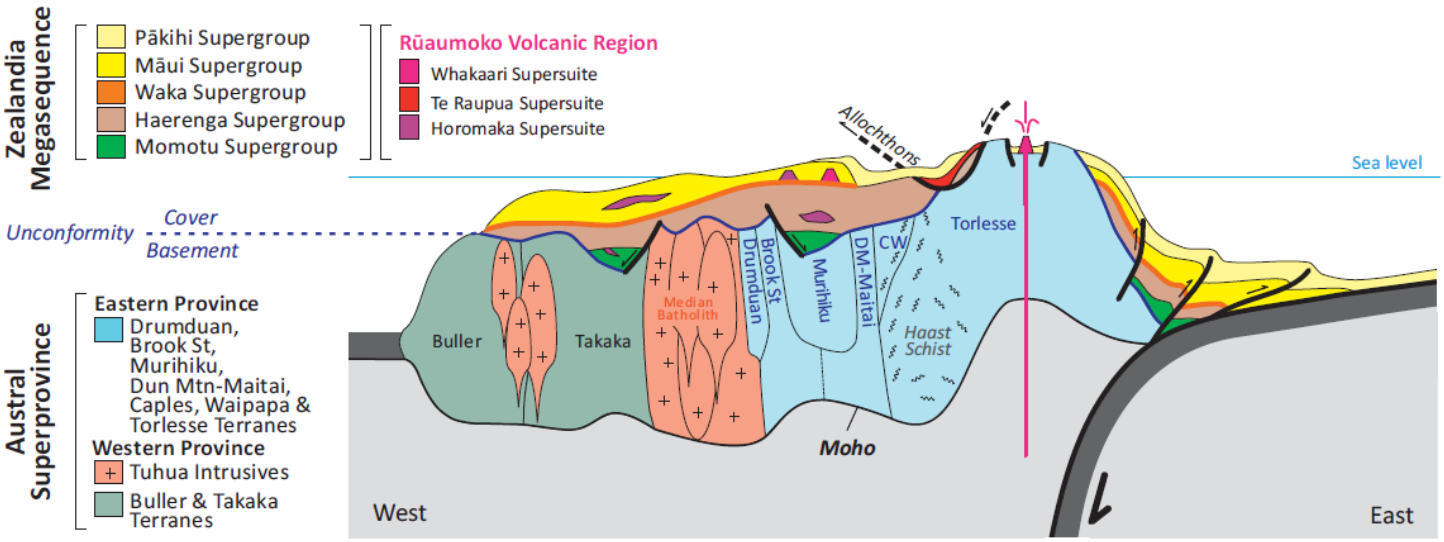

Figure 3.3: Cross section of Zealandia focusing on the spatial relationship of the terranes and its depositional settings relative to the subduction zone. The figure shows a strong vertical exaggeration. From Mortimer et al., 2014.

3.1.2 Zealandia Rift Phase

By mid-Cretaceous time, the subduction at the Gondwana margin ceased and was replaced by an extensional regime that eventually led to the breakup of Gondwana (Bradshaw, 1989**;** Luyendyk, 1995; Ballance, 2009; Robertson et al., 2019). The end of subduction has been linked to the collision of the anomalously thick and hot Hikurangi Plateau into the New Zealand sector of the Gondwana margin, consequently jamming the subduction zone (Bradshaw, 1989; Crampton et al., 2019; Mortimer et al., 2019). A period of extension followed the cessation of the subduction zone, resulting in the breakaway of New Zealand from Australia and Antarctica (Kula et al., 2009; Strogen et al., 2017; Tulloch et al., 2019). This time period is referred to as the Zealandia rift phase, and resulted in regional extension, crustal thinning, and subsidence which subsequently resulted in the formation of sedimentary basins (Strogen et al., 2017; Sahoo et al., 2020). Two sets of gravity lineation that strike in different directions are recognized in Zealandia (Fig. 3.4) (Tulloch et al., 2019). It has been suggested that these gravity lineations are associated with separate rift trends that support a two-stage rifting model Zealandia (Kula et al., 2007; Sahoo et al. 2014; Tulloch et al., 2019). The Campbell Plateau is dominated by gravity lineations that trend at 130° which is associated with the first stage of rifting between Zealandia-West Antarctica and Australia-East Antarctica (Fig. 3.4) (Tulloch et al., 2019). This rifting led to the formation of the Tasman Sea Floor slightly before 83 Ma (Gaina et al., 1998). The age of the first stage of rifting has been widely debated, but the eruptive ages of alkaline

magmas associated with the gravity lineation trend suggest rifting from c. 101-89 Ma (Kula et al., 2009; Strogen et al., 2017; Meer et al., 2017; Tulloch et al., 2019; Sahoo et al., 2020). The first stage of rifting resulted in a succession of sedimentary basins that developed with primary stretching along a NW-SE direction, parallel to the newly formed Tasman spreading ridge (Barrier, 2019; Tulloch et al., 2019; Higgs et al., 2019; Sahoo et al., 2020). The second rift stage is associated with gravity lineations that trend at 70° and represents the extension between Zealandia and West Antarctica, which produced the Pacific-Antarctic Ridge in the Southern Ocean (Fig. 3.4) (Kula et al., 2009; Tulloch et al., 2019). Alkaline magmatism and continental deformation associated with this gravity lineations trend is c. 89-90 Ma (Tulloch et al., 2019).

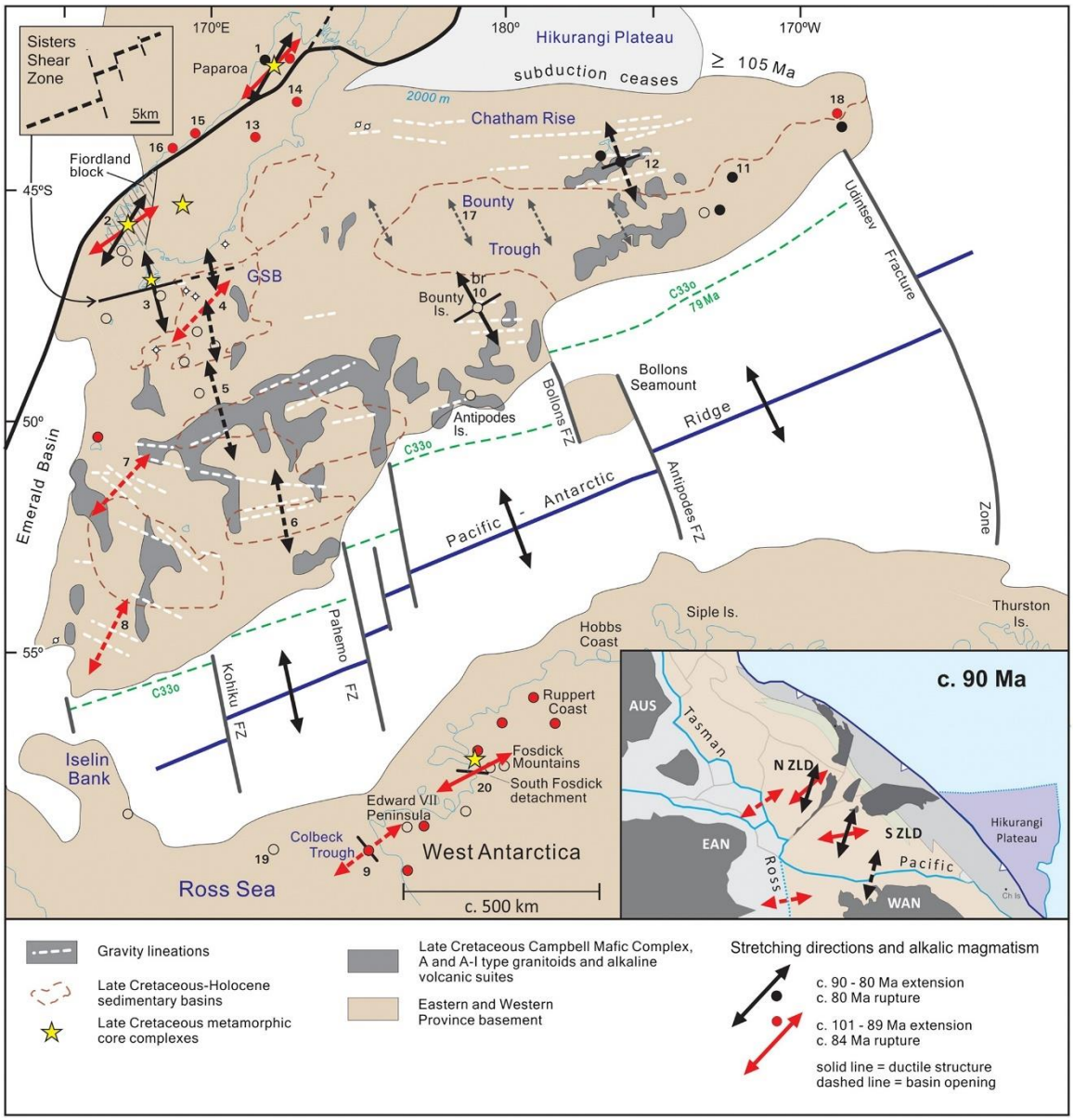

Figure 3.4: Kinematic map of South Zealandia showing extension directions and gravity lineations for c. 101-90 Ma and 90-80 Ma. The extension resulted in the opening of the Tasman Sea (red) and the Pacific Sea (black) respectively (see Figure inset). Numbered locations are references to kinematics/igneous character/age and legend can be found in Tulloch et al (2019). From Tulloch et al., 2019.

3.1.3 Zealandia Megasequence

As Zealandia drifted away during the rifting stage, the continental crust was stretched, thinned, and cooled. The loss of buoyancy resulted in a slow and steady submergence of the continent over a period of 60 Ma until about 23 Ma (Ballance, 2009; Mortimer et al., 2014; Cambell and Landis, 2014). Sedimentary deposits accumulated in basins such as the Great South Basin and the Canterbury Basin that were formed during the rifting events. The sediments deposited during this time form the cover rocks of New Zealand today and are grouped within the Zealandia Megasequence. The Zealandia Megasequence comprises five supergroups and records a 100 Ma long transgressive-regressive stratigraphic cycle (Fig. 3.5) (Mortimer et al., 2014). Momotu Supergroup comprises the sedimentary rocks that rest unconformably on top of the basement rocks. It represents deposits from the initial phase of rifting in eastern Gondwana during the 105-85 Ma intracontinental rifting phase, with non-marine strata being deposited in grabens and half grabens (Fig. 3.3) (Mortimer et al., 2014; Adams et al., 2016; Strogen et al., 2017). By 85 Ma, Zealandia had broken away from Gondwana, accompanied by the opening of the Tasman Sea (Bradshaw, 1989; Gaina et al., 1998). Haerenga Supergroup records the overall marine transgression as a result of deepening of the basins from the Late Cretaceous to the Late Eocene (Mortimer et al., 2014; Adams et al., 2017). The Waka Supergroup was formed during the maximum marine inundation of Zealandia during the Oliogcene. Its constituents are typically carbonates, greensands, calcareous mudstones, and some calcareous sandstones (Mortimer et al., 2014). By 40 Ma, extension in Zealandia was well established, with a series of sub-basins being formed. Anticlockwise rotation of the Pacific plate with respect to a fixed Australian plate developed a convergent plate boundary and the sediment response is seen in all of New Zealand's basins (King, 2000; Mortimer et al., 2014). A new convergent plate boundary resulted in uplift and a regression which is documented by the Maui Supergroup. The inception of convergent plate boundary resulted in an increased input of detrital clastic sediments that were eroded from the rising mountain ranges; hence the Maui Supergroup contains predominantly clastic-dominated sediments (Mortimer et al., 2014). The Pakahi Supergroup represents an acceleration of regional regression during Pliocene to Holocene. It is characterised by fluvio-glacial outwash plains and prograding continental shelf (Mortimer et al., 2014).

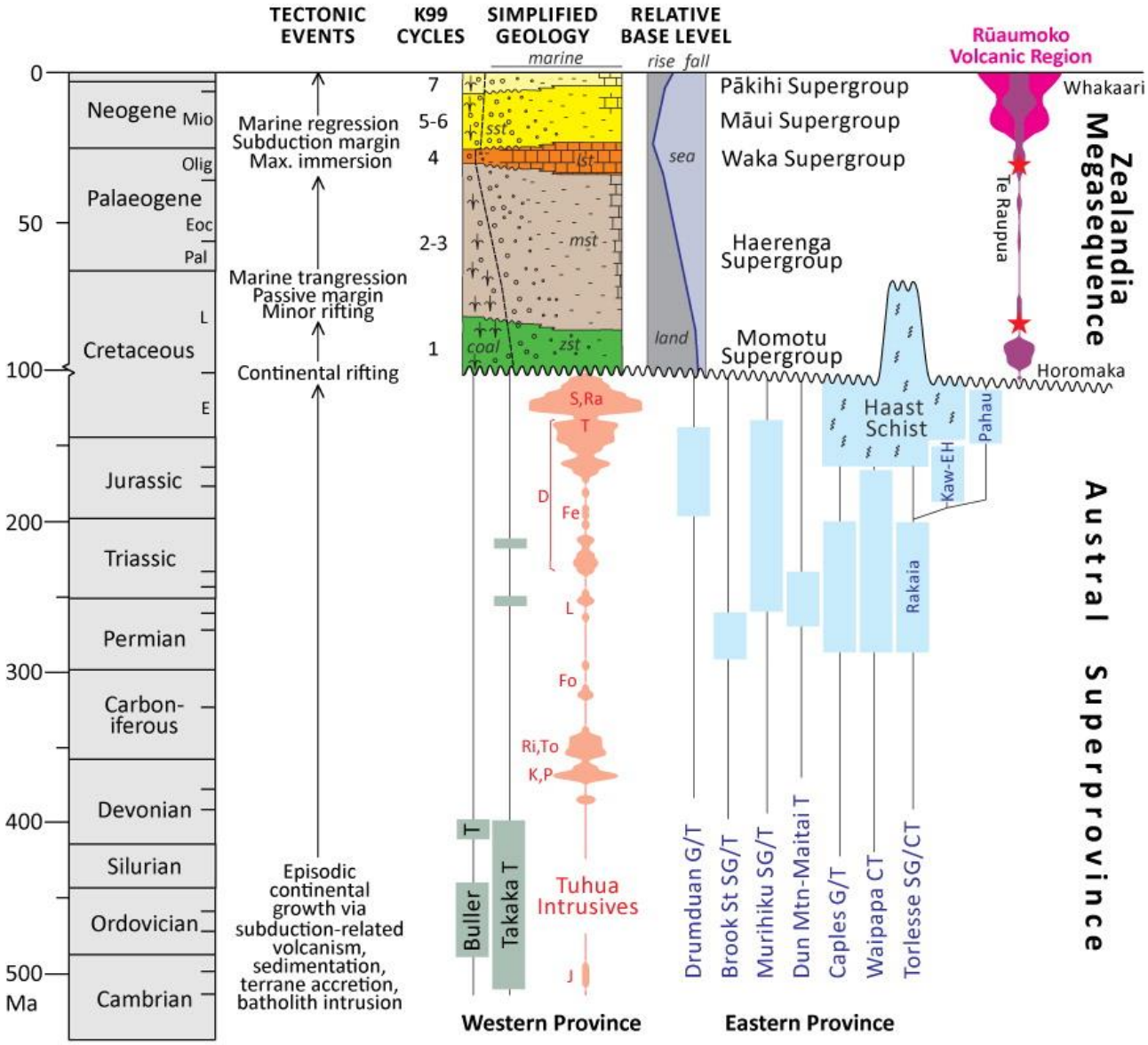

Figure 3.5: General age ranges of the high-level stratigraphic units of New Zealand. The Zealandia Megasequence lies unconformably on top of the old basement terranes of the Western and Eastern Province. The major tectonic events are shown. Figure after Mortimer et al., 2014.

3.1.4. Modern plate boundary and Alpine Fault

By 20 Ma the entire proto-New Zealand region is inferred to have been under compression as the Pacific and Australian plate collided (Sutherland, 1995; King, 2000). This resulted in reactivation of former extensional faults as reverse or thrust faults. Transform fault systems in southern New Zealand began to coalesce into a transfer zone, forming the proto-Alpine Fault (King, 2000). Continuous southward migration of the Euler pole of rotation of the Pacific Plate resulted in the Pacific plate having a general westward motion relative to the Australian plate and by 14 Ma the plate boundary was almost pure-strike slip, with a minor component of extension (Sutherland, 1995; King, 2000; Ballance, 2009). The Alpine Fault accommodated the dextral transform motion between the two plates. The Hikurangi subduction zone was established in the north and thrusting and subduction in the Puysegur Trench was established in the south (Ballance, 2009; Campbell and Landis, 2014). At 6-2 Ma, rotation of the Pacific Plate pole resulted in the motion of the Pacific plate becoming progressively more westward than south-westward, while the Australian plate moved northwards (King 2000; Ballance, 2009; Campbell and Landis, 2014). This resulted in accelerated convergence along the Alpine fault, and uplift of the Southern Alps. Today the pole of the Pacific plate is rotating anticlockwise at a rate of 1° /myr, while the motion of the Australian plate is moving north at around 4 cm/yr (Fig. 3.6a) (Norris and Cooper, 1995; Sutherland, 1995; Ballance, 2009). Oceanic crust of the Pacific plate is subducting beneath the Australian plate north of New Zealand in the Kermadec Trench and Hikurangi Trough (King, 2000; Ballance, 2009). This results in the subduction-related volcanism forming the Taupo volcanic zone on the North Island. As the plate boundary enters continental crust at Cook Strait the movement changes from oblique subduction to dominantly strike slip (Campbell and Landis, 2014). The Wairau Fault in the Marlborough Fault System forms the northernmost sector of the Alpine Fault, where the movement of the Pacific Plate is exactly parallel to the

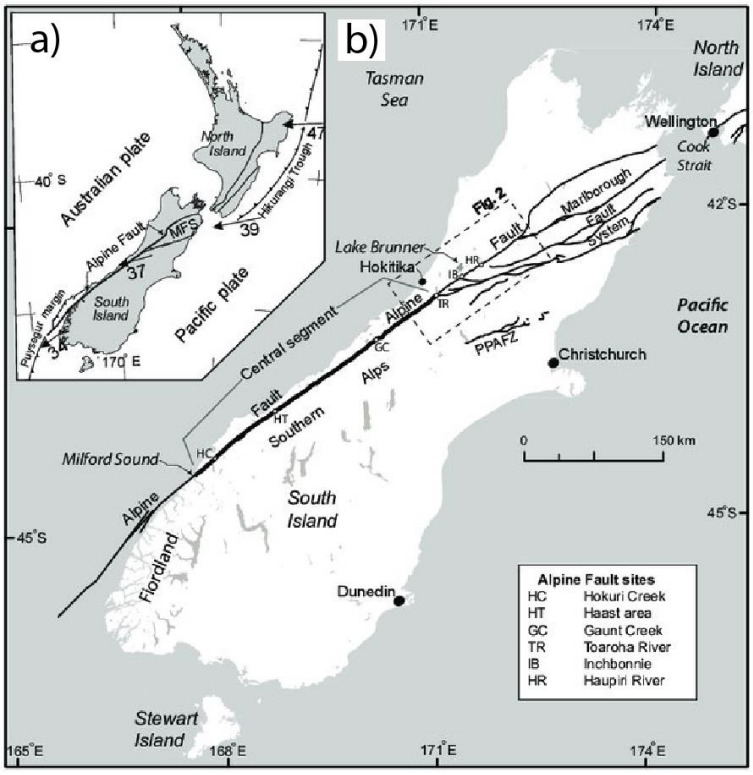

Figure 3.6: a) Map of the modern plate boundary of New Zealand and its motion vectors. b) Map of the Alpine Fault and Marlborough Fault System on the South Island, New Zealand. Legend shows paleo seismic sites of the Alpine Fault. Figure modified after Langridge et al., 2012

fault (Fig. 3.6b). As a result of this there is no compression in the northernmost part of the South Island, and the Southern Alps does not extend this far north (Ballance, 2009). A bend in the Alpine fault further south results in 11° of convergence across the fault, giving rise to the Southern Alps. The Alpine Fault can be traced all the way to Milford Sound where it goes offshore, and the plate boundary re-enters oceanic crust (Norris and Cooper, 1995; Ballance, 2009). In contrary to the north of New Zealand, the Australian plate is now subducting underneath the Pacific plate at a strongly oblique motion that forms the complex Puysegur trench/ridge system south of New Zealand (Ballance, 2009; Campbell and Landis, 2014).

3.2 Regional geology and stratigraphy

The geology of SE Otago, which is the region of interest for this thesis, consists of Cretaceous to Cenozoic marine and non-marine sedimentary successions from the Zealandia Megasequence that unconformably overlies the Caples Terrane (Mortimer et al., 2014). Jurassic metamorphism resulted in strong foliation and schistosity of the basement terranes; hence the basement rock of Otago is referred to as the Otago Schist (Bishop and Turnbull, 1996; Forsyth, 2001; Mortimer 2003). The Otago Schist forms a 150-kilometre-wide structural arch ranging from prehnite-pumpellyite facies on the flanks to greenschist facies in the centre (Fig. 3.7) (Bishop, 1972; Mortimer, 2003). Rifting in mid-Cretaceous formed a series of extensional fault-bounded basins, including the Great South Basin, which were rapidly infilled by coarse alluvial deposits that forms the Matakea Group which is part of the Momotu Supergroup (Mortimer et al., 2014). Extensional tectonics dominated throughout Cretaceous, activating the Titri fault zone, Tuapeka fault zone and Waipounamu Fault System (Fig. 3.8) (Bishop and Turnbull, 1996). The activation of major fault zones resulted in regional subsidence in latest

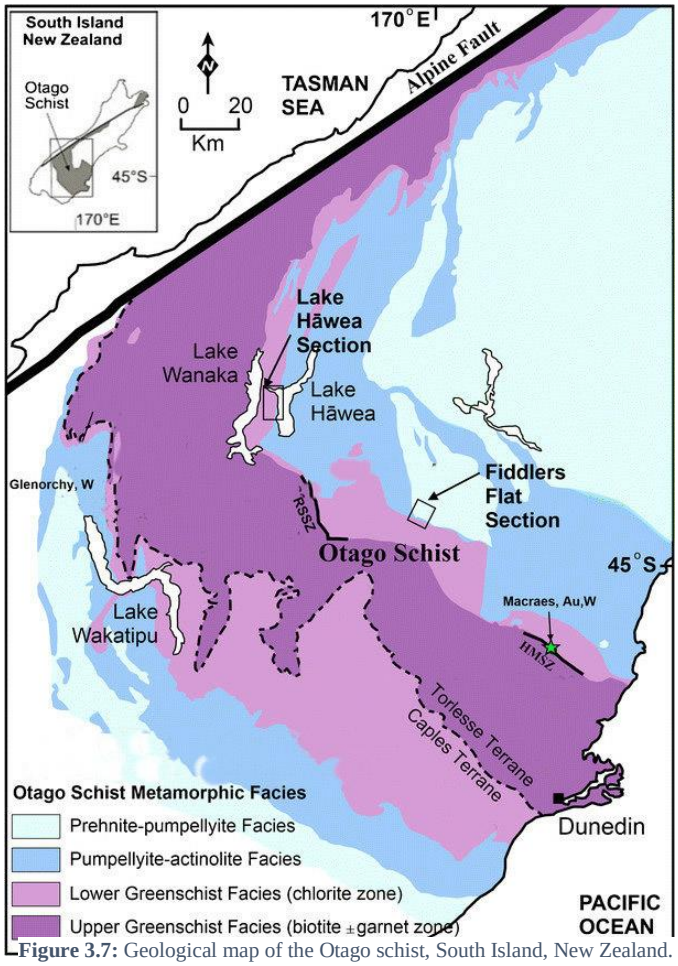

Figure 3.7: Geological map of the Otago schist, South Island, New Zealand. The figure shows the Caples and Torlesse Terrane, as well as the metamorphic facies of the Otago Schist. Modified after Cave et al., 2017.

Cretaceous time and the transgressive sediments of the Onekakara Group were deposited unconformably on basement rocks or the Matakea Group in the Otago region (Fig. 3.9) (Bishop and Turnbull, 1996; Forsyth, 2001). It is sediments from the Onekakara Group that are studied for this thesis. Subsidence continued into late Oligocene time where rotation of the plate boundary resulted in the initiation of convergent tectonics (Sutherland, 1995; King, 2000; Ballance, 2009). The maximum flooding of Zealandia is represented by an extensive marine erosional surface, called the Marshall unconformity, which caps the Onekakara Group (Carter, 1985; Mortimer et al., 2014). Following the Marshall unconformity is a thin package of the Kekenodon Group (Fig. 3.9) (Carter, 1985; Forsyth, 2001). During late Oligocene, inception of the Alpine Fault and regional uplift resulted in a period of regression, with the deposition of the Otakou Group (Bishop and Turnbull 1996; King, 2000). The renewed tectonic activity in late Miocene resulted in the reactivation of the Titri and Tuapeka fault zone, but with a reversed sense of motion (Bishop and Turnbull, 1996; Litchfield, 2001). The Dunedin Volcano Group formed under the influence of local extensional elements, and smaller igneous bodies were intruded adjacent to the faults. The compression across the South Island continues today, with continuing uplift and deformation being associated with the faults and folds that were reactivated during Miocene (Bishop and Turnbull 1996, Forsyth, 2001).

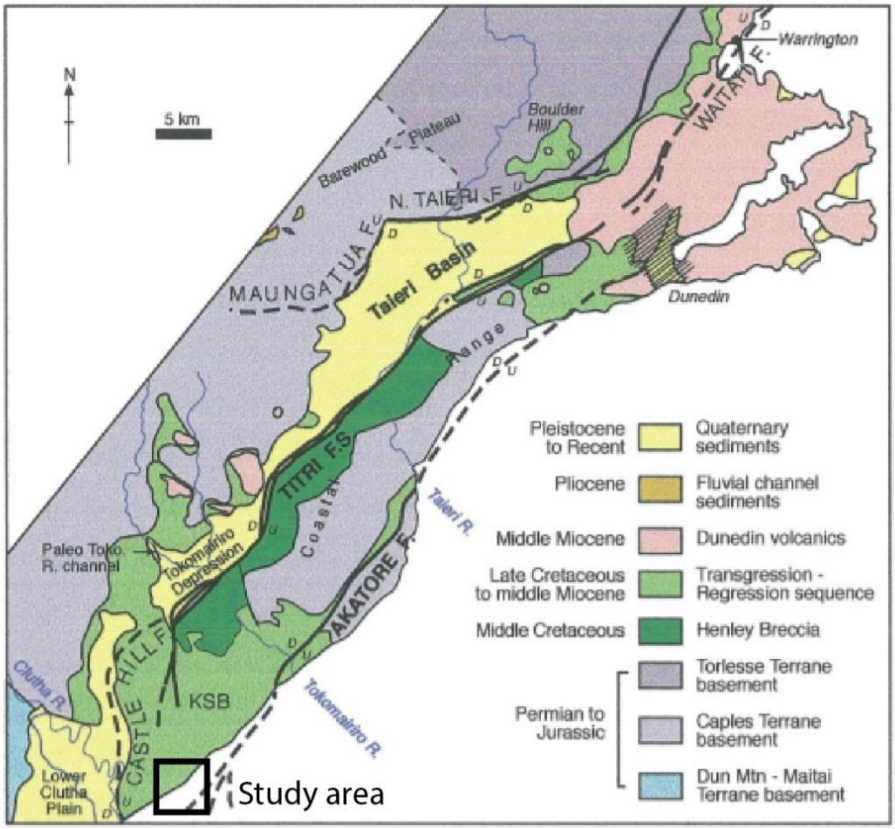

Figure 3.8: Geology of the southeast Otago area and study area including the basement terranes and location of cover sediments. KSB = Kaitangata Sub Basin. From Litchfield, 2000.

Onekakara Group

The Onekakara Group is a transgressive group that is part of the Haerenga supergroup and represents the transition from non-marine to shallow marine. The studied area for this thesis consists solely of the Taratu Formation which is part of the Onekakara Group. The Taratu Formation forms the base of the Onekakara Group and reaches a maximum preserved thickness of about 600 m in the Kaitangata coalfield (Bishop and Turnbull 1996). The age of the Taratu Formation ranges from Late Cretaceous to Eocene in age (Pole, 1994; Forsyth, 2001). The lower part of the formation consists of quartzose conglomerate interbedded with sandstone, mudstone and thick coal seams. Cross bedding is typical in lower Taratu Formation, indicating stream systems (Bishop and Turnbull, 1996; Lomas, 2003). The upper Taratu Formation show better sorting, hummocky cross stratification, increased bioturbation, and presence of marine dinoflagellates, which indicate marine influence (Kamp et al., 2015). The Taratu Formation is interpreted as a non-marine formation, but with increased marine influence towards the top of the formation. The depositional environment of the lower Taratu Formation is inferred to be in valleys and fluvial plains. Alluvial fans were depositing the coarse conglomerates, with coal forming in the quiet swamp areas in the periphery of a braided river system (Aitchison et al., 1993; Lomas 2003). Gradual marine transgression resulted in the braided river deposits being succeeded by shoreface deposition. The marine part of the Onekakara group includes the Wangaloa, Abbotsford, Green Island and Burnside Formations. They record the transition from the shoreface fossiliferous sandstone of the Wangaloa Formation to the offshore deposited mudstone of the Burnside Formation. The deposits of the Onekakara Group can be traced to a great extent offshore and are found at a few locations along the coast of Otago. The age of the marine sequence of Onekakara Group ranges from Palaeocene to Eocene age (Bishop and Turnbull, 1996). Only the upper part of the Taratu Formation where it grades into the Wangaloa Formation was studied for this thesis.

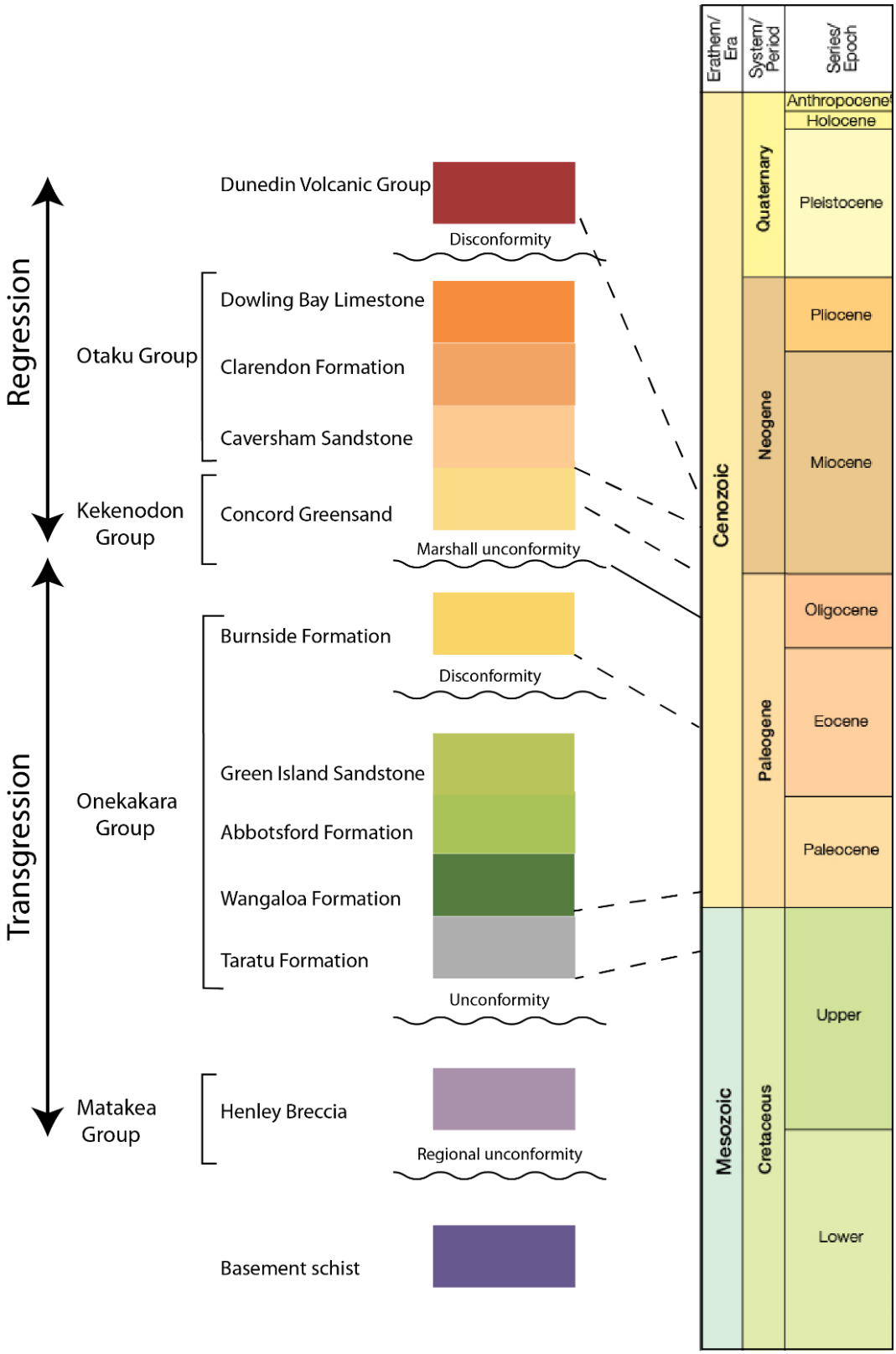

Figure 3.9: Generalized stratigraphic column of the Kaitangata/Wangaloa area. The lithology is based off Bishop and Turnbull (1996) and figure modified after Matthews (2003).

4 Methods

This following chapter will present the methods used during field work and data analysis for this thesis. The first part includes a description of the field methods applied. The second part will focus on the subsequent preparation of the samples collected in order to make thin sections for microscopic analysis as well as a description of the instruments used. The third part will include a description of the workflow used for digital image analysis (DIA) in order to evaluate the porosity and grain size distribution in the samples.

4.1 Field work

A total of two days were spent out in field at Wangaloa beach in January 2020. There were three deformation bands of particular interest at this outcrop. Nine samples were collected along a deformation band cluster (sample set 1) and nine samples were collected along two single deformation bands (sample set 2) (Fig. 4.1). Images were taken of both deformation bands with a digital camera before any sampling was done. Structural data was collected using an app called GeoID on an iPad. This included the orientation of bedding, faults, and deformation bands. No mapping of the local geology was done, as it was not crucial for this study. Instead, a lithological description of the Taratu Formation was noted. Samples were then carefully collected using a hammer and a chisel. Samples from sample set 1 were collected at different increments of thickness of the deformation band cluster and samples from sample set 2 were collected at different increments of displacement moving along dip of the two deformation bands. All the samples were then numbered from W1-W18 and carefully wrapped for transportation back to the lab. Sample W9 and W8 were not used for any work in this thesis.

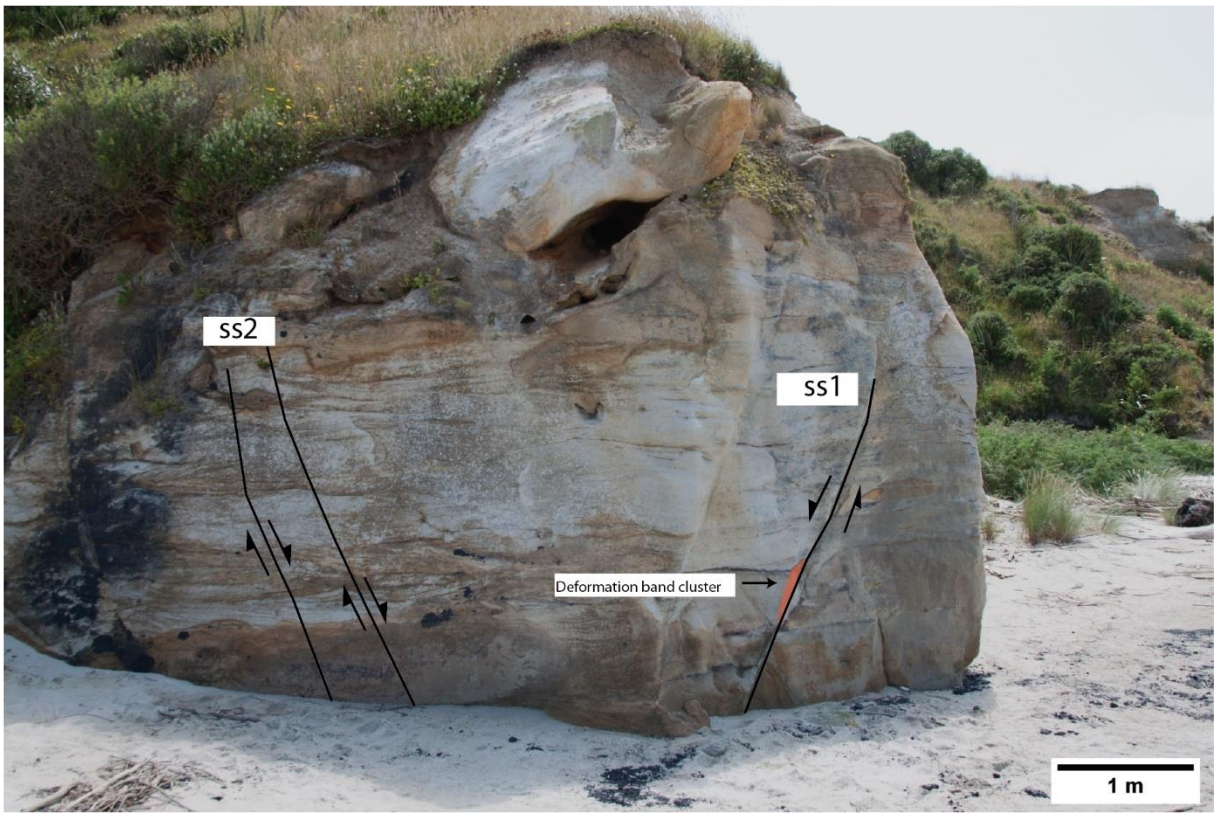

Figure 4.1: Image of the outcrop of interest and the location of the deformation bands used for sampling. Ss1 = sample set 1, ss2 = sample set 2.

4.2 Microscopical analysis

Back in the lab at the University of Otago, the samples were cut and polished in order to make thin sections. The samples were extremely fragile, and it was necessary to completely cover them in resin to harden them before starting the polishing process. 16 samples were first polished using a 200 µm grit, then a 400 µm, before finishing with a 600 µm grit. As the samples were polished, the resin would be grinded away, making the sample crumble again. Because of this, the resin needed to be reapplied several times for the samples to stay intact. Once the polishing was finished, the samples were handed over to a lab technician who prepared the 30 µm thick thin sections. The finished thin sections were analysed by the use of an optical light microscope and a scanning electron microscope (SEM) at the University in Bergen. This allowed for detailed microstructural analysis of the deformation bands and host rock

4.2.1 Optical light microscope

A standard *Nikon Eclipse LV100 POL* polarizing microscope was used to inspect the deformation bands. A *Nikon digital sight DS-Fil* camera was mounted on top of the microscope and *NIS Elements* F image software was used to capture photomicrographs of the thin sections.

Mosaics were created of all the samples by taking several images at 4x magnification and merging them together using Adobe Photoshop. The optical microscope was mainly used for a good overview of each sample, which made it easier to prepare for what to look for under the SEM.

4.2.2 Scanning electron microscope

The scanning electron microscope (SEM) was used to get higher resolution and magnification images of the thin sections. A ZEISS Supra 55VP Field Emission Scanning Microscope was used at the University of Bergen. The SEM is a valuable instrument that can be used for the examination and analysis of microstructures and chemical composition characterization at a resolution down to nanometre scale. Figure 4.2 is a schematic figure of the common setup of a SEM. The basic principle of a SEM is that an electron gun produces a stable electron beam that accelerates the electrons to an energy range of 0.1-30 keV (Zouh, 2007; Chen, 2015). The electron beam is focused by magnetic fields produced by coils of wires and can be magnified and demagnified using electron lenses (Zouh, 2007). As the electron beam interacts with the samples, the electron can either be inelastically scattered or elastically scattered. Inelastic scattering are the low energy electrons that only reach the sample surface before being emitted, which creates secondary electrons (SE). Elastic scattering produces backscattered secondary electrons (BSE), which is produced by incident electron scattering by the nucleus of the sample (Chen, 2015). BSE imaging was used to analyse the samples in this study. Each sample was carbon coated before being analysed in the SEM. The thin sections are non-conductive, and without any metal coating they would accumulate charge during electron bombardment. By coating with a conductive metal like carbon this is avoided, and the signal is improved (Zhou, 2007). Once coated, the sample is placed on the specimen stage, which is inside a vacuum chamber. The vacuum chamber is crucial for the SEM in order to avoid scattering on the electron beam

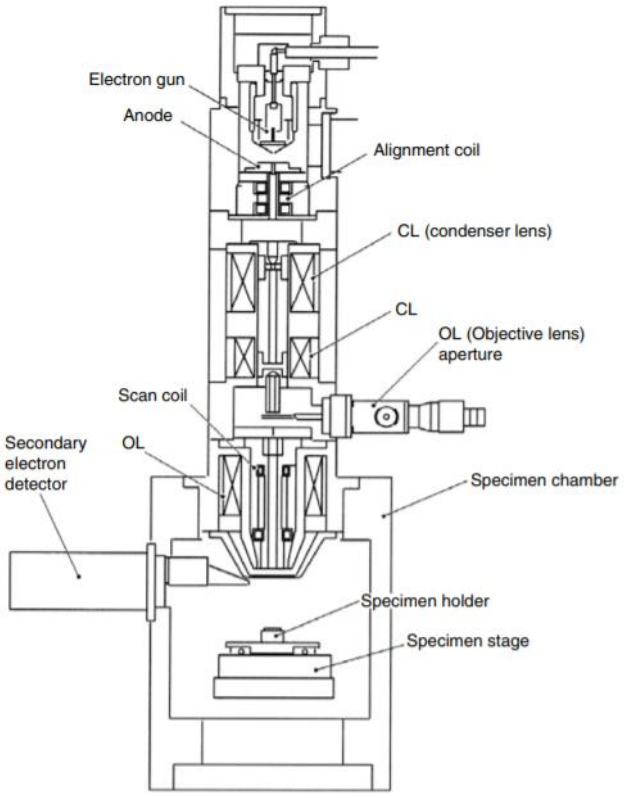

Figure 4.2: A schematic figure of the main components of the scanning electron microscope (SEM). It is comprised of an electron gun at the top, a series of electromagnetic lenses and apertures, a vacuum pump system and a specimen chamber. From Zouh (2007).

as well as contamination of the electron gun (Zhou, 2007). As the beam hit the sample material, the elastic collision between an electron and the specimen atomic nucleus causes the electron to bounce back. An element with higher atomic number has more positive charges on the nucleus, causing more electrons to be backscattered and absorbed as signals by a detector (Zhou, 2007). The signals are then converted to images, where the greyscale contrast in the BSE images reflect the distribution of heavy or light elements. This allows for easy differentiation of minerals (Chen et al., 2015). The SEM was used to collect images that illustrated the porosity and grain size in both the host rock and the deformation bands, as well as images of the deformation of coal.

4.3 Digital Image Analysis

In order to quantify the evolution of the deformation bands it is necessary to know how the microstructures in terms of porosity and grain size change along dip of the band and compare that to the microstructures of the host rock. Analysis of porosity and grain size was achieved using digital image analysis on BSE-SEM images with the use of a program called ImageJ, a digital image analysis software., Because blue epoxy was not injected into the thin sections, it was difficult to apply the same concepts to photomicrographs as the grain boundaries were not distinct enough. Therefore, BSE-SEM images were the only images that were analysed for porosity and particle size distribution.

4.3.1 Porosity in BSE-SEM images

Multiple locations inside the deformation bands and outside the deformation bands were chosen to measure porosity. BSE-SEM images were taken at magnifications between 100-130x, which were subsequently analysed using ImageJ. The DIA workflow in ImageJ is depicted in a schematic flow chart in Figure 4.3. The BSE-SEM images were converted to 8-bit greyscale images in order to apply a threshold that would separate the pore space from the grains. The pore space is represented by black colour in the BSE-SEM images and grains by different shades of grey. By carefully adjusting the threshold while comparing to the original image, the pore space was highlighted in red. Once the threshold was satisfactory the image was converted to a binary image where pore space is represented by black and the ratio between pore space and grains is measured.

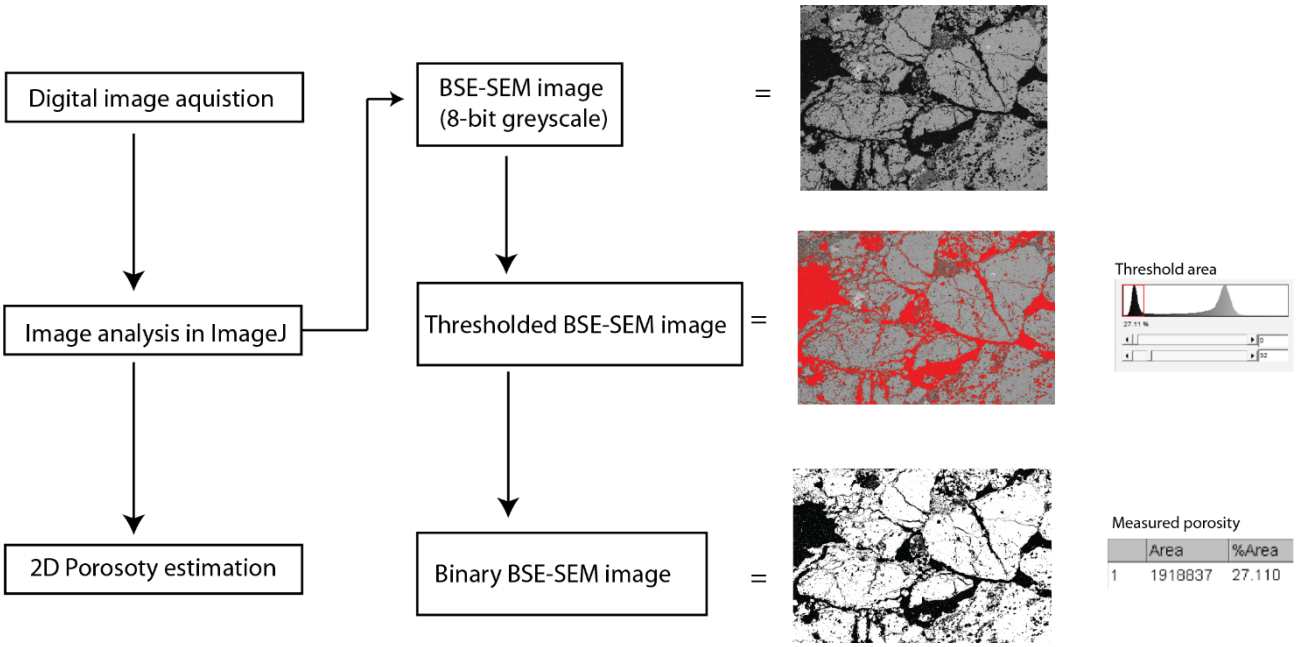

Figure 4.3: Flowchart depicting 2D porosity estimation from 8-bit gray scale BSE-SEM images using ImageJ. The pore space appears as black in the 8-bit images and the grain as different shades of grey. The pore space in the threshold image appears as red. This method is used to calculate the total 2D porosity in an image. Modified from Thorsheim (2015).

4.3.2 Particle size distribution in BSE-SEM images

ImageJ was also used to quantify the particle size distribution. Two locations were chosen for each sample, one inside the deformation band and one from the host rock. Three images were taken from the same location at magnifications of 130x, 500x and 1000x in order to include the full range of grain size. The workflow in ImageJ is depicted in a schematic flow chart in Figure 4.4. The BSE-SEM images were converted to 8-bit greyscale images in order to apply a threshold that would separate the quartz and feldspar grains from pore space and phyllosilicates. Phyllosilicates mainly appear as a darker shade of grey in the BSE-SEM images, so the threshold was carefully adjusted to single out the right shade of grey that represented the quartz and feldspar. Once content with the separation of the grains the image was converted to a binary image, where grains appear black. The binary image was stacked with the original image in order to be cleaned for unwanted mineralogy such as phyllosilicates and coal. Careful erasing of pixels from merged grain boundaries was done for instances where ImageJ had not been able to differentiate between two separate grains. Each grain was separated in a satisfactory way and the particle size area (PSA) of the grains was calculated. The grains in pixels were calibrated in square micrometre by setting the real scale on each image.

The measured PSA was then used to create a particle size distribution plot where the exceedance frequency (EF) was plotted versus the PSA. The EF of a particular value of a particle size is defined as the number of data with values greater than that value, divided by the total number of the data (Torabi et al., 2007). EF was plotted versus PSA of both the host rock and deformation band to compare their particle size distribution. The particle size distribution can be described by a power law with dimension D (exponent) (Torabi et al., 2007). The calculated D-value is two dimensional but can be converted to a three dimensional by adding 1 to its value (Sammis et al., 1987; Blenkinsop, 1991). A plot was made for each sample in both sample sets and were used to analyse the change in grain size with respect to changes in thickness of the deformation band cluster and evolving displacement in the single deformation bands.

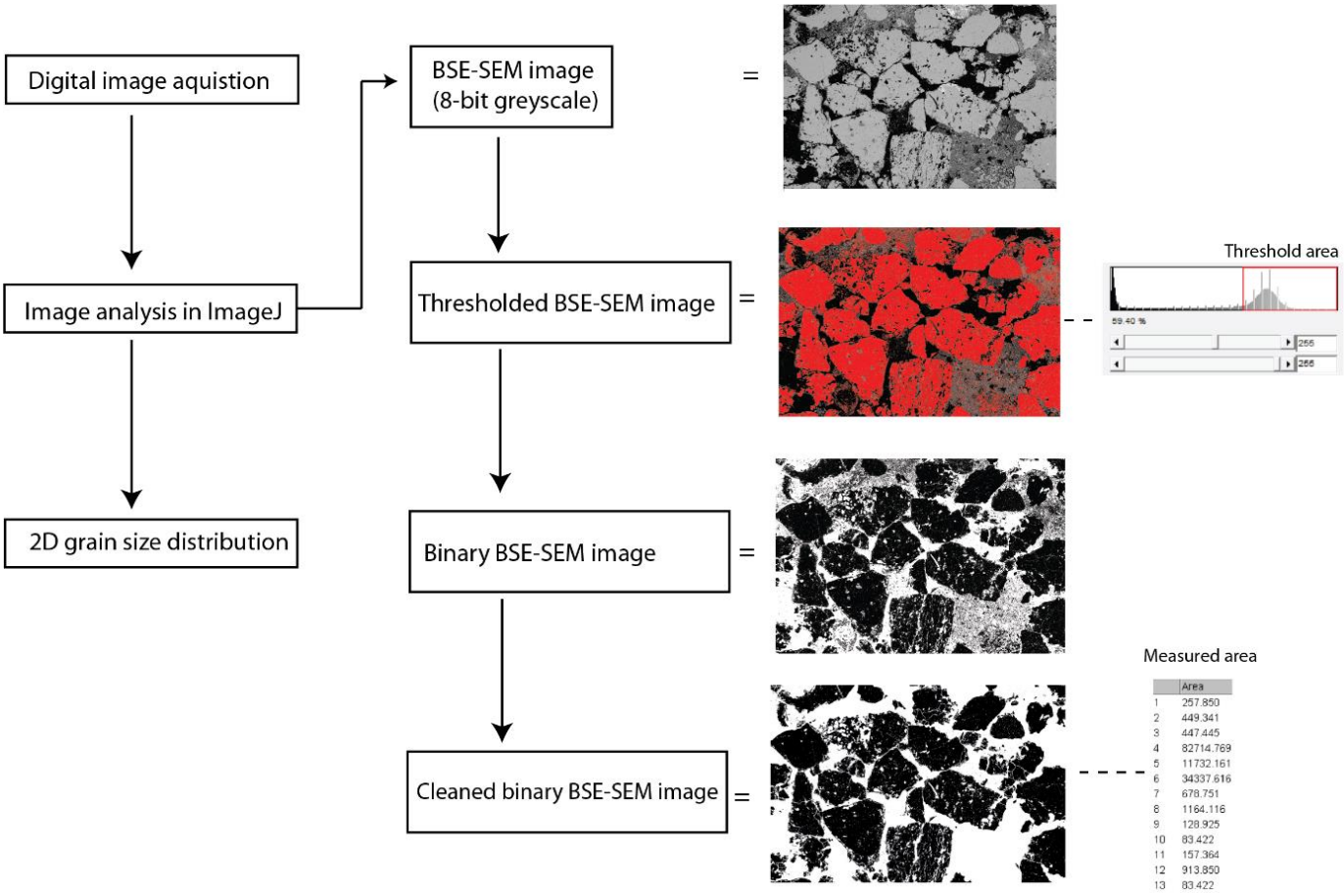

Figure 4.4: Flowchart depicting 2D grain size area calculations from BSE-SEM images using ImageJ. The method measures the grain size area by pixel counting on a binary image after several steps of thresholding has been applied. The grains are shown as black in the binary BSE-SEM image. Modified from Thorsheim (2015).

4.4 Sources of error

Various limitations and sources of errors can occur when calculating 2D porosity from thin sections. Thin sections are 2D projections of a 3D sample and this can lead to misrepresentation of clast and pore size based on their geometric distribution. The thin sections are 30μm thick and whether grains are situated at the top or the bottom of the thin section is considered random. This may lead to an over or underrepresentation of grains and pores in optical microscope. This problem was avoided by measuring porosity from BSE-SEM images as only the top μm of the thin sections is penetrated by the electron beam in the SEM. Therefore, the problem of grain distributions in thin sections are not transferred to the BSE-SEM images.

Another potential source of error could have occurred when preparing the samples. When the samples were cut and polished in preparation for thin sections the deformation bands in the hand sample were fragile and small particles would fall out before resin was reapplied. When investigating the samples in optical microscope and SEM it was therefore important to rule out whether the large pore space in the deformation band was natural or a result of fallout from the preparation process.

5 Results

This chapter will present the results from the field work survey, as well as the digital image analysis (DIA) of the BSE-SEM images of the deformation bands and coal rich layers. The first section will include a description of the outcrop and structural data collected in the field such as orientation and dip of bedding, marker layers, deformation bands and lineations (when present). The second section will present the results from the digital image analysis of the two sample sets with particular focus on the change of grain size and porosity measurements in both the host rock and deformation band. Finally, it will present the digital image analysis of the coal found in both sample sets and look closer on the effect the coal has on porosity.

5.1 Field observations

The outcrop of interest is a 3.5 m high cliff face located at Wangaloa Beach, Dunedin. It is composed of a well-sorted, medium to coarse-grained quartz sandstone that belongs to the top member of the Taratu Formation (Fig. 5.1a). Within the sandstone, 2-30 mm thick layers of mud and coal can be found interbedded with the sandstone. Bedding planes were measured from these layers, showing a strike with a strong W-E trend, and a very shallow dip of around 5° north (Fig. 5.2). The layers can be discontinuous with a lateral extension ranging between 10-40 cm or as coherent layers with a length up to 1.5 m. A 23 mm thick mud layer is found at the bottom of the outcrop which shows an undulating base

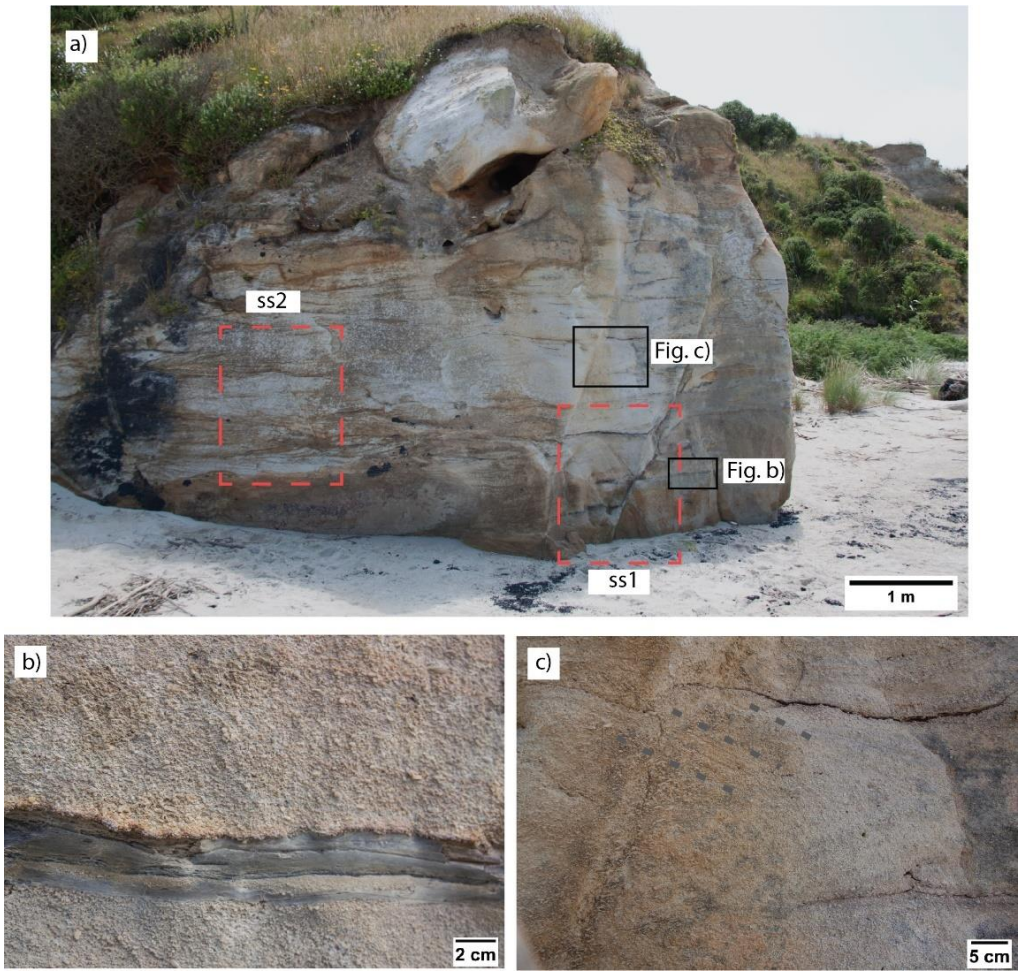

Figure 5.1: Photos from the outcrop at Wangaloa beach. a) The outcrop of interest. Ss1= sample set 1, ss2= sample set 2.b) Mud layer where overlaying sand has eroded into the top. c) Cross bedding dipping towards east located below the thin coal layer.

and a sharp, erosive upper contact (Fig. 5.1b). Repetitive cycles of upward grain size coarsening are present, with the outcrop showing an overall upward coarsening trend testified by a larger amount of pebbles (> 8 mm in size) being more common towards the top. Cross bedding with a dip direction towards the NW is present above a 24 mm thick coal seam (Fig 5.1c). However, cross bedding further up the formation is dipping towards the NE. Several small-scale faults and deformation bands were mapped along and within five metres from the main outcrop. Figure 5.2 shows a stereonet with the collected structural data. Faults and deformation bands are organised in two N-S conjugate sets dipping c. 60-70° towards E (more common) or W. Two faults showed the occurrence of slickenlines with a plunge of 62 ° east and 57 ° west and with a normal sense of slip, confirmed also by offset of marker layers in the outcrop (See also Fig. 10 and 11).

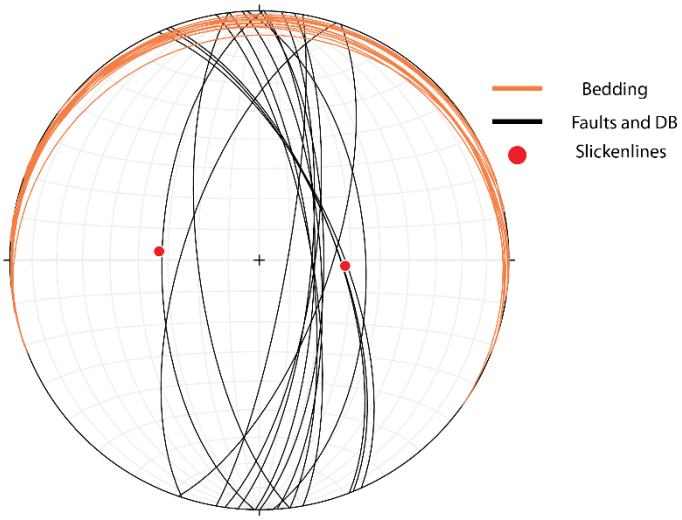

Figure 5.2: Stereonet of the recorded structural data from the outcrop located at Wangaloa Beach.

5.2 Sample set 1

Two sample sets were collected along two different deformation bands/clusters of deformation bands. Sample set 1 was collected along a deformation band cluster with orientation 181/60° (Fig 5.3). The deformation band cluster forms the damage zone of the hanging wall of a well-defined fault surface displaying slickenlines (Fig. 5.4). The cluster of bands appear as a pale coloured zone that visibly offsets a mud and a coal layer (Fig. 5.3). The mud layer shows a 30 cm displacement, and the coal layer shows a 24 cm displacement with a component of horizontal extension due to shearing from the individual bands in the cluster. The cluster of deformation bands extends from below the lower mud layer until it tips out ca. 50 cm above the upper coal layer. The thickness of the cluster thins when approaching the mud layer before increasing in both directions away from the mud layer going from 4 mm to 12 cm. Seven samples were analysed as part of sample set 1 and these were collected at increments of increased thickness of the cluster. Table 5.1 shows the thickness and the bulk strain of the deformation

Table 5.1: The measured thickness and bulk shear strain of the deformation band cluster in each sample.

Sample	*Thickness*	*Bulk strain*
W1	4-12 mm	3
W2	20 mm	1.2
W3	24-26 mm	1.06
W4	27-42 mm	0.72
W5	42-50 mm	0.56
W6	Footwall	NA
W7	60mm	0.4

band cluster for each sample collected. Bulk strain ($\gamma = \frac{d}{t}$, where d is displacement and t is thickness) was calculated for a displacement of 24 mm.

Figure 5.3: Picture of the studied location of sample set 1 and from where the samples were collected along the band. The red lines are deformation bands, and the cluster of interest is highlighted as a red zone. Black lines show the coal and mud layers that have been displaced. Photographs of each hand sample collected is included. The deformation bands in the hand samples are visible as slightly lighter colored bands.

All samples were collected from the damage zone at the hanging wall of the fault, with exception for W6 that was collected from the damage zone at the footwall (Fig. 5.3). The deformation bands are visible in the hand samples as slightly lighter coloured bands with a visible reduction in grain size. Sample W1 contains a slip surface with slickenlines. There is clear evidence of shear-induced rotation in samples where coal is present, particularly in sample W5 (Fig. 5.3). The lower half of the footwall has a prominent orange colour which is interpreted to be staining from fluids. Sample W1 and W2 show how the staining is confined to the host rock, hence form a sharp contact between the host rock and the cluster of bands (Fig. 5.3).

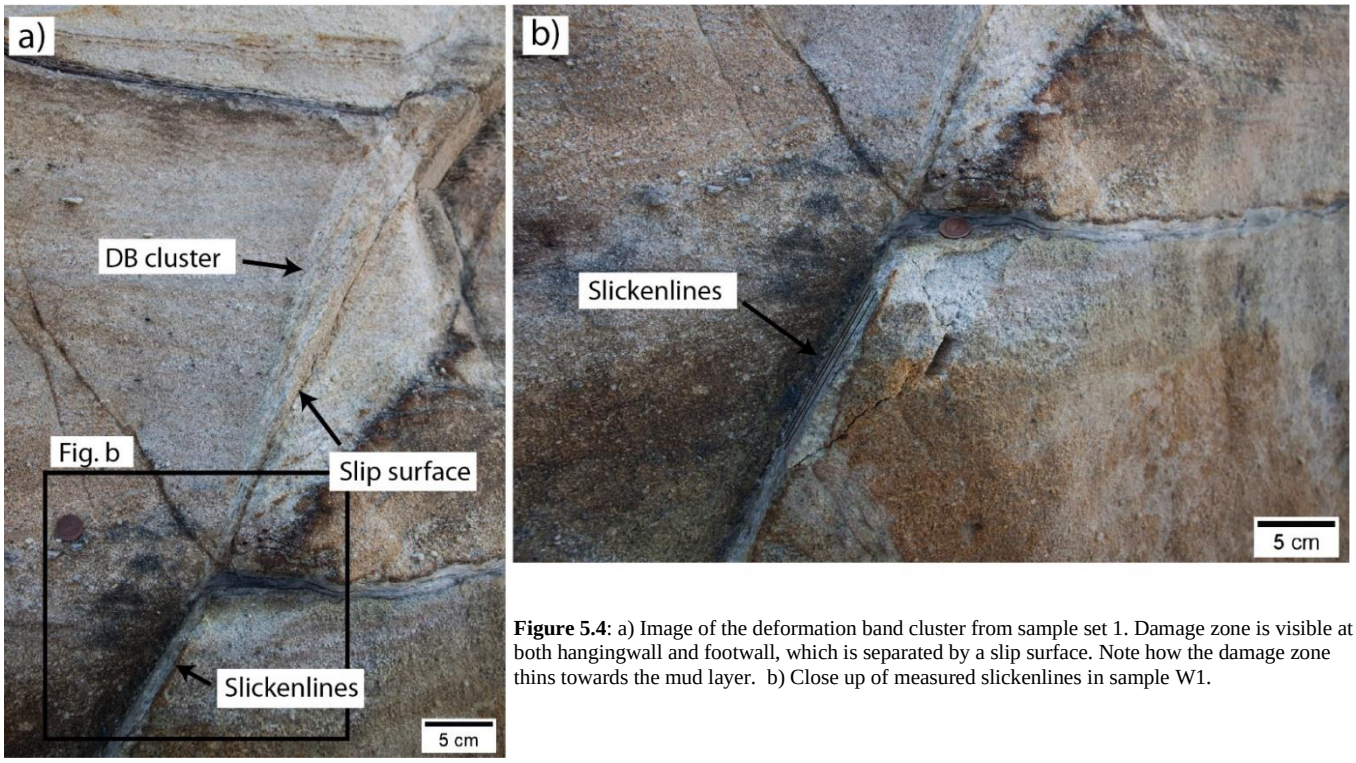

Figure 5.4: a) Image of the deformation band cluster from sample set 1. Damage zone is visible at both hangingwall and footwall, which is separated by a slip surface. Note how the damage zone thins towards the mud layer. b) Close up of measured slickenlines in sample W1.

When investigating the samples under the optical microscope and SEM the deformation bands can be distinguished from the host rock in terms of grain size and pore space variability. Figure 5.5 shows how microstructures may differ inside and outside of the deformation bands in the case of sample W3 (see red lines in Fig. 5.5b delineating the inferred boundaries of the deformation bands). The main observations are visible increased pore space and grain size reduction inside the deformation bands (Fig. 5.5b), and these observations are seen in all samples. Both the host rock and the deformation bands show grain fracturing, mostly intragranular fractures, while grain flaking is mainly observed inside the deformation bands. Grain flaking along clast boundaries results in angular, elongated smaller particles that form a fine-grained matrix (c. 0.8-5 μm in size) in between large survivor grains. Intergranular fractures are only seldomly detected. The grade of fracturing of the host rock is visibly less

intense compared to the deformation bands, with the number of large grains (1-2 mm) being strongly reduced inside the deformation bands (Fig. 5.5c-d).

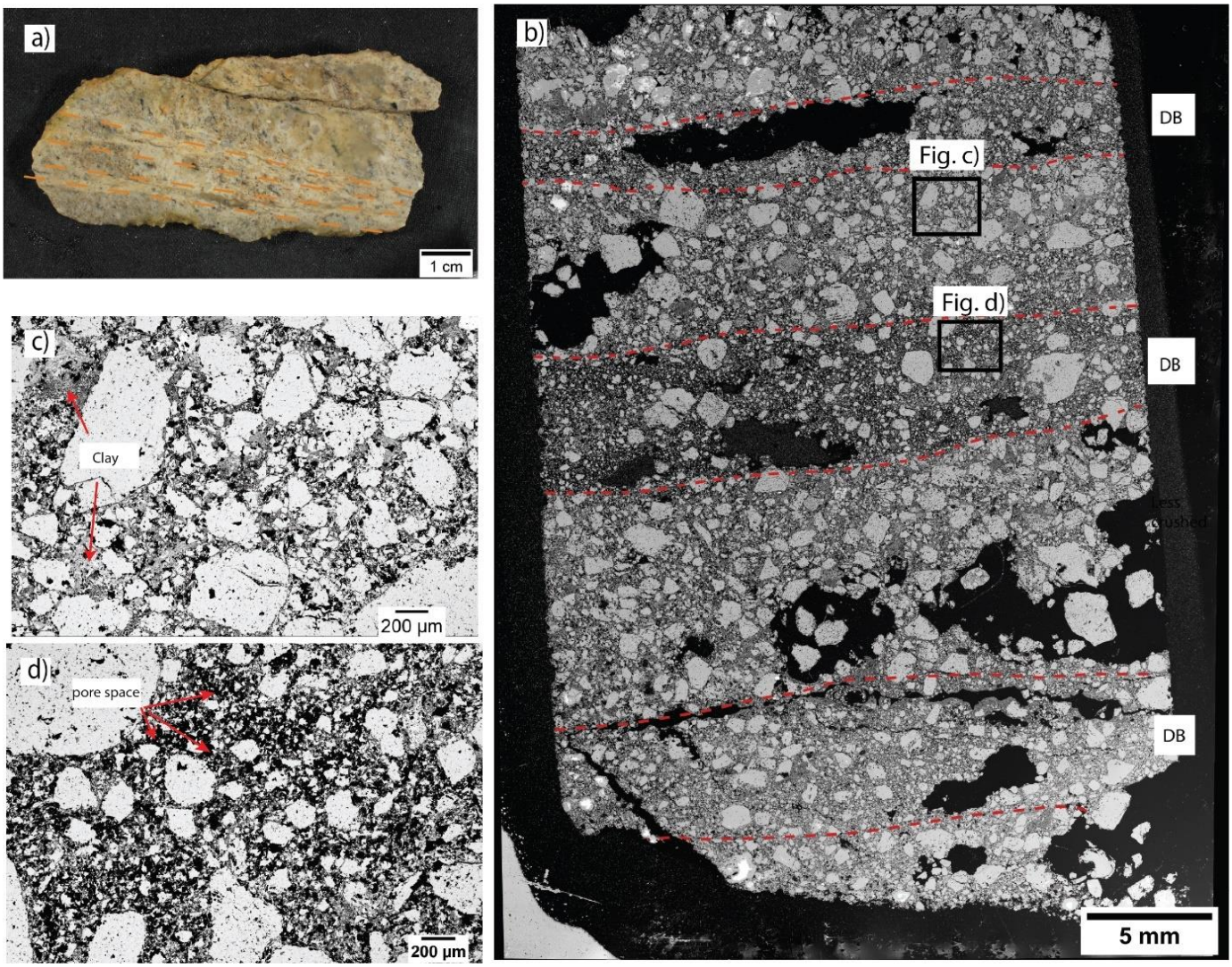

Figure 5.5: a) Sample W3 showing 4 distinct deformation bands; b) BSE SEM have been stitched together to create a mosaic of W3. Red dotted line infers the boundaries of the deformation bands; c) Higher magnification image of the host rock with larger clay fields; d) higher magnification image of deformation band with visibly increased pore space.

An exceedance frequency plot was made for all thin sections containing deformation bands in order to quantify the difference in particle size area (PSA) between the host rock and deformation bands (Fig. 5.6). The EF plots from sample W1-W7 show that there are minimal differences between the host rock and deformation band curves of sample W1, W2 and W4. Sample W3, W5, W6 and W7 show a small shift of the host rock curve towards the right, confirming the observations of the host rock having a larger particle size. The measured D-values of all the analysed samples are similar and relatively low, ranging from 1.785 to 1.871 (Fig. 5.6). In general, there is a positive correlation between the measured D-value and the intensity of cataclasis: meaning a higher D-value indicates higher intensity of cataclasis

(Rotevatn et al., 2008). All plots show high similarity between the steepness of the two curves representing the host rock and the deformation band. This similarity implies that the proportions of grain size do not change from the host rock to the deformation band, showing that there is little correlation between intensity of cataclasis and thickness of the cluster of bands.

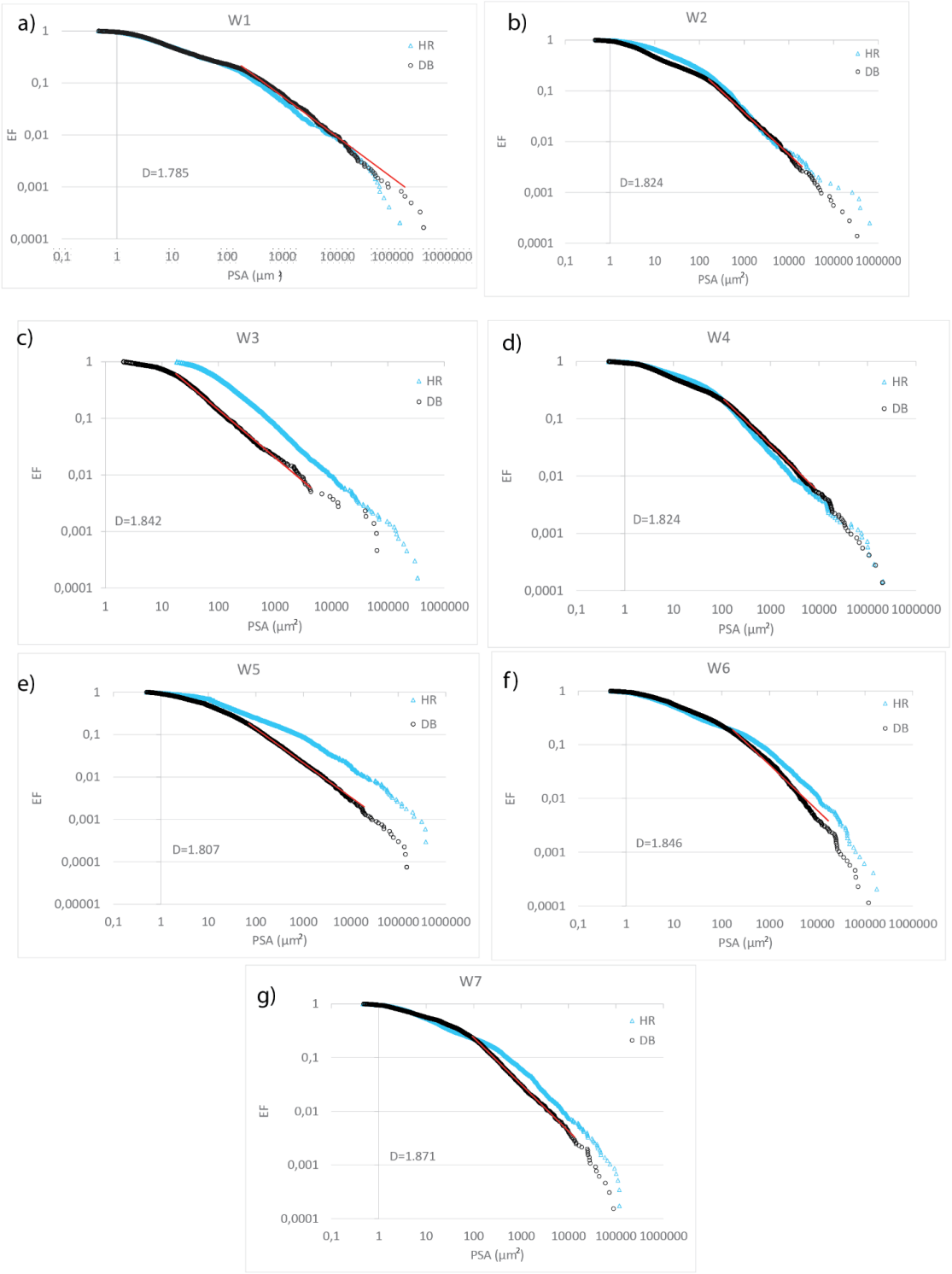

Figure 5.6: Particle size distribution plots from host rock and deformation in each sample in sample set 1. Exceedance frequency (EF) is plotted against particle size area (PSA). Power of law dimension D (D-values) have been plotted for the steepest curve of the deformation band.

Figure 5.5c-d shows the difference in porosity (seen as black areas) between the deformation bands and the host rock, with a visibly higher amount of pore space occurring in the bands. Phyllosilicates are present in both host rock and deformation band and occur as infilling in the pore space. There is a noticeably higher amount of phyllosilicates in the host rock. No prominent alignment of clay minerals with the shearing direction is found within or surrounding the deformation bands. These observations are the general trend seen in all the samples. Figure 5.7 is from W5, and like W3, the deformation bands are characterised by higher amounts of pore space and grain size reduction while the host rock contains larger clay zones filling the pore space.

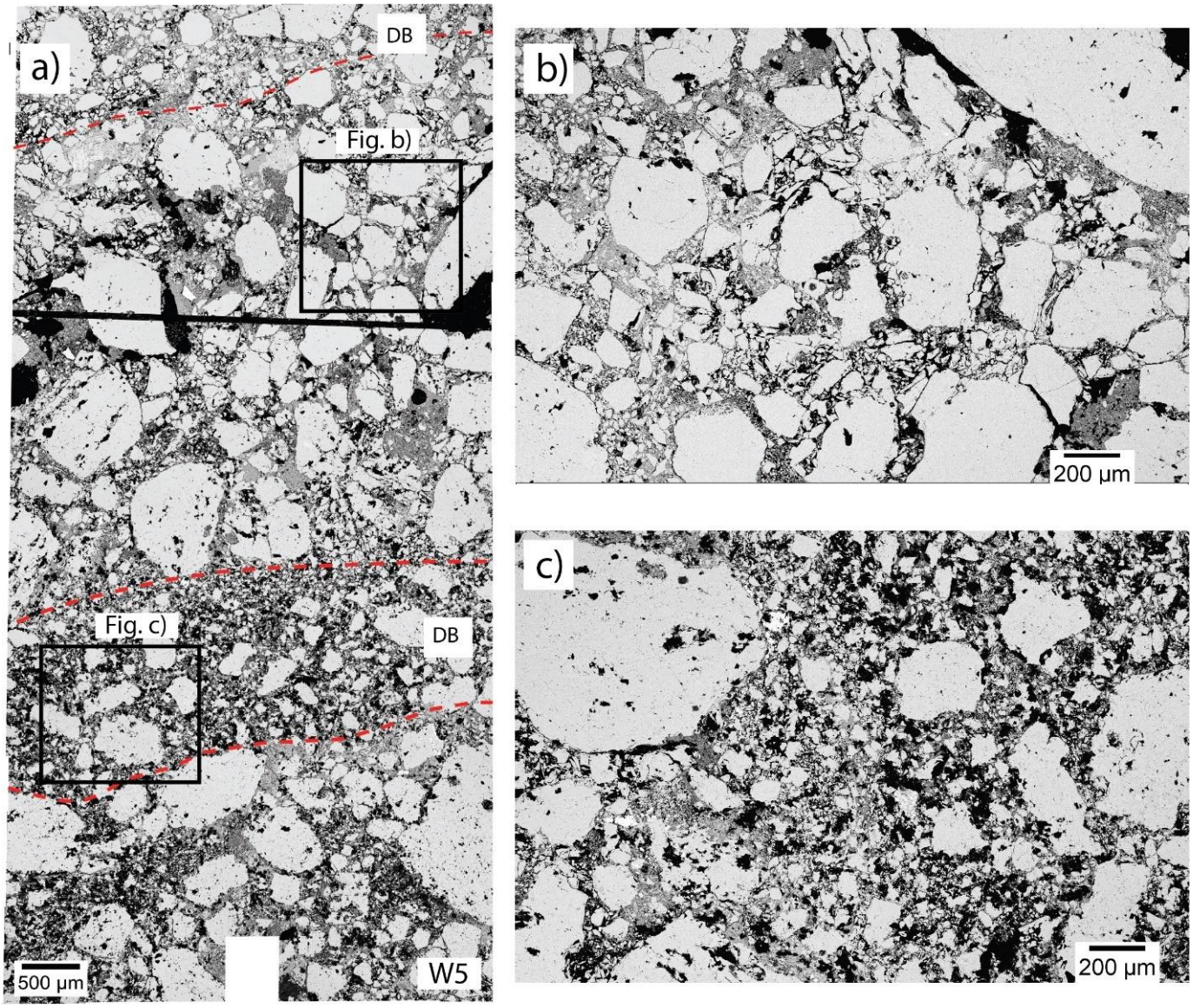

Figure 5.7: BSE images from W5. a) mosaic of several BSE images showing the deformation bands (red dotted line) and the host rock. b) higher magnification image of host rock with high amounts of phyllosilicates. c) higher magnification image of deformation band with increased pore space similar to W3.

Porosity measurements from all samples are shown in a box plot in Figure 5.8. There is a large variation of porosity between the samples, with no particular correlation with the degree of cataclasis. Porosity is higher in the deformation bands of most samples apart from in W1 and W4. Sample W4 and W7 show high porosity both within the host rock and the deformation band, with mean porosity in the band being 28 % and 33 % respectively and 30% and 28% in the host rock (Fig. 5.9a-b). Sample W1, W2 and W5 have a low porosity relative to sample W4 and W7, with the mean porosity in the band being 11 %, 24 % and 23 % respectively and 14 %, 17 % and 15 % in the host rock respectively (Fig. 5.9c-f). Observations from SEM images show that W1 and W2 contain cement in the intergranular pore space and high amounts of phyllosilicates in the host rock (Fig. 5.9d-e), while W5 has high amounts of phyllosilicates (Fig. 5.9f). The various amounts of phyllosilicates and cement present in the host rock contributes to the large spatial variation of porosity.

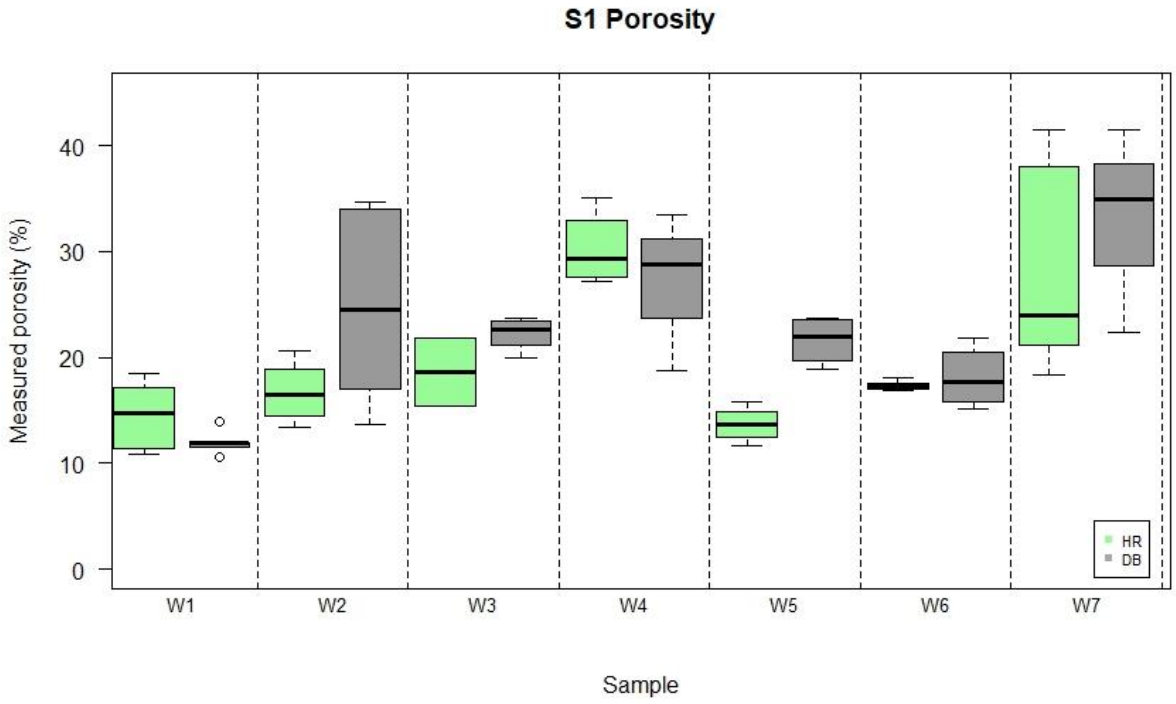

Figure 5.8: Box plot of measured porosity from BSE images of both host rock and deformation band in sample set 1. The boxes represent interval measurements from the 2nd to 3rd quantile, with the mean porosity being represented by the black horizontal line. The dashed line represents the interval between the maximum and minimum measured value.

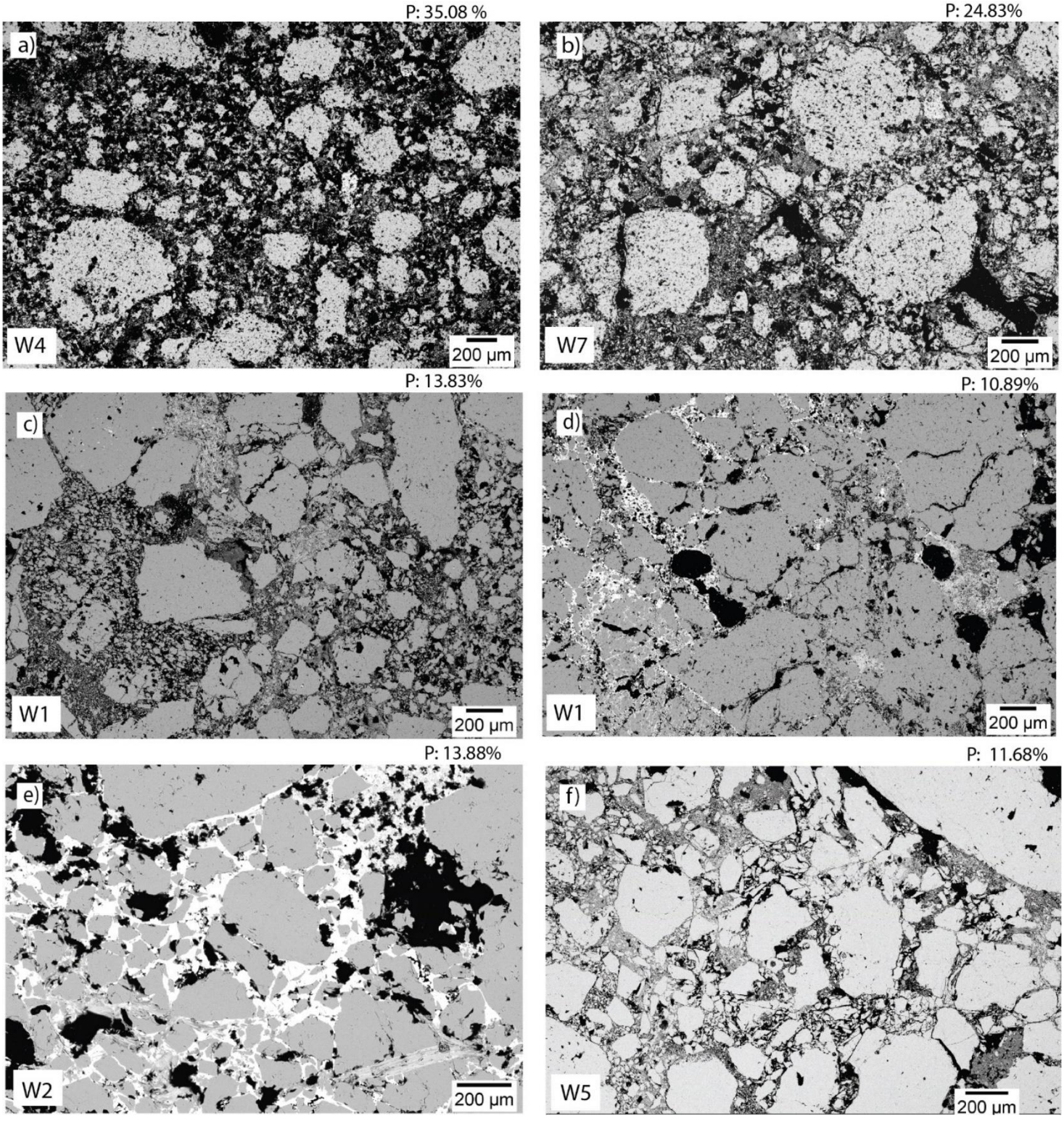

Figure 5.9: BSE images of host rock in different samples that show various amount of porosity. Porosity measurements are written on top of images. a-b) W4 and W7 having high porosity due to high amounts of pore space. c-d) W1 having low porosity due to phyllosilicates and cement. e) W2 having low porosity due to cement. f) W5 having low porosity due to large fields of phyllosilicates. Note the large variation of black pore space in each image.

The clay minerals that are typically observed in both the host rock and the deformation bands are kaolinite and kaolinite-muscovite intergrowth (Fig. 5.10). The kaolinite is found as stacked aggregates, also known as kaolinite booklets (Fig. 5.10a), or as pore filling cement. Kaolinite booklets are randomly oriented in pore space and are commonly truncated by adjacent booklets. Crystals of kaolinite booklets in the host rock are larger than the ones in the deformation bands, measuring from up to 21 µm wide and < 1µm thick (Fig 5.10a) while crystals of kaolinite booklets in the deformation band typically measure up to 10 µm wide and <1 µm thick (Fig. 10b). There is a higher abundance of kaolinite in the host rock than inside the deformation bands (Fig. 10a and b). Kaolinite booklets are not related to minerals such as feldspar that would suggest a replacement reaction, rather they occur in large pore space between quartz grains. The muscovite is generally found as elongated crystals that are intergrown with kaolinite (Fig 10c). They too occur as pore filling crystals that are truncating each other and with random orientations. Muscovite-kaolinite crystals are larger than the kaolinite booklets, being up to 0.1 mm in length. Figure 10c show locations of element scanning done by the SEM and their element spectrum. The element spectrum of location 1 is reflective of the chemical formula of kaolinite ($Al_2Si_2O_5(OH)_4$) while the element spectrum of location 2 is reflective of the chemical formula of muscovite ($KAl_2(AlSi_3O_{10})(F,OH)_2$

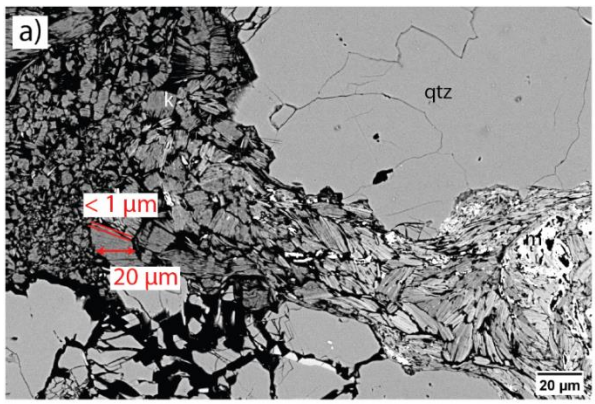

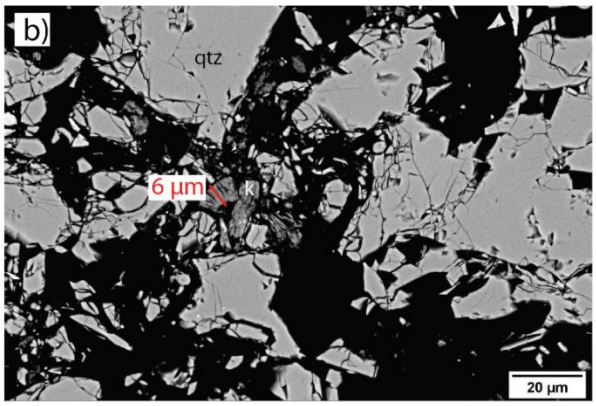

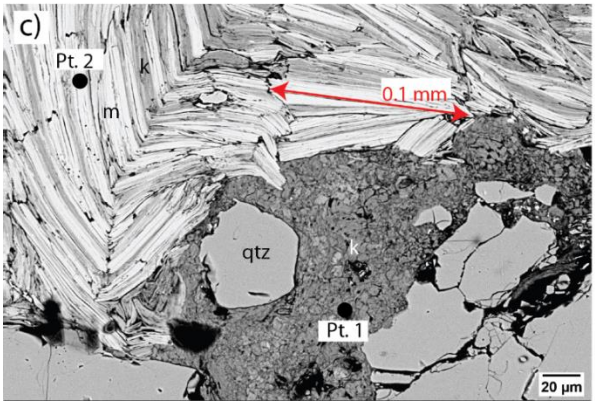

	C	O	Mg	Al	Si	K	Fe
Pt. 1	8.39	47.02	0.25	21.15	21.18		2
Pt. 2	3.27	47.14	1.86	13.56	23.16	9.12	2.89

Figure 5.10: a) BSE-SEM image of pore filling kaolinite (k) booklets in between quartz grains (qtz) in host rock of W5. b) BSE-SEM image of kaolinite booklets inside the deformation band of W5. c) BSE-SEM images of pore filling muscovite (m) and kaolinite in host rock of W5. Pt. 1 and Pt.2 are locations of element scanning, with the weight of atoms presented in the table.

5.3 Sample set 2

Sample set 2 is collected along two separate deformation bands with an orientation of 008/70° and 005/73°. The deformation bands are mainly visible due to displacement of multiple coal layers (Fig. 5.10). In the field the deformations have a slightly lighter colour than the surrounding host rock but become difficult to detect towards the top and base of the outcrop as no layers are visibly offset.

Nine samples were collected along two separate deformation bands (Fig. 5.11). Samples W10-W13, W15 and W16 were collected along one band referred to as DB1, while W14, W17 and W18 were collected from an adjacent band referred to as DB2 (Fig. 5.11). Samples from DB1 are used to describe the changes in microstructure with different increments of displacement, while samples from DB2 are used to investigate the coal deformation. The displacement along the deformation band is clearly visible in hand samples where coal has been displaced (Fig. 5.11). Table 5.2 lists the thickness, displacement, and bulk strain of each sample. The thickness of the deformation band ranges between 1.6-4.3 mm and appears to reach its maximum thickness towards the central part of the band along dip where the measured displacement is larger. No displacement is measured in W13, W15, W16 and W17 due to lack of offset layers. The full lateral extent updip and downdip of the deformation bands is not known, as it covers the whole extension of the outcrop. Sample W10, W11, W12, W14 and W18 have distinct coal layers that have been smeared by the deformation band, which allows for more precise measurements of displacement. Bulk strain is calculated in samples where both thickness and displacement are known.

Sample	Thickness	Displacement	Bulk strain
W10	2.6 mm	12.6 mm	4.84
W11	5.1 mm	11.8 mm	2.3
W12	2.4 mm	11 mm	4.58
W13	1.6 mm	NV	NA
W14	3.3 mm	12.2 mm	3.69
W15	1.9 mm	NV	NA
W16	1.8 mm	NV	NA
W17	4 mm	NV	NA
W18	4.3 mm	19.8 mm	4.6

Table 5.2: Measured thickness, displacement and bulk strain in each sample. Bulk strain is calculated from displacement/thickness. NV = Not visible, NA = not applicable

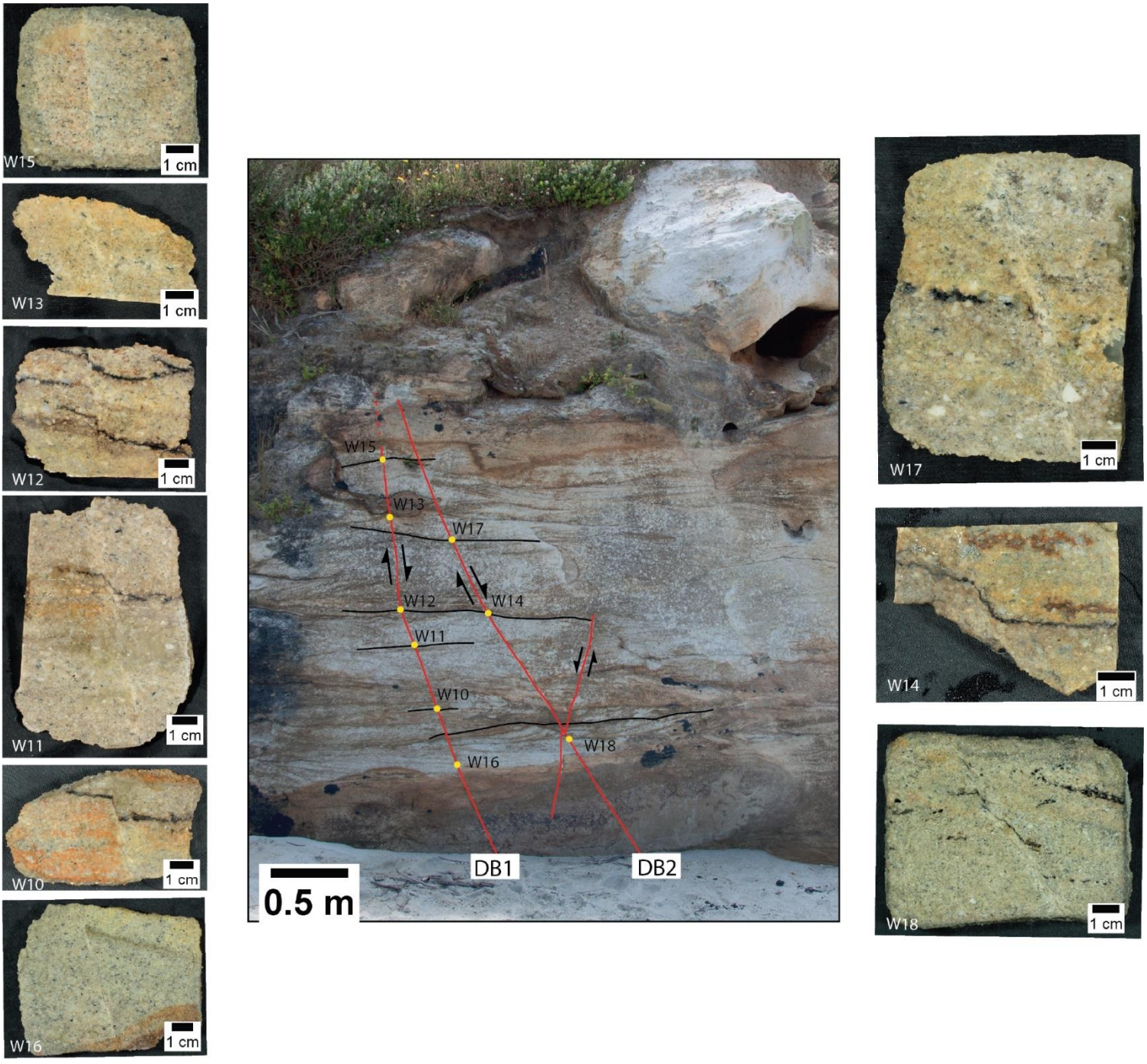

Figure 5.11: Picture of the studied location of sample set 2 and from where the samples were collected. Red lines indicate the location of the deformation bands. Pictures of all the samples are included. Note how the displacement is visible in samples that contain thin coal layers.

The deformation band in sample set 2 is characterized by having a visible grain size reduction compared to the host rock (Fig. 5.12). Observations from optical microscope reveal that the number of larger grains (1-2 mm in size) in the band is reduced (Fig 5.12b). The thickness of the band has a large spatial variation over short distances which can be seen in Figure 5.12b. The grain size reduction inside the band is seen in all samples of sample set 2. Fracturing is observed in both host rock and deformation band, but with a higher intensity inside the deformation band. Fractures are mainly intragranular, with minor grain flaking along some clasts (Fig 5.13a-b). As a result, larger survivor grains (0.2-0.9 mm) are typically surrounded by a fine-grained matrix (0.5-7 μm in size) and phyllosilicates (Fig. 5.13c). Intergranular

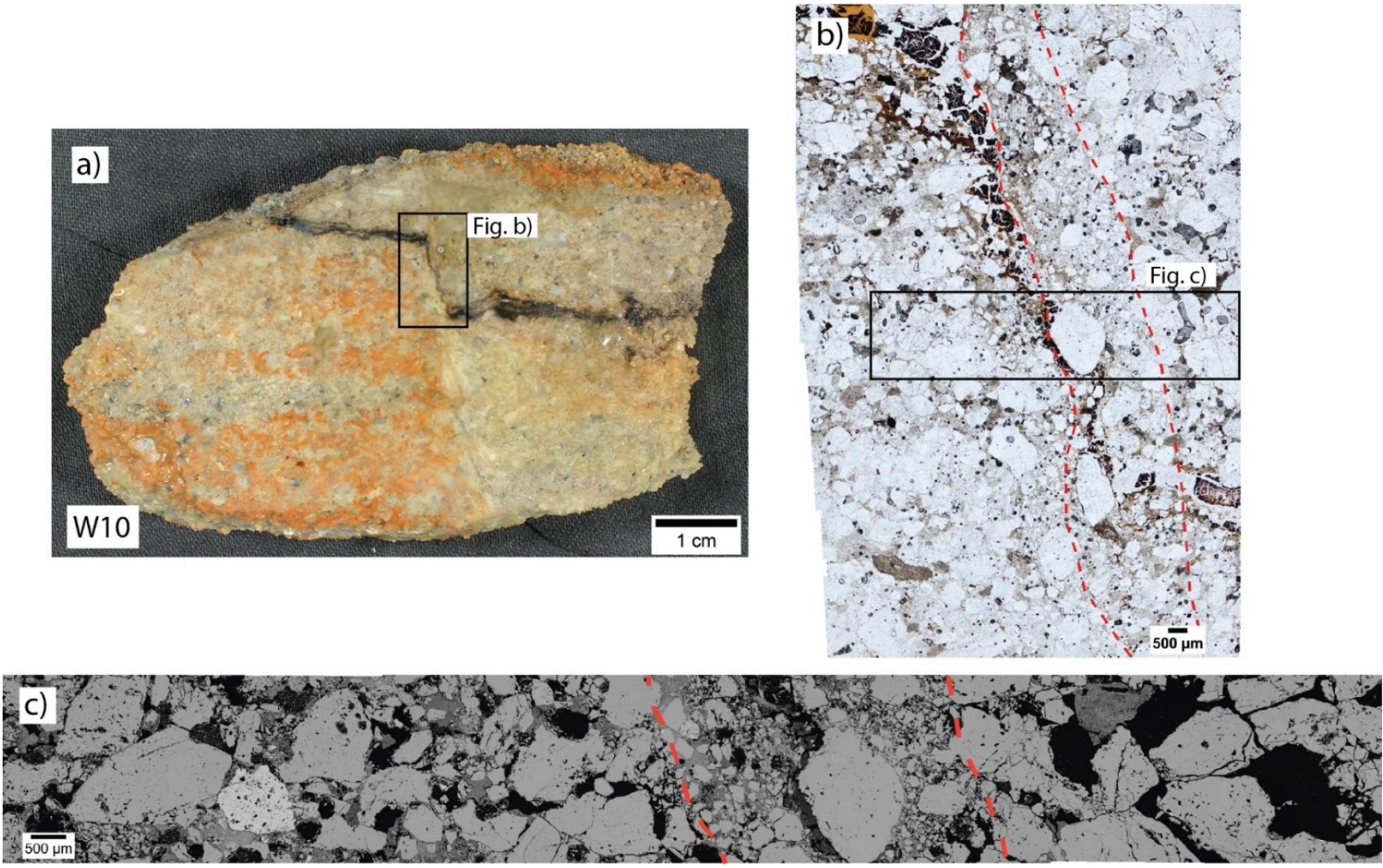

Figure 5.12: a) hand sample of sample W10. Deformation band is visible as a pale colored band offsetting the coal layer. b) optical microscope image from sample W10. Deformation band is outlined by red dotted lines. c) BSE-SEM image from sample W10.

fractures are rare in both host rock and deformation band. Fig. 5.14 shows a comparison of BSE-SEM images from the host rock and deformation band from each sample, as well as their particle size distribution. The particle size distribution curve of the deformation bands is commonly steeper and shifted towards the left with respect to the host rock, confirming the observations of grain size reduction inside the deformation bands. The D-values are high in sample W10, W11 and W12 (1.86-1.96), while W13 and W15 show lower D-values (1.76-1.79). Even though the variation is not significant this indicates that a higher degree of cataclasis occurred towards the centre of the band along dip (Fig. 5.15). The particle size distribution curves for the host rocks usually show a kink towards the right tail, thus indicating a frequency increase of larger grains in the host rock. Both SEM images and the PSD plots in Figure 5.14 show that there is a variation of largest grain size in the host rock. W12 shows grain sizes up to 2mm in diameter (long axis) while W13 shows grain sizes up to 0.9 mm (Fig. 14).

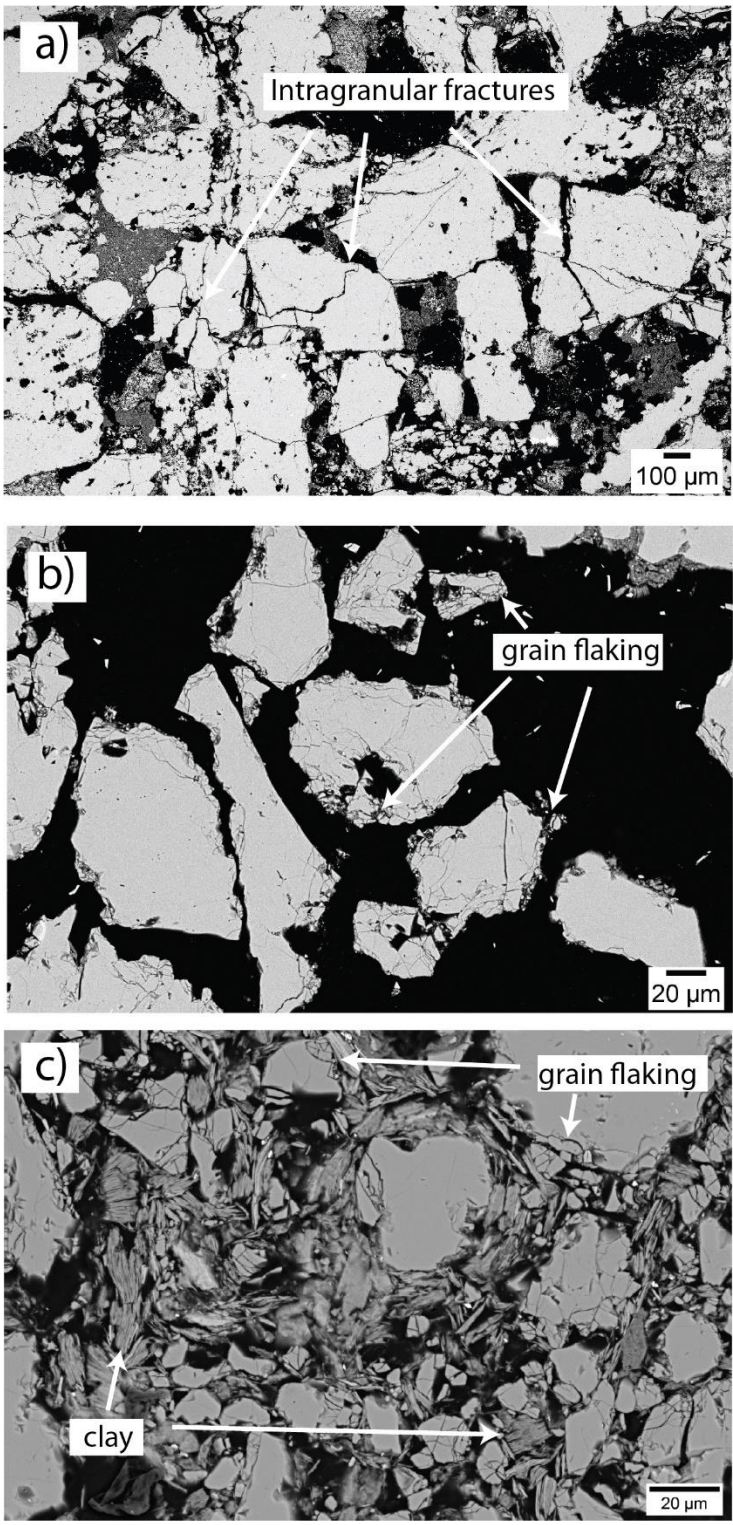

Figure 5.13: BSE images displaying the different fractures found in the host rock of the samples. A) intragranular fractures from the host rock of sample W11, b) grain flaking at grain boundaries of the host rock of sample W12. c) fine-grained matrix in host rock of W10. Clays are infilling pore space.

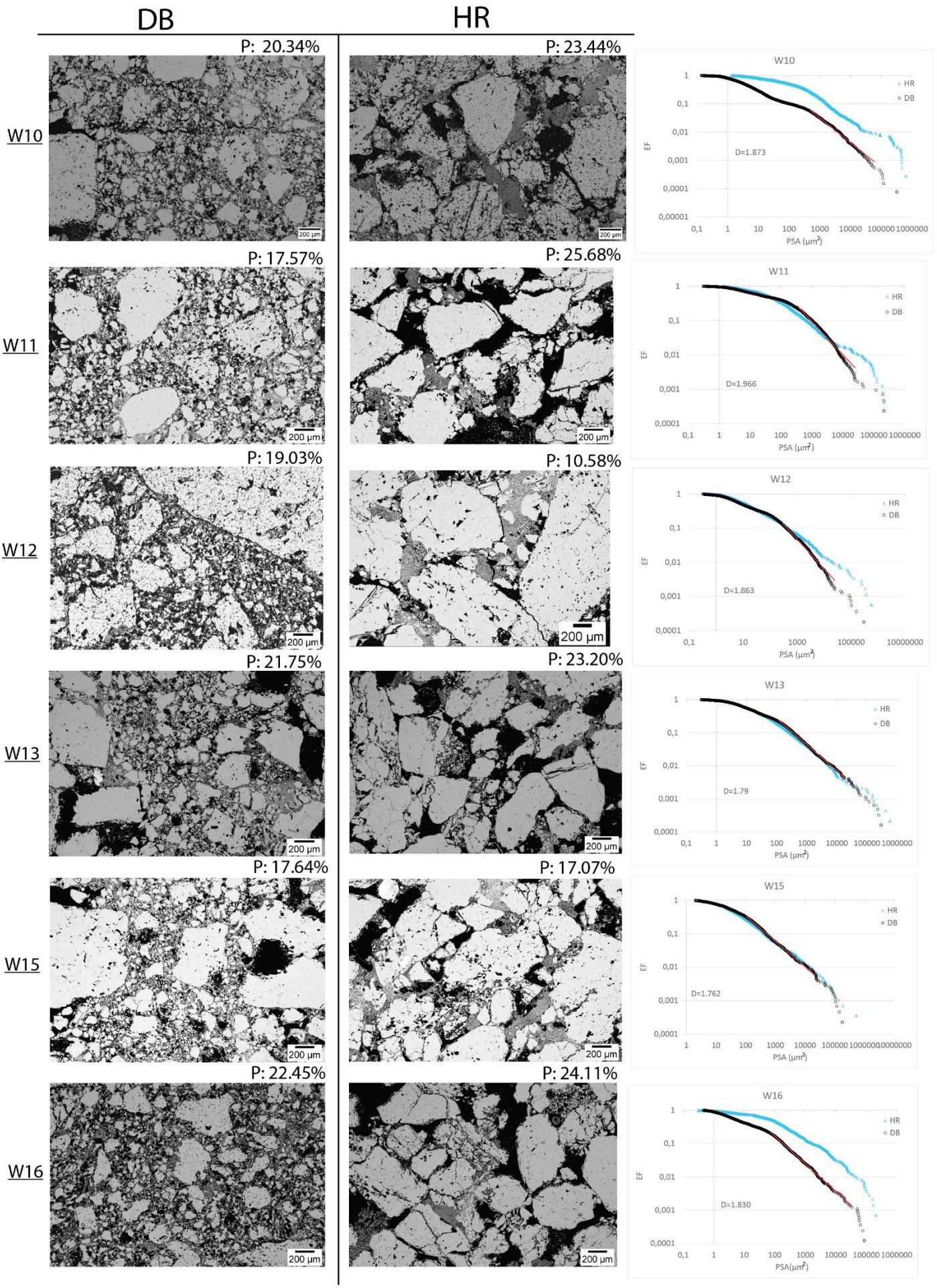

Figure 5.14: BSE images from host rock and deformation band in samples from DB1, as well as their particle size distribution plots. Porosity measurements are located on top of images. Note the large variation in porosity in both deformation band and host rock.

SEM images in Figure 5.14 and porosity analysis in Figure 5.16 show an overall decrease in porosity in the deformation band. There is a large variation of porosity between the samples, ranging from 12-35% inside the deformation band. Particularly the host rock shows a large porosity variation. Figure 5.14 shows sample W11, W13 and W16 with a visibly higher amount of pore space compared to W12 and W15. Low porosity in host rock is usually correlated with high amounts of phyllosilicates filling the pore space as seen in W12 and W15 (Fig. 5.14). Presence of kaolinite cement is more common in sample set 2 than in sample set 1 and is mainly observed in the host rock of all samples (Fig. 5.17a). Kaolinite booklets and muscovite is present in both the host rock and inside the deformation band with similar texture and behaviour as described in sample set 1. There are higher amounts of phyllosilicates in the host rock than inside the deformation bands (Fig. 5.17b). Sample W12 and W18 show higher porosity within the band than the deformation band. This could be because of the presence of coal in the band that tend to increase the porosity and will be further discussed in the next section. There is little correlation between the porosity measurements, the degree of cataclasis and the thickness of the band.

Figure 5.15: D-values of samples from DB1 measured from particle size distribution plots against their location along the deformation band. The highest D-values are located towards the centre of the band.

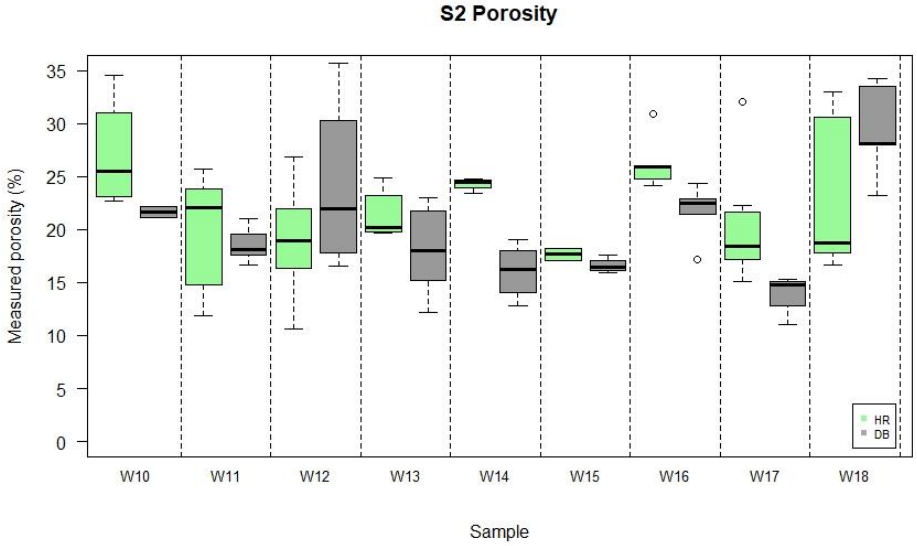

Figure 5.16: Box plot of measured porosity from BSE images of both host rock and deformation band of sample set 2. The boxes represent interval measurements from the 2nd to 3rd quantile, with the mean porosity being represented by the black horizontal line. The dashed line represents the maximum and minimum measured values.

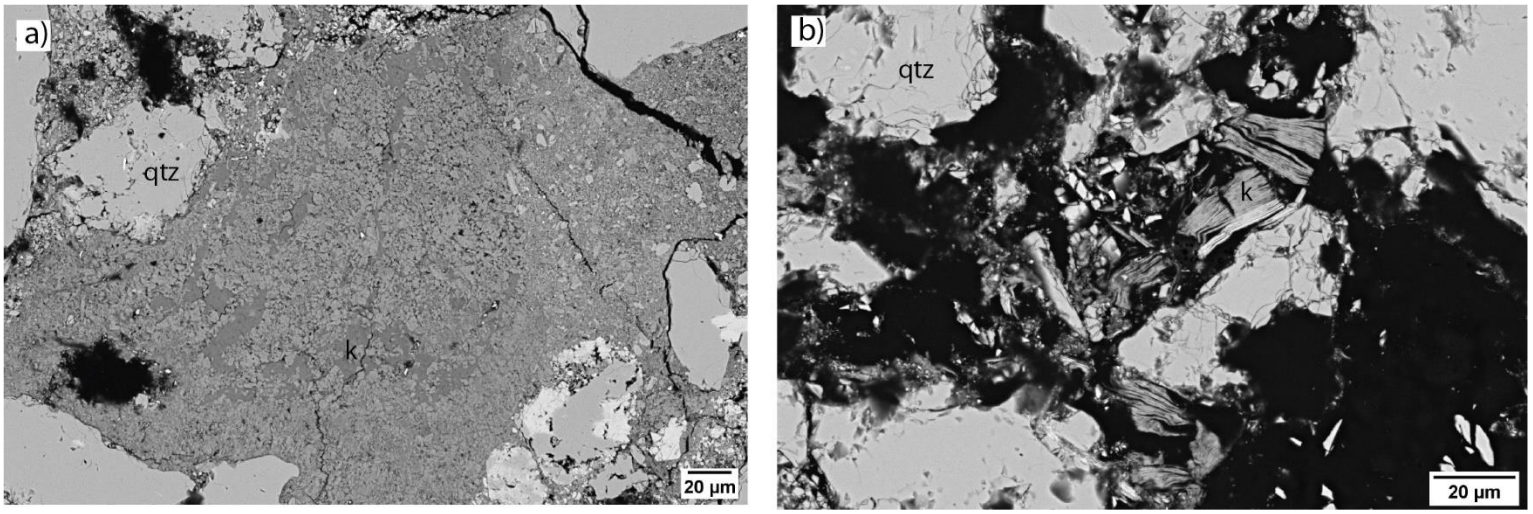

Figure 5.17: a) BSE-SEM image of kaolinite (k) cement in host rock of sample W12. b) BSE-SEM image of kaolinite booklets inside the deformation band in sample W12.

5.4 Coal

Coal is present and deformed in both sample sets, but to a various extent. Coal mainly occurs as small fragments (0.2-0.5 mm) in sample set 1, apart from sample W5 that contains a continuous layer of coal that has been sheared and rotated by the deformation bands. The coal in W5 can be used as kinematic indicators for the shear sense and shows a sinistral shear sense (Fig. 5.16). Coal in sample set 2 occur as 0.8-1.2 mm thick and continuous layers with the length ranging between 0.2-1.7 m. The coal layers have been displaced by 11-20 mm by the deformation bands. Observations from the optical microscope reveal that the coal is thicker outside the deformation band and is sheared and thinned inside the deformation band (Fig. 5.17a). Macroscopically it appears to bend in a ductile manner inside the deformation band, but SEM images show brittle fracturing of the coal inside the band (Fig. 5.17b).

Figure 5.16: Hand sample of sample W5. Coal is sheared and rotated by deformation bands.

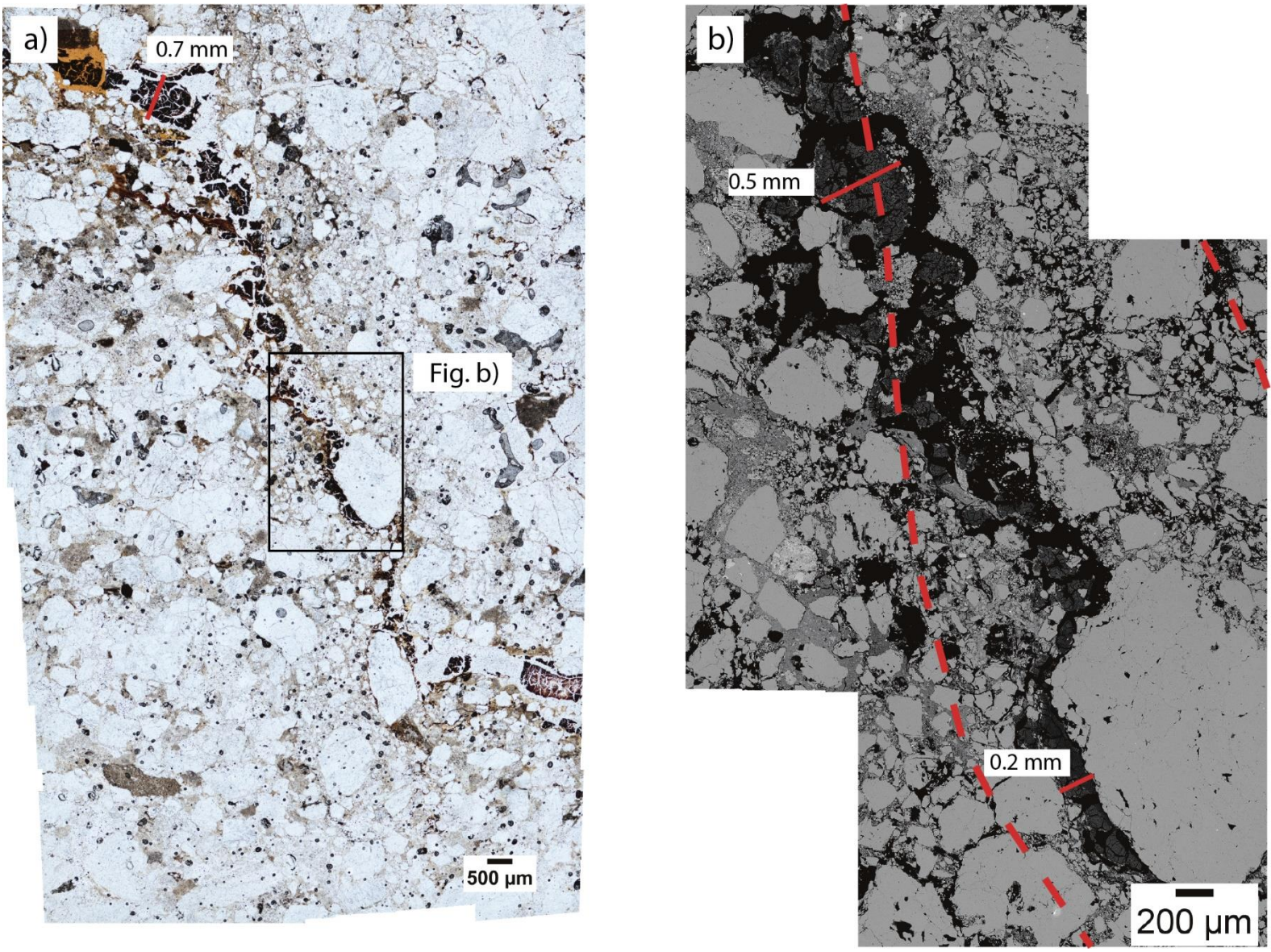

Figure 5.17: a) Photomicrograph of coal in sample W10. The thickness of the coal outside the band is 0.7 mm and it is thinned and stretched by the deformation band. b) BSE-SEM image from W10 showing the coal being thinned and fragmented inside the deformation band. The deformation band is indicated by dashed red lined and thicknesses measured are shown by full red line.

Coal in the BSE images appear as dark grey to black features in both host rock and deformation band. Its structure is highly variable, but the most common appearance of coal is as broken off fragments with a complex fracture network (Fig. 5.18a). This type of coal is referred to as fractured coal in this thesis and is the main type of coal seen in sample W10, W11, W12 and W14. The coal is equally as internally fractured in the host rock (Fig. 5.18b) as in the deformation band (Fig. 5.18c), which indicates that the fracture network is not a direct result of deformation in the deformation band. However, fragments of coal are larger (up to 1 mm in size) and more coherent in the host rock (Fig. 5.18b) and becomes more broken up smaller

grains (up to 0.3 mm in size) inside the deformation band (Fig 5.18c). Several samples contain coal that does not have the typical appearance of the fractured coal. Figure 5.19 shows the large variation of coal structure seen in both sample sets and they can mainly be divided into three types of structures based on their appearance. The first type of coal has a blobby appearance that lacks the interconnected fracture network previously described (Fig. 5.19a-b). At very high magnification (1.70K x) the blobby appearance is revealed to be highly broken up fragments of coal, showing brittle deformation. However, within the broken-up fragments there are areas with more preserved structures that show a more ductile deformation trend (Fig. 5.19b). The second type is coal with a preserved cell wall structure of its original plant material (Fig. 5.19e-g). The cell walls are often stretched, forming large open cavities (Fig. 19f) or they have been crushed and lost its initial structure (Fig 19e and g). The third type is coal consisting of crushed and broken fragments, with no fracture network or cavity porosity (Fig. 5.19h). There is no correlation between intensity of cataclasis and type of coal. Several samples contain several types of coal within very short distance as seen in Figure 5.19d. In this figure there are three different types of coal deformation present. The common fractured coal is seen to the right, coal deformed in a more ductile manner in the centre and the blobby type of coal with a poor fracture network to the left of the image.

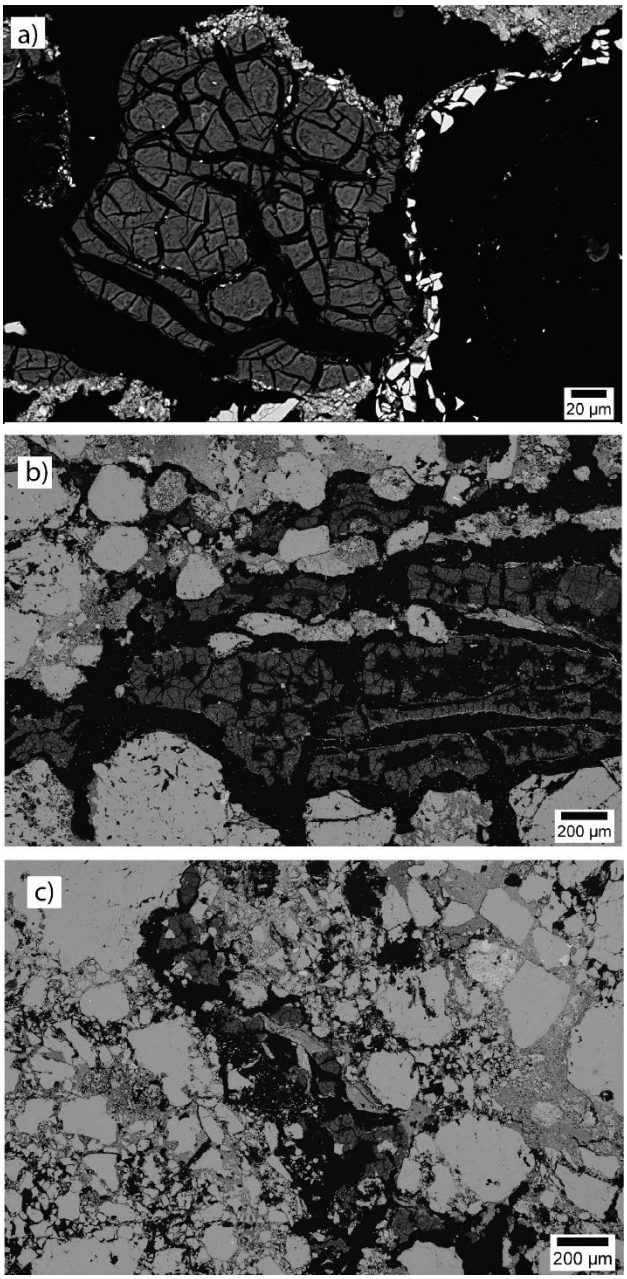

Figure 5.18: a) Fractured coal in sample W11. b) Fractured coal in host rock of sample W10. c) Fractured coal in deformation band of sample W10.

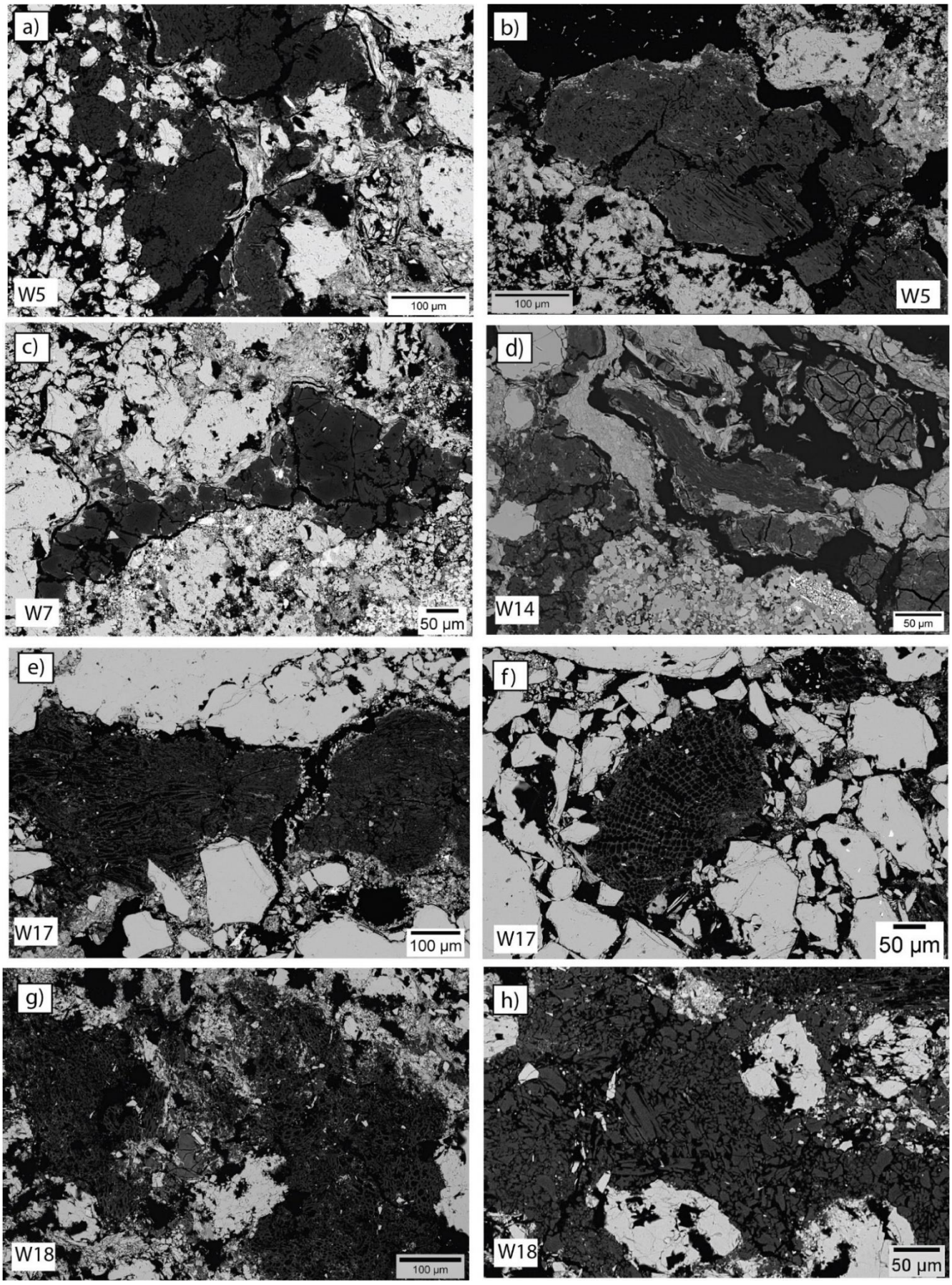

Figure 5.19: BSE-SEM images from inside the deformation bands at various samples from both sample sets. a-b) blobby coal from sample W5. c) blocky coal from sample W7. d) three different types of coal in sample W14. e-f) preserved cell wall structured coal in sample W17. g) cell wall structured coal in sample W18 that has been crushed. h) blocky coal deformed in a brittle manner in sample W18.

The porosity in the deformation band is affected by the presence of coal, depending on the type of coal. Image analysis from BSE images of fractured coal in sample W10, W12 and W14 reveal a significant increase in porosity in the deformation band where coal is present (Fig. 5.20a-b). This is largely due to the systematic increase of pore space area surrounding the coal and the fracture porosity. Porosity measurements are increased by up to 14 % when coal is present in sample W10. The high connectivity seen in the fracture network could potentially increase the permeability in deformation bands with this type of coal present. The types of coal that are not the fractured coal does not show a significant increase of pore space surrounding the coal and are mainly outlined by a thin zone of increased pore space (Fig. 5.20c-d). This results in the other types to not have such a significant effect on the porosity inside the band. Coal with preserved cell walls tend to show higher intragranular porosity, as the open cavities are not infilled by other minerals. Cases where the cell wall structure is crushed and the coal consists of severely broken up fragments results in a significant porosity reduction compared to coal with fracture networks and well preserved cell wall structures.

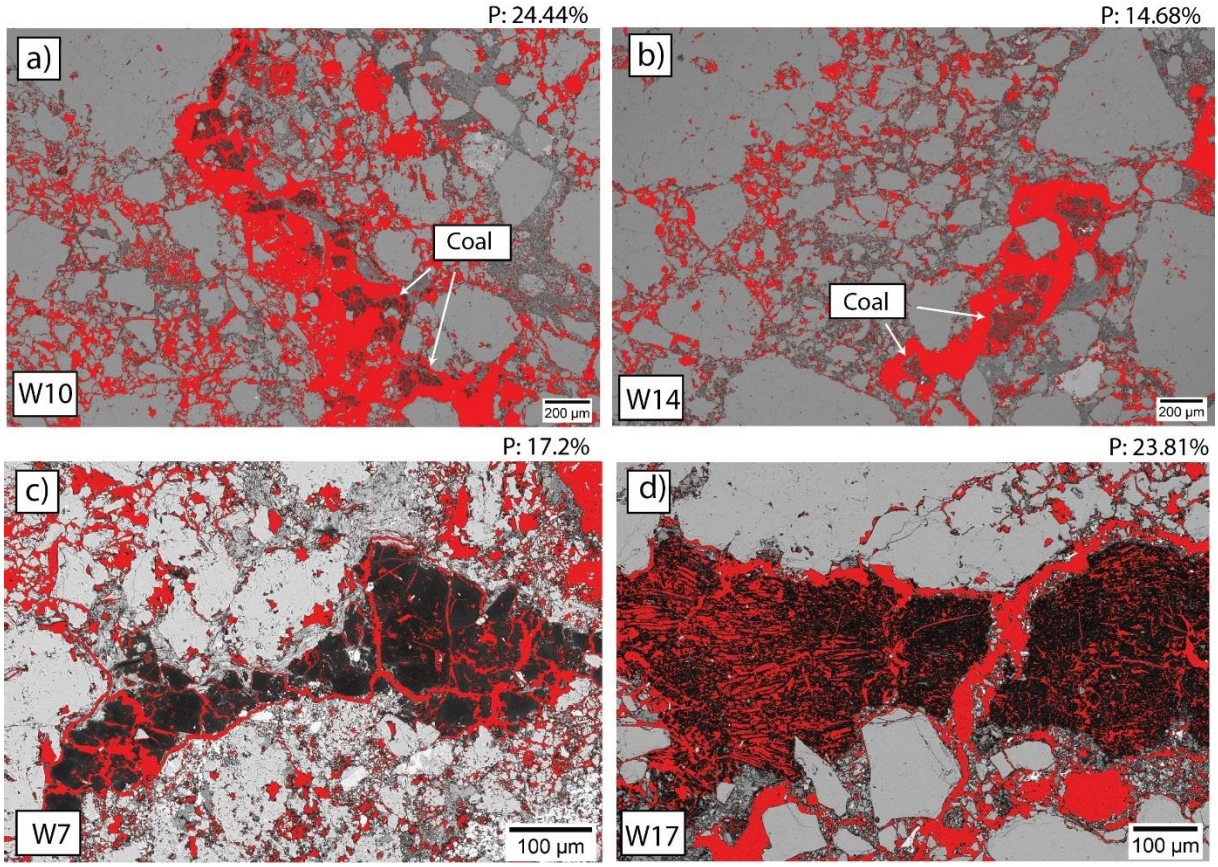

Figure 5.20: Porosity measurements of different types of coal from BSE-SEM images. Red color is pore space. a-b) Increased pore space surrounding fractured coal in sample W10 and W14. c) Less significant increase of pore space surrounding blocky coal in sample W7. d) pore space surrounding beehive coal.

6 Discussion

6.1 Particle size analysis: insights into deformation mechanisms and -conditions

Deformation in granular and porous material can occur as particulate flow or cataclasis. Particulate flow involves grain rolling and frictional sliding along grain boundaries and is typically found to be operating at shallower depths than cataclasis (Rawling and Goodwin, 2003; Fossen et al., 2007). Deformation bands where particulate flow is the dominant deformation mechanism typically display shear offsets with grains being fractured by grain flaking and intragranular fractures. Grain flaking is commonly formed during grain-to-grain contact when the grains are sliding or rolling past each other, resulting in chipping of the grain edges. Cataclasis occurs when the frictional sliding along grain boundaries is coupled with intense fracturing and crushing of grains (Fossen, 2010). Cataclasis in deformation bands results in grain size reduction, angular grains, loss of pore space and extensive grain interlocking (Aydin, 1978; Fossen et al., 2007). Grains are heavily fractured during cataclasis, with intergranular fractures being common. The main observations from BSE-SEM images of both sets of deformation bands is a clear grain size reduction inside the bands compared to the host rock (Fig. 5.5) However, whereas in sample set 1 there is an increased porosity within the deformation bands, sample set 2 shows a decreased porosity inside the bands. Grain size reduction by crushing is a common observation inside deformation bands and have previously been reported as evidence for cataclastic shear bands (e.g., Aydin, 1978; Aydin and Johnson, 1978; Antonellini et al., 1993; Hesthammer and Fossen, 2001; Torabi et al., 2007; Fossen et al., 2007). However, intense crushing of grains is not observed in sample set 1, and the particle size distribution curves do not show a large variation between the host rock and deformation bands. The measured D-values are also relatively low, (i.e., 1.78-1.87 for sample set 1 and 1.86-1.96 for sample set 2, see Figs. 5.6 and 5.14) if compared to similar studies where D-values inside cataclastic bands and fault gouges in unconsolidated rocks ranges between 2-3.1 (Sammis et al., 1987; Billi and Stortzi, 2004; Rawling and Goodwin, 2002). Sammis et al. (1987) proposed a constrained comminution model to explain grain size distribution evolution during gouge development. They suggested that fracturing is most likely to occur when two particles of equal size are in contact, and one will deform by intergranular fracturing. The fractured grain will break into sub particles and ultimately this results in a microstructure in which a large survivor

grain is surrounded by comminution debris. The process ultimately yields a self-similar grain size distribution within gouge with a D-value of ~2.6, and this value is sometimes referred to as steady state particle distribution (Sammis et al., 1987; Torabi et al., 2007). This implies that in a self-similar fault gouge no neighbouring grains have equal size and that intergranular fractures are common. What is observed in both sample sets for this study is: (1) a high number of relict grains which are commonly in contact; (2) the main fracture mechanism is typically grain flaking and intragranular fractures, with a rare occurrence of intergranular fractures; (3) D-values are low and do not reach the constrained comminution model value of ~2.6. Marone and Scholz (1989) investigated comminution mechanisms and microstructure development in fault gouges by performing shear experiments on quartz sandstone at different confining pressures. Experiments conducted at 20 MPa showed fewer transgranular fractures in particles and more flaking of grains than in experiments conducted at 100 MPa. These observations suggest that lower confining pressure promotes grain flaking rather than intergranular fracturing. These findings were supported also by ring shear experiments performed on sandstones by Torabi et al (2007), where they observed that steady state particle distribution was not achieved under normal stress of 20 MPa. The maximum depth of burial at Wangaloa is not known but is not believed to have reached depths greater than 0.5-1 km (Harrington, 1958). The equation for lithostatic stress ($P = \rho g z$) can then be used to calculate the approximate confining pressure during burial of the Taratu Formation, where ρ = density (2.3 g/cm^3 for porous sandstone), g = gravitational acceleration and z = depth. The calculation implies that the Taratu Formation was subjected to confining pressures between 12-20 MPa, which may not have been sufficient to fracture the largest grains and the steady state particle size distribution was not reached. These findings suggest that the low confining pressure have resulted in less intense cataclasis than initially believed. Grain size reduction inside the deformation bands is seen in both sample sets, although its intensity is minor when compared in the PSD plots (Figs 5.6 and 5.14). The deformation mechanism of both sample sets is therefore suggested to be an interplay between particulate flow and cataclasis, where grain size reduction is mainly a result of grain flaking from particulate flow rather than crushing from cataclasis. The transition between particulate flow and cataclasis is gradual and they can operate simultaneously (Borradaile, 1981; Bense et al., 2003). Smaller grains can break under given pressure conditions while the larger grains are strong enough to continue to slide along each other through particulate flow (Bense et al., 2003). Sample set 2 shows an overall higher D-value, and more significant grain size reduction in the deformation band compared to the host rock than sample set 1. This indicates that there is a slightly higher contribution of cataclasis in

sample set 2, particularly in sample W10, W11 and W12. These samples show displacements ranging from 11-12.6 mm and D-values from 1.86-1.96 while sample W13 and W15 show no visible displacement and have low D-values of 1.76 and 1.79 respectively. The largest displacement is located close to what is assumed to be the centre of the band moving along dip as the full extent of the band is not visible. Fossen and Hesthammer (1997) reported similar findings of peak displacement towards the centre of the length of deformation bands formed withing Jurassic sandstones in Utah (USA). The displacement distribution in faults also tend to show maximum displacement in the central part of the fault which then gradually decrease towards the tips (Fossen et al., 2010). Based on the findings discussed above it is therefore suggested that the deformation mechanisms of both sample sets are an interplay of particulate flow and cataclasis, with cataclasis being slightly more prominent in sample set 2 than in sample set 1.

6.2 Porosity distribution: kinematics vs allogenic or authigenic clay

In the previous section, it was shown how both cataclasis and particulate flow were active within deformation bands during their formation and evolution. A common characteristic of cataclastic deformation bands is the reduction of porosity within the band due to grain size reduction (e.g., Aydin, 1978; Aydin and Johnson, 1978; Antonellini et al., 1994; Hesthammer and Fossen, 2001; Torabi et al., 2007; Fossen et al., 2007). Conversely, increased porosity is usually seen in dilational bands, where studies have reported an increase in porosity of around 7-10 % in the deformation band (Du Bernard et al., 2002a; Antonellini et al., 1994). Several studies have proposed that the formation of deformation bands starts with an initial stage of dilation and minor shear associated with cataclasis (e.g., Antonellini et al., 1994; Baud et al., 2000; Besuelle, 2001; Vajdova et al., 2004; Lommatzsch et al., 2015). A study done by Lommatzsch et al. (2015) proposed that the initial stage of dilation had been preserved by subsequent fluid infiltration, resulting in the deformation band having a higher porosity than the host rock. Lab experiments conducted by Bied et al. (2002) showed that samples tested under 7 MPa of confining pressure had a porosity increase in the deformation band. The porosity inside the band were up to 31 % while the host rock had porosity of up to 21 %. Grain cracking was mainly observed, with smaller particles being formed from flaking of grain boundaries. Grain size distribution curves of the band from the samples subjected to low confining pressure were similar to the curve of the host rock, but with a larger fraction of smaller particles. Bied et al. (2002) classified their deformation bands as dilating shear bands, with the shear zone being characterized by grain fracturing. The deformation bands at Wangaloa have a

clear shear component during deformation, highlighted by the displacement of coal layers (Fig. 5.11 and 5.17), as well as an increase in porosity within the band (as observed in sample set 1, Fig. 5.5 and 5.7). Similarly to what is reported by Bied et al. (2002), the particle size distribution curves of the deformation bands in sample set 1 are almost superimposed to the host rock one (Fig. 5.6) and grain flaking is common (Fig. 5.10b). This points towards classifying the deformation bands in sample set 1 as dilational shear bands.

An increase of porosity in the deformation bands in sample set 1 could also be explained by the preferential precipitation of authigenic clay in the host rock. The host rock contains large zones of clay that fill in the pore space. Clay is found at smaller amounts in the deformation band compared with the host rock, and with smaller particle size. Some BSE-SEM images show up to 40 % clay, which are found to greatly reduce the porosity. Wilson and Pittman (1977) reported authigenic and allogenic clay in sandstones and how they can be distinguished from each other. The term allogenic clay refers to clay particles that are formed prior to deposition while authigenic clay refer to the growth of new minerals by the alteration of other after their deposition (Wilson and Pittman, 1977). High amounts of authigenic clay can reduce the porosity significantly and lower the reservoir quality (Sarkisyan, 1972; Howard, 1992; Hong et al., 2020). Authigenic clay can form either as a direct precipitate from solution (neoformation) or through reaction between precursor material and the contained waters (regeneration) (Sarkisyan, 1972; Wilson and Pittman, 1977). Numerous criteria have been proposed for differentiation of authigenic clay and allogenic clay. The former typically attain a higher degree of purity in their chemical composition whereas the latter may experience degradation during erosion and transport. The most reliable and commonly used criterion for distinguishing the two types of clays is often a well-developed crystalline habit for the case of authigenic clays (Wilson and Pittman, 1977; Wanas and Soliman, 2001). Kaolinite is the main clay mineral found in both sample sets and occurs both as cement and as stacks referred to as kaolinite booklets (Fig 5.10a). Kaolinite booklets are delicate fabrics and has previously been suggested as an indication of authigenic origin as it is unlikely that the booklets would survive sediment transport (Arostegui et al., 2001; Wanas and Soliman, 2001; Gianetta et al., 2021). Authigenic kaolinite in sandstones can be produced by the migration of meteoric water in pore space during diagenesis. Porewater supersaturated with silicon and aluminium ions can lead to the precipitation of pore filling kaolinite cement (Hurst and Irwin, 1992; Psyrillos et al., 199; Ahmed, 2008). Kaolinite cement in both sample sets is found mainly in the host rock, suggesting a preferential flux of fluids in the host rock. However, kaolinite booklets are also

found inside the deformation bands at smaller amounts, which suggests that fluid was not restricted by the deformation bands. Maciel et al. (2018) reported similar findings of increased clay content in the host rock, suggesting a barrier behaviour of the deformation bands. Based on their observations, the authors suggested an authigenic origin for the clay, seeing as if it was allogenic, the clay would have been incorporated into the fault zones during deformation. At Wangaloa, the pore space in the deformation bands is high in both sample sets and therefore it is unlikely that the bands acted as a barrier for fluid flow. Evidence such as kaolinite booklets and increased clay cement in host rock points towards the clay being authigenic, thus indicating that the measured porosity in the host rock is secondary porosity. New porosity measurements done in ImageJ, where the clay is classified as pore space, results in a host rock porosity of roughly 30-35 % in sample set 1 and 33-40 % in sample set 2 (Fig 6.1). Measuring porosity without clay is more difficult to do inside deformation bands as both grain size and clay minerals as smaller, but an increase in porosity is expected to be found inside the deformation bands as well. These new measurements could suggest that the porosity inside the deformation band of sample set 1 initially was not higher than the host rock, but that preferential precipitation of clays in the host rock resulted in a decreased porosity in the host rock, thus making the porosity in the deformation bands appear higher. This could imply that the cluster may not be classified as dilational shear bands, if the initial porosity of the band is lower than the host rock once the clay is removed. In general, further work might be needed to shed more light on the timing and relationship to the authigenic clay with deformation in order to more precisely classify the bands. More work is also needed on why there is a preferential precipitation of clays in the host rock considering the deformation bands do not appear to act as a barrier for fluid flow.

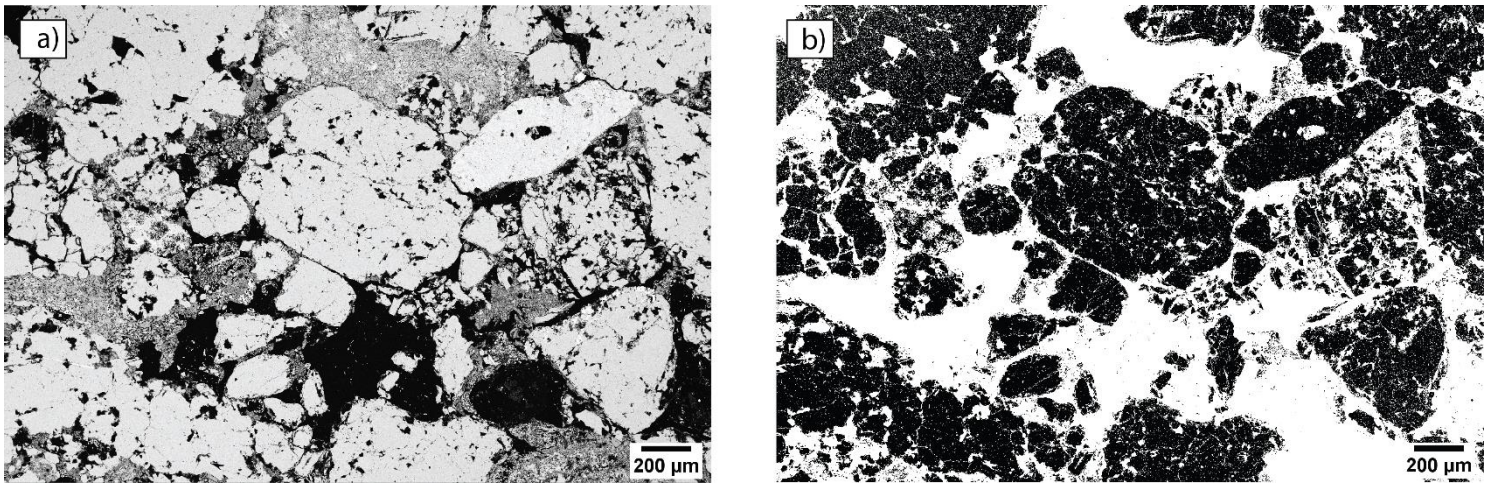

Figure 6.1: a) BSE-SEM image from host rock in sample W12 that contains pore filling clay. b) binary image from ImageJ that has been used to remeasure the porosity after clay as been digitally removed and classified as pore space (white color).

6.3 The relationship between strain evolution, PSD and porosity

One of the main aims of this thesis was to investigate whether there was a connection between the evolution of strain and the microstructures in the deformation bands such as porosity and particle size distribution. The results showed that there was a large variation in porosity measurements, but not a large variation in particle size distribution between the bands and the host rock. This section will discuss if the variations were due to different increments of strain or other factors. The deformation band style can vary depending on the lithology of the host rock, which again could contribute to the large variation in porosity measurements as seen in the samples. Factors such as initial sorting, angularity, grain size and porosity of the host rock have been proved to influence the deformation mechanism (Aydin, 1978; Flodin et al., 2003; Torabi and Fossen, 2009; Fossen et al., 2007). A study done by Torabi and Fossen (2009) on deformation bands in the Entrada Sandstone, Utah (USA), revealed that the degree of cataclasis, porosity and permeability is intimately related to the initial microstructure of the host rock layers. Sammis et al. (1987) suggested that in a fault rock with fractal PSD the total strain is correlated with the D-value. This approach is based on the constrained comminution theory, where average particle size decreases with increasing strain (Sammis et al., 1987; Hadizadeh and Johnson, 2003). However, in our case, there is no clear correlation between the D-values, microstructures, and strain evolution. The calculated bulk strain in sample set 1 shows $\gamma=3$ at the thinnest part of the cluster and $\gamma=0.4$ at the thickest part (Table 5.1). For the same displacements, a thicker deformation band means that the strain is distributed over a larger volume, and therefore the expected degree of cataclasis is lower in the thinner band. However, this is not seen in sample set 1. The calculated D-value of W1, which is collected where the band is 4-12 mm thick (Fig. 5.3), is 1.785, while the D-value of W7, collected where the band is 60 mm thick, is 1.871. These findings seem to suggest that the D-value is lower at a location with higher strain than at a location of lower amounts of strain. It is worth noticing though, that sample W1 is located close to a smeared mud layer, which could explain the higher frequency of small particles (i.e., the clays), thus resulting in a higher D-value. Furthermore, the high amounts of clay in W1 can promote frictional grain boundary sliding by acting as a lubricant (Fossen et al., 2007), thus inhibiting a high intensity of fracturing inside the band. However, the D-values of sample W2 and W3 are still lower than the D-values of sample W7, confirming that the D-values are lower at locations with higher strains.

Overall, the relatively similar D-values and the large variation of porosity in the samples do not appear to be correlated with the bulk strain and degree of cataclasis/fracturing. Instead, host

rock microstructural characteristics such as initial grain size, sorting, angularity, porosity, content of clay and cement appear to have a larger impact on the final degree of cataclasis. The upper part of the Taratu Formation where the samples are collected show a spatial variation in grain size distribution by alternating layers of coarse and medium sand. This is shown in the variation of PSD plots for the host rocks (Fig. 5.6 and 5.14).

6.4 Formation of the deformation bands

This section will discuss the formation of the deformation bands, with particular focus the following questions:

6.4.1 How does the deformation bands relate to the structural evolution of the region?

6.4.2 What are the mechanisms behind development of the deformation bands?

The main focus will be on the deformation band cluster in sample set 1 due to its unusual increase of porosity inside the band.

6.4.1 *How does the bands relate to the structural evolution of the Otago region?*

The structural geology of coastal Otago and Wangaloa Beach records the transition from extensional tectonic regime to compressional tectonic regime (Bishop and Turnbull, 1996; King, 2000; Forsyth, 2001). Several major NE-SW and NW-SE trending faults in the region developed as normal faults during extension in the Cretaceous, and then underwent inversion during the compressional stress field in the late Miocene (Bishop and Turnbull, 1996; Litchfield, 2001). A good example of reactivation in a compressional tectonic regime is seen in the Waihemo Fault, Castle Hill Fault and Titri Fault (Litchfield, 2001). The compressional regime resulted in folding and faulting throughout the region and is still continuing to this day (Bishop and Turnbull, 1996; Litchfield and Norris, 2000). Although no extensive mapping of faults was done for the purpose of this thesis, previous studies mention several small-scale faults and folds in the area surrounding Wagnaloa Beach with both reverse and normal sense of slip (Harrington, 1958; Barry, 1985; Bishop and Turnbull, 1996; Litchfield and Norris, 2000). The deformation bands at Wangaloa Beach formed likely as a response to the tectonic stresses of these faults. A thesis on this area done by Matthews (2003) described several zones of normal faulting at Wangaloa with no evidence of reverse faulting. Similarly, the small-scale structures mapped for this thesis, such as the deformation bands and the slip surface in sample set 1, all show a normal sense of motion. This can be explained through a selective reverse-reactivation of faults. Kelly et al. (1999) investigated the importance of fault geometries on the reactivation

with a reverse slip direction of normal faults. Their study concluded that mostly larger faults with displacement > 22 m and dip ranging of 40-55 ° showed reactivation in compression, while reverse-reactivation was rarely achieved on normal faults with a dip steeper than 60° (Kelly et al., 1999). The faults mapped for this thesis have a dip range of 60-70° and maximum displacement of 30 cm suggesting that their lack of reactivation during the switch to a compressional tectonic regime was controlled by their geometry and overall displacement.

6.4.2 What are the mechanisms behind the development of the deformation bands?

Based on the tectonic history of the studied area, it is proposed that the development of the deformation bands is associated with fault growth in the area. ‘

The deformation bands in sample set 2 are characterized by a localized, single, through-going deformation band that is not spatially located adjacent to a fault or within a fault-related damage zone. Previous studies have shown that in compressional regime deformation bands appear to be more broadly distributed away from faults (Braathen et al., 2020 and references therein). Deformation bands in sample set 2 are suggested to have gone through a three-stage development. During sediment deposition and burial, only little deformation occurred mainly as grain rearrangement (stage 1). As burial continues, the confining pressure increases, ultimately leading to the initiation of deformation band formation by particulate flow (stage 2). A poorly lithified host rock with high porosity allows for grain reorganization, and possibly an initial porosity increase within the band (Bied et al., 2002; Lommatzsch et al., 2015). Further burial results in pore collapse in the incipient deformation bands and fracturing at grain contacts and along grain edges becomes more widespread (stage 3). Meteoric waters circulating through the pores during diagenesis resulted in the precipitation of authigenic clay. The exact timing of this last event is not known and is noted as focus for future work.

The development of deformation band clusters has been an open topic of discussion since first described by Aydin (1987). The same sequential evolution that formed the single bands can be applied to the cluster. However, some explanation is needed to understand why the network evolves in a cluster. There are two models proposed for the formation of a deformation band cluster that can be used to explain the formation of what is observed in sample set 1. The first possibility is the strain hardening model which was first proposed by Aydin (1978). Here, cataclasis leads to grain fracturing and comminution, which increases the grain-contact friction and results in a strain hardening behavior of the deformation band (Aydin and Johnson, 1978; Nicols et al., 2013; Philit et al., 2018). This means that as strain is accommodated within the

deformation band, the (shear) stress necessary to continue localizing the deformation in the band increases as well. As a result, there will be a point where it is energetically more favorable to form a new deformation band, rather than sliding on the one already present. When this process is repeated multiple times, the resulting band network will be a cluster (Aydin and Johnson, 1978; Fossen and Hesthammer, 1997; Mair et al., 2000; Fossen et al., 2007; Nicols et al., 2013). Eventually, the number of bands increases until an ultra-fine cataclasite is formed which promotes strain softening and slip localization on a single through-going slip surface (Aydin and Johnson, 1978; Fossen et al., 2007). The second possibility is referred to as the geometric model (Nicols et al., 2013). Here, deformation bands are characterized by a strain-weakening behavior and that occurrence of types of fault-related complexities such as fault relay zones, fault bends, fault intersection and normal drag can promote the formation of clustered bands. The cluster is envisaged by Nicols et al. (2013) to develop in three steps. (1) A fault forms as an array of irregular segments separated by relays, bends or fault intersections. (2) Strain accumulates across the fault zone and deformation bands are formed as shear strain migrates towards an optimal energy efficient planar geometry. (3) The deformation bands attain a geometry that enable the irregularity to be by-passed and strain localization form a slip surface (Nicols et al., 2013) (Fig. 6.2) Additions of new deformation bands followed by slip localization is central to both models, but the processes are different. The slip surface in the strain hardening model is proposed to form when ultra-fine cataclasis leads to strain weakening. However, there is no evidence in sample set 1 for ultra-fine cataclasis or strain hardening. In fact, there is relatively low amount of cataclasis and an increase in pore space found in the deformation bands. These findings do not support the theory of strain hardening, as one would expect to see pore space collapse and grain interlocking in each band (Mair et al., 2000). The confining pressure during formation of the bands of Wangaloa were relatively low (12-20MPa) and estimated calculations only showed a bulk strain of 3. It is therefore highly unlikely that the strain was high enough to promote ultra-fine cataclasis and strain hardening in sample set 1. The geometric model therefore seems to better fit the observations for sample set 1. The slip surface located in the cluster does show a bend and it is possible that the cluster formed as two faults linked up (Fig. 5.3). The damage zone that is found adjacent to this bend tips out slightly above it and does not extent further along the slip surface. Figure 6.2 shows a proposed sequential formation of the cluster of deformation bands in sample set 1 where stage 1 involves increasing confining pressure that results in strain accumulating and forming possibly two separate faults separated by relays. As strain accumulates, deformation bands are formed at incremental steps in order to enable the separate faults to link up (stage 2). Once the

energetically efficient planar geometry is reached and the deformation bands attain a geometry that enables the irregularity to be by-passed strain localization, the formation of new bands ceases (stage 3) (Nicols et al., 2013). A question that still remains open regards the observed component of dilatancy in the deformation bands and further work on this topic is necessary. The final stage (stage 4) involves the precipitation of the authigenic clay. High porosity in both deformation band and host rock resulted in the movement of meteoric waters through pores at some point during diagenesis, which promoted the precipitation of authigenic clay in the pore space of the host rock in particular. Timing of the authigenic clay, and why there was a preferential precipitation of authigenic clay in the host rock considering the high porosity in the deformation band is not investigated but is suggested as possible direction for future work.

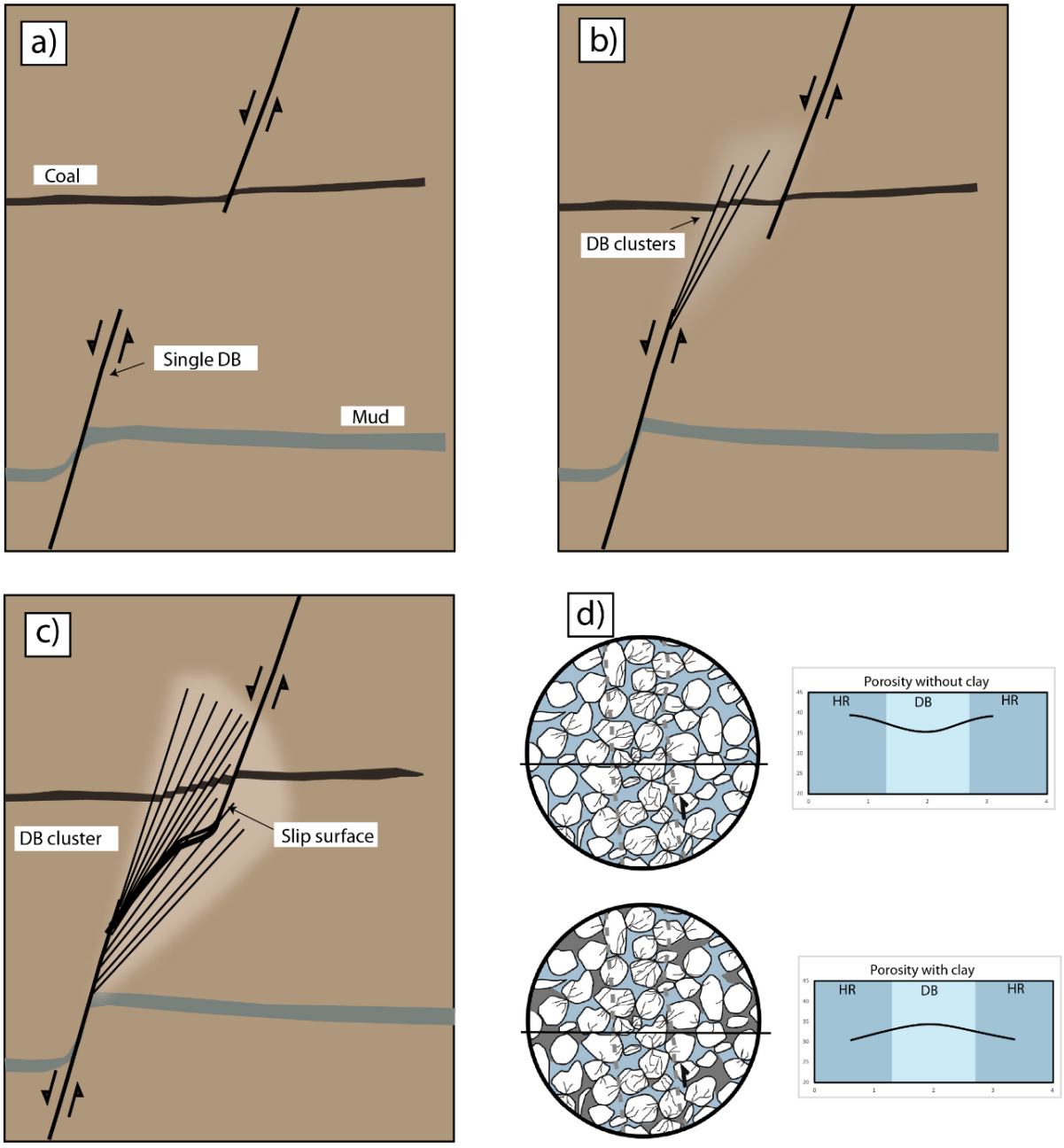

Figure 6.2: Diagram of the evolution of the deformation band cluster in sample set 1. a) stage 1, two separate faults are formed in a sandstone under increasing confining pressure. b) several deformation bands are formed at incremental steps to accommodate distributed strains and link up the two faults. c) formation of new bands ceases as a slip surface form and thus becomes energetically efficient to accommodate displacement. d) meteoric water circulating through the sandstones during diagenesis promotes clay precipitation (grey color) in the pore space. This alters the porosity within and outside the deformation bands. (Modified from Nicols et al., 2013 and Ballas et al., 2015.

6.5 Different coal types and the effect of coal on porosity and permeability

The coal displays various types of fractures and deformation mechanisms. The highly fractured coal shows a fracture network that is similar to desiccation cracks in mud. Similar fractures in coal were found in the Balingian Province, Malaysia by Ibrahim and Padmanabhan (2019). They discovered that thermally stressed samples showed an increase in fractures with temperature and suggested loss of moisture content in the coal as the mechanism behind it (Ibrahim and Padmanabhan, 2019). Loss of moisture in coal can also occur during the coalification process or due to tectonic stress and the resulting volume shrinkage (Thakur and Rajput, 2016; Rong et al., 2020). Rong et al. (2020) conducted a study where low rank coal was dried under a constant environment of 423 K and 20kPa in order to determine the relationship between dehydration, volume shrinking and thermal fragmentation. Moisture in coal is mainly found in the pore structure and as drying progresses, the water in the large pores evaporates first while water in the smallest pores evaporates last. The dehydration is considered to be carried out from the outside of the coal particle to the inside, resulting in a wet core with a decreasing radius (Fig. 6.3) (Rong et al., 2020). Water is considered to be an important support component of the mechanical strength of coal (Suuberg et al., 1993). Removal of internal water results in pore collapse and volume shrinkage which leads to development of fractures in the dry zone (Bongers et al., 2000; Rong et al., 2020; Dong et al., 2021). The fractures are usually found to be extending along a spherical surface towards the wet core (Rong et al., 2020), with stress produced by shrinkage around the fractures promoting further propagation of them. With increasing drying time, the size and number of fractures grow, and larger fractures facilitate breaking of coal particles (Fig. 6.3). Fragmentation is primarily caused by devolatilization and the increase of pressure of the volatiles in the pores of the coal particles (Zhang et al., 2002). The fractures described by Rong et al (2020) are similar to the ones seen in the highly fractured coal in the samples of this thesis (Fig. 5.18), suggesting a similar origin. Increased temperature and tectonic stresses during the burial of the Taratu Formation may have resulted in the loss of volatile matter in the coal, leading to volume shrinkage and formation of the well-developed fracture network. The volume shrinkage results in increased pore space area surrounding the coal and the fragmentation of the coal in smaller particles (Fig. 5.20). Granular flow and cataclasis within the deformation band may have shifted the grains and resulted in a less significance pore space increase surrounding the coal in the band compared to the host rock. The coal rank of the coal in the nearby Kaitangata Coal Field ranges from lignite to sub-bituminous, which is considered to be low-rank coal with high moisture content (Lomas, 2003).

Fractures in lignite have previously been reported to appear similar as desiccation cracks in mud (Dong et al., 2021), which is the same observations made in our samples.

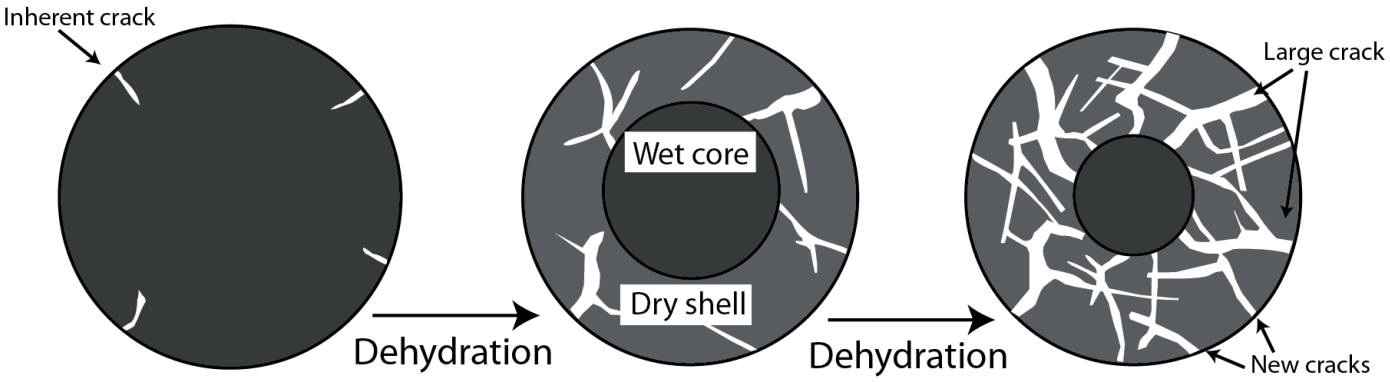

Figure 6.3: Mechanism of volume shrinkage and fracturing of a coal particle. Dehydration of coal leads to fracturing and a decreasing wet core. Number and size of fractures in increasing with increasing drying time. Modified from Rong et al., 2020.

The fractured coal is the most common coal observed in the samples, but there is a large variety in microstructures and deformation mechanism of the coal which is portrayed by Figure 5.19. Differences in coal rank and macerals play an important role in microstructural variation as macerals particularly have distinct properties based on the organic material they are derived from (Pophare, 2014; Greb et al., 2017; Vranjes et al., 2018). There is little information on structure characteristics for macerals as they are difficult to separate (Sun et al., 2002), and characterization of the distinct macerals was not done for this thesis. Fusinite and semifusinite are submacerals of the inertinite group and tend to form well-defined cell wall structures of wood tissue with cavities (Gamson et al., 1992; Pophare, 2014). The coal structure in Figure 5.19f with preserved cell walls resembles this description and is interpreted to be fusinite or semifusinite. The cell cavities are called cell lumens and are often filled in with minerals (Gamson et al., 1992). The cell lumens in our samples show no filling. It is common for the cellular wall to be broken and crushed if the coal has undergone compression. In the initial phase of compression, the wood fibres behave like an elastic cellular solid, which is termed elastic buckling. Further compression can result in the wood fibres to collapse and break, a process called plastic collapse (Fig. 6.4) (Gamson et al., 1992). The coal structure seen in Figure 5.19e and 5.19g is believed to be a result of plastic collapse of the cell wall structures of wooden tissues of a fusinite, while Figure 5.19f show the cellular walls in a less deformed state. Coal in Figure 5.19a, c and h appear to be coal fractured in a brittle manner, where its original structure has been lost. Coal in Figure 5.19b and d behaves more ductile. A study done by Vranjes et al (2018) reported that macerals have different mechanical properties, such as hardness (H) and

elastic modulus (E_r), where E_r expresses the stiffness of a material. A material with low E_r is mechanically weak and has low resistance to deformation (Fossen, 2010). The highest average values for H and E_r have been obtained from inertinites and the lowest average values were obtained from liptinites (Vranjes et al., 2018). Inertinites also have the highest aromaticity and liptinites have the lowest (Sun et al., 2002; Pickel et al., 2017). High aromaticity indicates more stability between bonds, and aromatic rings do not easily break apart. It is clear based on the mentioned findings that different macerals have different mechanical properties that results in different deformation mechanisms. This could explain the different structures seen in the coal in our samples, but further work is needed to be done on identification of macerals in order to fully confirm this theory.

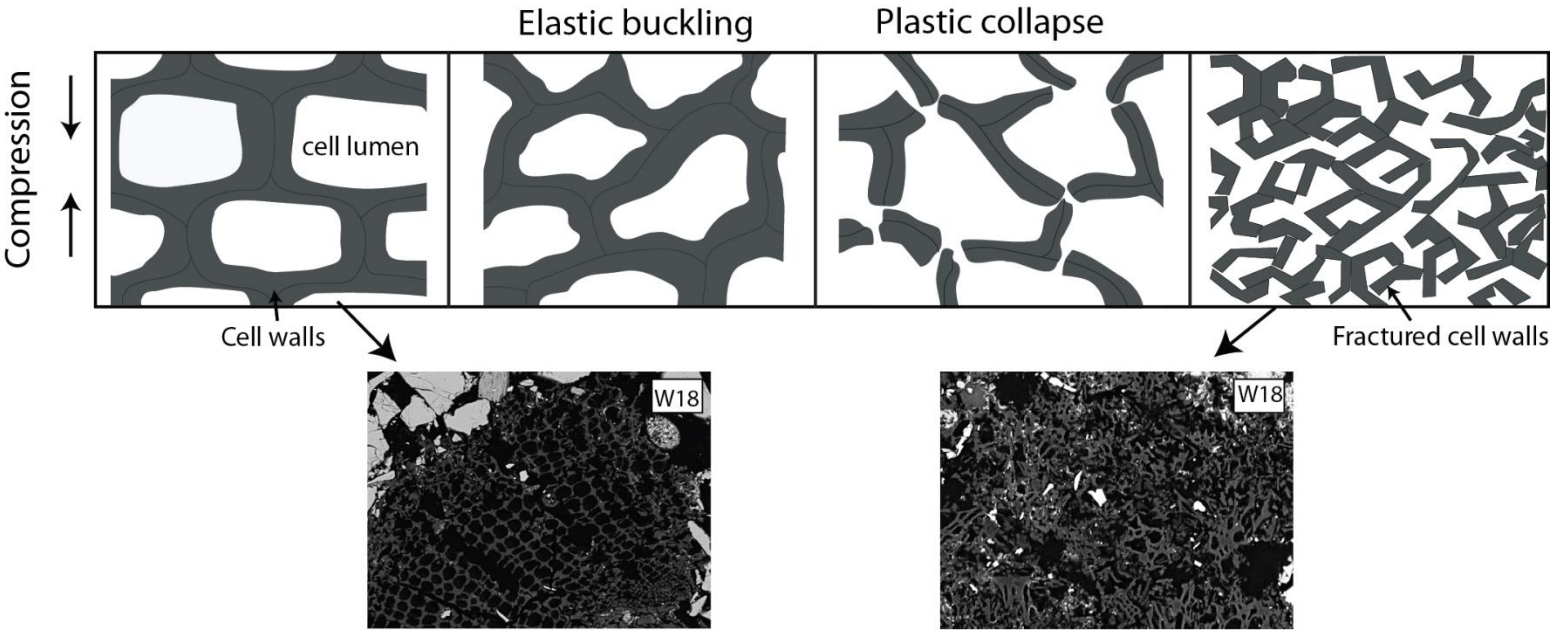

Figure 6.4: Phases of deformation observed in coal with preserved cell wall structures and cell lumens and BSE-SEM images where similar structure is observed in the samples from Wangaloa. Increased compression results in the plastic collapse of the cell walls, eventually leaving the coal heavily fractured with complete loss of initial structure. Modified from Gamson et al., 1993.

One of the main aims of this thesis was to discover if the coal affected the porosity in a similar manner as a clay smear. Clay smear is formed in deformation bands or faults if the host rock contains high enough clay content or if it goes through a mud layer (Fisher and Knipe, 2001; Fossen et al., 2007). Clay smears may impede subsurface flow as the porosity and permeability is significantly reduced (Vrolijk et al., 2016). The coal in sample set 2 behaves in a similar way as a coal smear, in the sense that it has been smeared inside the deformation band. However, the coal is fragmented into smaller particles, with each particle having an extensive microfracture network. Volume shrinkage of the coal due to drying also results in increased

pore space surrounding the coal fragments, which may increase the permeability of the deformation band. Two types of coal porosity are recognized in this thesis: fracture porosity and phyteral porosity. Fracture porosity is associated with the microfracture network seen in the main fractured coal. The microfractures have a high connectivity and are generally not filled in with any minerals. Phyteral porosity is a term used by Gamson et al. (1993) and refers to the porosity within the void space of the original plant fragments. Remnants of cell wall structures and cell lumens are found in a few samples. The cell lumens have a high pore space area for instances where they are not crushed. Deformed coal can occur either as severely broken and crushed fragments or deformed in a ductile manner (Fig. 5.19). Both show a porosity reduction, but they are of such a rare occurrence that their impact on the overall porosity and permeability is suggested to be minimal. No permeability measurements were done for the samples but based on the high fracture network connectivity it is suggested to increase the permeability in the presence of coal. Matthews (2003) conducted a similar study on coal in the Taratu Formation at Wangaloa and Shag Point, north of Dunedin. Her findings indicated that coal smears could act as a potential barrier to fluid flow. However, the coal was only studied under optical microscope and the microstructures of coal was not visible in a way that BSE-SEM images allows for. The coal in the thin sections analysed by Matthews (2003) were c. 2-3 mm while the coal in the Wangaloa samples were generally <1 mm. Færseth (2006) reported coal smears in faults from offshore Norway. The thickness of the coal seams was 0.15 and 0.35 m thick, and he proposed that coal smears may form significant barriers to fluid flow (Færseth, 2006). The thickness of the coal seams from Færseth (2006) and Matthews (2003) is thicker than the ones studied at Wangaloa, and it is suggested that the thickness of the coal seam may play an important part in determining the sealing potential of coal smears. A potentially interesting approach would be to investigate the coal smears from Færseth (2006) and Matthews (2003) under the SEM to analyse the occurrence of cleating or microfractures that would enhance fluid flow. More work is necessary to be done on coal in deformation bands. The coal in this thesis is suggested to not have a high sealing capacity. This is mainly due to of the high fracture porosity, which shows a high connectivity, and the increased pore space outlining the coal fragments. Even more study is necessary to be done on the macerals present in the coal, where it is suggested that different maceral may have various effect on porosity and permeability.

6.6 Influence on fluid flow in reservoir

Deformation bands have been shown to have the potential to act as conduits or barriers for fluid flow (e.g., Antonellini et al., 1999; Fisher and Knipe, 2001; Fossen and Bale, 2007). Decrease in porosity and permeability seems to be directly controlled by the intensity of cataclasis within the deformation bands and can baffle fluid flow (Ballas et al., 2015). High porosity loss is achieved by grain fracturing and comminution, which is typically seen in compactional shear bands (Aydin, 1978; Antonellini et al., 1993; Hesthammer and Fossen, 2001; Fossen et al., 2007). The deformation bands in sample set 2 show an overall porosity reduction, but with a large spatial variation of porosity along dip of the band. Torabi and Fossen (2009) regarded a single deformation band to have a restricted contribution to baffling of fluid flow due to its lateral variation. This applies well sample set 2, where porosity variabilities along the band (with local values up to 30%) would result in local conduit behaviour of the deformation band. Following Fossen et al. (2007), the cluster can be classified as dilational shear bands, which is considered to have limited influence on permeability in sandstone reservoirs (Fossen et al., 2007). However, to my knowledge, dilational deformation band clusters have previously not been documented, meaning that their influence on fluid flow is possibly still an open question to be investigated. The findings in this thesis show that there is large spatial variability of porosity within the cluster. This variation is mainly due to spatial differences in clay content, both in the host rock and deformation bands, and initial grain size of the host rock. Even though the presence of clay greatly reduces the porosity and permeability locally, its spatial variability means it has low influence on the overall seal properties of the cluster. On the other hand, it might increase the sinuosity and tortuosity of fluids by altering the fluid flow path and consequently decrease its effective permeability (Fossen and Bale, 2007; Sun et al., 2011; Ballas et al., 2015). Contrary to a clay smear where phyllosilicates deform in a ductile manner (Torabi and Fossen, 2009), coal smears appear to fracture in a brittle manner. As a result, locations where coal is present in the deformation bands seem to have an increase in porosity due to volume shrinkage and development of a well-connected fracture network within the coal. Finally, based on all the observations, both sample sets of deformation bands are suggested to have limited influence of fluid flow because of the low degree of cataclasis and spatial variation of porosity and clay content.

7 Conclusion

The main aim of this thesis was to investigate the changes in microstructures within the deformation bands and gain further understanding of their deformation mechanisms. Lastly it had a look at coal entrainment in the deformation bands and how it could affect the porosity. The aims were reached through field-based investigations and digital analysis of porosity, PSD and coal variations seen in BSE-SEM images from both the host rock and deformation band. From the results and discussion presented herein, the following conclusions are drawn:

- Analysis of particle size distributions inside the deformation bands reveal that the deformation mechanism is a combination of particulate flow and cataclasis. Low confining pressure during burial is suggested to explain the low degree of grain crushing in the deformation bands, which is reflected by the low D-values and similar deformation band curve and host rock curve in the PSD plots. Sample set 2 show a slightly higher degree of cataclasis than sample set 1.
- Porosity increase is observed inside the deformation band cluster of sample set 1. Following Fossen et al. (2007) the cluster is classified as dilational shear bands, which may explain the increased porosity and low degree of grain crushing. Preferential precipitation of authigenic clay in the host rock also affects the porosity, resulting in the large spatial variability of porosity measurements. This could imply that the measured porosity is secondary porosity, and that the initial porosity was not higher within the bands compared to the host rock.
- Porosity decrease is observed inside the deformation bands of sample set 2, resulting in the deformation bands being classified as compactional shear bands. Authigenic clay is found at larger amounts in the host rock, resulting in a large spatial variability of porosity in sample set 2.
- The geometric model by Nicols et al. (2013) is suggested to be a better fit for the observations from sample set 1 and is proposed as the formation model of the cluster. Geometric irregularities and the linking of two separate slip surfaces resulted in incremental formation of deformation bands in order for the slip surface to link up. Once linked up, a through-going slip surface is formed.
- Microstructural analysis reveals a large spatial variability of porosity and PSD moving along dip of the deformation bands and in the host rock. There appears to be no correlation between the bulk strain, degree of cataclasis and porosity

measurements. These variations are instead suggested to be a result of variations in microstructures such as initial grain size, angularity, initial porosity and particularly the clay content in the host rock.

- The various types of coal structures are suggested to be attributed to different coal macerals present in the samples. Macerals have different mechanical properties; hence they deform differently and could therefore be the reason to why there is such a large variation in the coal when observed in the BSE-SEM.
- Volume shrinkage of coal due to heating during burial is suggested to result in fragmentation and formation of well-connected fracture network within the coal particles both inside the deformation bands and in the host rock. Volume shrinkage results in the coal being outline by increased pore space, increased fracture porosity and possibly increased permeability. It is therefore concluded that the coal investigated in this thesis results in increased porosity and has limited sealing potential.
- The deformation bands are suggested to have limited influence of fluid flow because of the low degree of cataclasis and large spatial variability of porosity and clay content.

The findings of this study provide new insights into the geometry and evolution of particularly deformation clusters and coal entrainment in deformation bands. Never, to my knowledge, have dilational shear bands been reported in deformation band clusters and this study can contribute to the understand of the evolution of the geometric model and cluster formation. Coal entrainment has previously been reported in faults, but never been investigated under SEM in deformation bands. This study provides useful information on how coal is affected and deformed by deformation bands that can be used to gain insight into the role of coal in reservoirs.

8 Future work

- It would be interesting to do more work on the clay found in the samples in order to gain further understanding of the timing of the clay formation. X-ray diffraction (XRD) could be carried out to determine a more precise mineralogy of the clay and the sandstone, and more careful analysis of the clay can be done in the SEM in order to distinguish between allogenic and authigenic clay. A method could be developed in ImageJ or similar DIA-software to digitally remove the clay from the BSE-SEM images for the porosity to be measured without the presence of clay. Digital removal of clay was done for a few images for this study, but the method used is believed to be unprecise and time consuming. A more precise digital removal of authigenic clay would contribute to determine if the increased porosity in the deformation band clusters were due to preferential precipitation of clay in the host rock or due to kinematics of the bands.
- It is suggested that characterization of coal macerals can be useful to do in order to better understand how coal deforms in deformation bands. Macerals have previously been distinguished using fluorescence microscopy and Raman spectroscopy that can analyse the chemical structures of coal macerals. Characterization of coal macerals would be useful as this study has shown that they do deform differently and have various effect on porosity and permeability. Determining the vitrinite reflectance of the coal could also be done to know the rank of the coal.
- It was concluded that the coal for this study did not have a sealing effect similar to clay smear, but a few studies have reported otherwise. It would be interesting for future projects to study the microstructures of thicker coal seams in the SEM than the ones used for this study (1.2 mm thick) and determine the effect of thickness on porosity and permeability. Permeability measurements can also be carried out on both the coal and the deformation bands to investigate the total effect on fluid flow.

9 Bibliography

Adams, C., Campbell, H. and Griffin, W., 2009. Tracing the Caples Terrane through New Zealand using detrital zircon age patterns and radiogenic isotope signatures. *New Zealand Journal of Geology and Geophysics*, 52(3), pp.223-245.

Adams, C., Campbell, H., Mortimer, N. and Griffing, W., 2016. Perspectives on Cretaceous Gondwana break-up from detrital zircon provenance of southern Zealandia sandstones. *Geological Magazine*, 154(4), pp.661-682.

Ahmad, W. (2008) "Contrast in Clay Mineralogy and their Effect on Reservoir Properties in Sandstone Formations", Bull. Chem. Soc. Ethiopia. 22(1), Pp. 41–65.

Aitchison, J., Campbell, J. and Stilwell, J., 1993. Cretaceous/Tertiary geology and macropaleontology of the Waianakarua District, North Otago, New Zealand. *Journal of the Royal Society of New Zealand*, 23(1), pp.43-54.

Antonellini, M. and Aydin, A., 1994. Effect of Faulting on Fluid Flow in Porous Sandstones: Petrophysical Properties. *AAPG Bulletin*, 78.

Antonellini, M., Aydin, A. and Pollard, D., 1994. Microstructure of deformation bands in porous sandstones at Arches National Park, Utah. *International Journal of Rock Mechanics and Mining Sciences & Geomechanics Abstracts*, 31(6), p.276.

Antonellini, M.A., Aydin, A. & Orr, L. 1999. Outcrop aided characterization of a faulted hydrocarbon reservoir: Arroyo Grande oil field, California, USA. In: Haneberg, W.C., Mozley, P.S., Moore, C.J. & Goodwin, L.B. (eds) Faults and Subsurface Flu¨

Arostegui, J., 2001. Microtextures and the Origin of Muscovite-Kaolinite Intergrowths in Sandstones of the Utrillas Formation, Basque Cantabrian Basin, Spain. *Clays and Clay Minerals*, 49(6), pp.529-539.

Aydin, A. and Johnson, A., 1978. Development of faults as zones of deformation bands and as slip surfaces in sandstone. *Pure and Applied Geophysics PAGEOPH*, 116(4-5), pp.931-942.

Aydin, A. and Johnson, A., 1983. Analysis of faulting in porous sandstones. *Journal of Structural Geology*, 5(1), pp.19-31.

Aydin, A., 1978. Small faults formed as deformation bands in sandstone. *Pure and Applied Geophysics PAGEOPH*, 116(4-5), pp.913-930.

Aydin, A., Borja, R. and Eichhubl, P., 2006. Geological and mathematical framework for failure modes in granular rock. *Journal of Structural Geology*, 28(1), pp.83-98.

Ballance, P., 2009. *New Zealand geology: an illustrated guide*. Auckland: Geoscience Society of New Zealand.

Ballas, G., Fossen, H. and Soliva, R., 2015. Factors controlling permeability of cataclastic deformation bands and faults in porous sandstone reservoirs. *Journal of Structural Geology*, 76, pp.1-21.

Barrier, A., 2019. *Tectonics, sedimentation and magmatism of the Canterbury Basin, New Zealand*. PhD. University of Canterbury.

Baud, P., Schubnel, A. and Wong, T., 2000. Dilatancy, compaction, and failure mode in Solnhofen limestone. *Journal of Geophysical Research: Solid Earth*, 105(B8), pp.19289-19303.

Bésuelle, P., 2001. Evolution of strain localisation with stress in a sandstone: Brittle and semi-brittle regimes. *Physics and Chemistry of the Earth, Part A: Solid Earth and Geodesy*, 26(1-2), pp.101-106.

Billi, A. and Storti, F., 2004. Fractal distribution of particle size in carbonate cataclastic rocks from the core of a regional strike-slip fault zone. *Tectonophysics*, 384(1-4), pp.115-128.

Bishop, D., 1972. Progressive Metamorphism from Prehnite-Pumpellyite to Greenschist Facies in the Dansey Pass Area, Otago, New Zealand. *Geological Society of America Bulletin*, 83(11), p.3177.

Bishop, D.G., Turnbull, I.M. (compilers), 1996. Geology of the Dunedin area. Institute of Geological & Nuclear Sciences. Lower Hutt, New Zealand.

Blenkinsop, T., 1991. Cataclasis and processes of particle size reduction. *Pure and Applied Geophysics PAGEOPH*, 136(1), pp.59-86.

Bongers, G., Jackson, W. and Woskoboenko, F., 2000. Pressurised steam drying of Australian low-rank coals. *Fuel Processing Technology*, 64(1-3), pp.13-23.

Borradaile, G., 1981. Particulate flow of rock and the formation of cleavage. *Tectonophysics*, 72(3-4), pp.305-321.

Bradshaw, J., 1989. Cretaceous geotectonic patterns in the New Zealand Region. *Tectonics*, 8(4), pp.803-820.

Braathen, A., Petrie, E., Nystuen, T., Sundal, A., Skurtveit, E., Zuchuat, V., Gutierrez, M. and Midtkandal, I., 2020. Interaction of deformation bands and fractures during progressive strain in monocline - San Rafael Swell, Central Utah, USA. *Journal of Structural Geology*, 141, p.104219.

Campbell, H., and Landis, C. A., 2009. "New Zealand, Geology". *Encyclopedia of Islands*, edited by Rosemary Gillespie and David Clague, Berkley: University of California Press, pp. 673-680

Campbell, H., Mortimer, N. and Turnbull, I., 2003. Murihiku Supergroup, New Zealand: Redefined. *Journal of the Royal Society of New Zealand*, 33(1), pp.85-95.

Campbell, M., Rosenbaum, G., Allen, C. and Mortimer, N., 2020. Origin of dispersed Permian–Triassic fore-arc basin terranes in New Zealand: Insights from zircon petrochronology. *Gondwana Research*, 78, pp.210-227.

Carter, R., 1985. The Mid-Oligocene Marshall Paraconformity, New Zealand: Coincidence with Global Eustatic Sea-Level Fall or Rise?. *The Journal of Geology*, 93(3), pp.359-371.

Chen, L., Xu, J. and Chen, J., 2015. Applications of scanning electron microscopy in earth sciences. *Science China Earth Sciences*, 58(10), pp.1768-1778.

Cooper, R. and Tulloch, A., 1992. Early Palaeozoic terranes in New Zealand and their relationship to the Lachlan Fold Belt. *Tectonophysics*, 214(1-4), pp.129-144.

Cooper, R., 1989. New Zealand tectonostratigraphic terranes and panbiogeography. *New Zealand Journal of Zoology*, 16(4), pp.699-712.

Crampton, J., Mortimer, N., Bland, K., Strogen, D., Sagar, M., Hines, B., King, P. and Seebeck, H., 2019. Cretaceous termination of subduction at the Zealandia margin of Gondwana: The view from the paleo-trench. *Gondwana Research*, 70, pp.222-242.

Diessel, C., Boyd, R., Wadsworth, J., Leckie, D. and Chalmers, G., 2000. On balanced and unbalanced accommodation/peat accumulation ratios in the Cretaceous coals from Gates Formation, Western Canada, and their sequence-stratigraphic significance. *International Journal of Coal Geology*, 43(1-4), pp.143-186.

Dong, Z., Yu, W., Jia, T., Guo, S., Geng, W. and Peng, B., 2021. Experimental Study on the Variation of Surface Widths of Lignite Desiccation Cracks during Low-Temperature Drying. *ACS Omega*, 6(30), pp.19409-19418.

Du Bernard, X., Eichhubl, P. and Aydin, A., 2002. Dilation bands: A new form of localized failure in granular media. *Geophysical Research Letters*, 29(24), pp.29-1-29-4.

Elphick, K., Sloss, C., Regenauer-Lieb, K. and Schrank, C., 2021. Distribution, microphysical properties, and tectonic controls of deformation bands in the Miocene subduction wedge (Whakataki Formation) of the Hikurangi subduction zone. *Solid Earth*, 12(1), pp.141-170.

Fisher, Q.J. & Knipe, R.J. 2001. The permeability of faults within siliciclastic petroleum reservoirs of the North Sea and Norwegian Continental Shelf. Marine and Petroleum Geology, 18, 1063–1081

Forsyth , I'J .(compiler) 200 1: Geology of the Waitaki area. Institute of Geological & Nuclear Sciences 1:250 000 geological map 19. I sheet + 64p. Lower Hutt, New Zealand. lnstitute of Geological J & Nuclear Sciences Limited.

Fossen, H. and Bale, A., 2007. Deformation bands and their influence on fluid flow. *AAPG Bulletin*, 91(12), pp.1685-1700.

Fossen, H. and Hesthammer, J., 1997. Geometric analysis and scaling relations of deformation bands in porous sandstone. *Journal of Structural Geology*, 19(12), pp.1479-1493.

Fossen, H., 2010. *Structural geology*. Cambridge (UK): Cambridge University press.

Fossen, H., Schultz, R., Shipton, Z. and Mair, K., 2007. Deformation bands in sandstone: a review. *Journal of the Geological Society*, 164(4), pp.755-769.

Fossen, H., Soliva, R., Ballas, G., Trzaskos, B., Cavalcante, C. and Schultz, R., 2017. A review of deformation bands in reservoir sandstones: geometries, mechanisms and distribution. *Geological Society, London, Special Publications*, 459(1), pp.9-33.

Færseth, R., 2006. Shale smear along large faults: continuity of smear and the fault seal capacity. *Journal of the Geological Society*, 163(5), pp.741-751.

Gaina, C., Müller, D., Royer, J., Stock, J., Hardebeck, J. and Symonds, P., 1998. The tectonic history of the Tasman Sea: A puzzle with 13 pieces. *Journal of Geophysical Research: Solid Earth*, 103(B6), pp.12413-12433.

Gamson, P. D., Beamish B.B, and Johnson C, 1992. Coal Microstructure and Micropermeability and Their Effects on Natural Gas Recovery. *AAPG Bulletin*, 76.

Giannetta, L., Webb, N., Butler, S. and Grigsby, N., 2021. Using clay microporosity to improve formation evaluation in potential residual oil zones: Cypress Sandstone, Illinois Basin. *AAPG Bulletin*, 105(8), pp.1595-1625.

Greb S.F., Eble, C.F., Hower J.C (2017) Coal. In: White W. (eds) Encyclopedia of Geochemistry. Encyclopedia of Earth Sciences Series. Springer

Hadizadeh, J. and Johnson, W., 2003. Estimating local strain due to comminution in experimental cataclastic textures. *Journal of Structural Geology*, 25(11), pp.1973-1979.

Harrington, H., 1958. *Geology of Kaitangata Coalfield*. Wellington: Government Printer.

Hesthammer, J. and Fossen, H., 2001. Structural core analysis from the Gullfaks area, northern North Sea. *Marine and Petroleum Geology*, 18(3), pp.411-439.

Hesthammer, J., Bjørkum, P.A. & Watts, L.I. 2002. The effect of temperature on sealing capacity of faults in sandstone reservoirs: examples from the Gullfaks and Gullfaks Sør fields, North Sea. AAPG Bulletin, 86, 1733–1751.

Higgs, K., Browne, G. and Sahoo, T., 2019. Reservoir characterisation of syn-rift and post-rift sandstones in frontier basins: An example from the Cretaceous of Canterbury and Great South basins, New Zealand. *Marine and Petroleum Geology*, 101, pp.1-29.

Hong, D., Cao, J., Wu, T., Dang, S., Hu, W. and Yao, S., 2020. Authigenic clay minerals and calcite dissolution influence reservoir quality in tight sandstones: Insights from the central Junggar Basin, NW China. *Energy Geoscience*, 1(1-2), pp.8-19.

Howard, J. J., 1992. Influence of authigenic-clay minerals on permeability, in Origin, Diagenesis, and Petrophysics of Clay Minerals in Sandstones, edited by D. W. Houseknecht and E. D. Pittman, Spec. Publ. SEPM, 47, 257-264,

Hurst, A. and Irwin, H., 1982. Geological modelling of clay diagenesis in sandstones. *Clay Minerals*, 17(1), pp.5-22.

Ibrahim, Y. and Padmanabhan, E., 2019. Thermally - Induced Fractures in Coal, Balingian Province, Sarawak, Malaysia. *2018 AAPG International Conference and Exhibition,. Industrial Research, pp. 11.* Int. J. Coal Geol., 219

Kamp, P.J.J., Vincent, K.A. & Tayler, M.J.S. (2015): Cenozoic sedimentary and volcanic rocks of New Zealand: A reference volume of lithology, age and paleoenvironments with maps (PMAPs) and database. University of Waikato, Hamilton, New Zealand. 335 p.

Kelly, P., Peacock, D., Sanderson, D. and McGurk, A., 1999. Selective reverse-reactivation of normal faults, and deformation around reverse-reactivated faults in the Mesozoic of the Somerset coast. *Journal of Structural Geology*, 21(5), pp.493-509.

Kimbrough, D., Mattinson, J., Coombs, D., Landis, C. and Johnston, M., 1992. Uranium-lead ages from the Dun Mountain ophiolite belt and Brook Street terrane, South Island, New Zealand. *Geological Society of America Bulletin*, 104(4), pp.429-443.

Kula, J., Tulloch, A., Spell, T. and Wells, M., 2007. Two-stage rifting of Zealandia-Australia-Antarctica: Evidence from 40Ar/39Ar thermochronometry of the Sisters shear zone, Stewart Island, New Zealand. *Geology*, 35(5), p.411.

Laird, M. and Bradshaw, J., 2004. The Break-up of a Long-term Relationship: the Cretaceous Separation of New Zealand from Gondwana. *Gondwana Research*, 7(1), pp.273-286.

Litchfield, N. and Norris, R., 2000. Holocene motion on the Akatore Fault, south Otago coast, New Zealand. *New Zealand Journal of Geology and Geophysics*, 43(3), pp.405-418.

Litchfield, N., 2000. *Quaternary deformation at the leading edge of the Otago reverse fault province*. PhD. University of Otago.

Litchfield, N., 2001. The Titri Fault System: Quaternary-active faults near the leading edge of the Otago reverse fault province. *New Zealand Journal of Geology and Geophysics*, 44(4), pp.517-534.

Lomas, S., 2003. An assesment of basin development and coal rank in the Kaitangata Coalfield, South Otago, New Zealand. *PhD*. University of Canterbury.

Lommatzsch, M., Exner, U., Gier, S. and Grasemann, B., 2015. Dilatant shear band formation and diagenesis in calcareous, arkosic sandstones, Vienna Basin (Austria). *Marine and Petroleum Geology*, 62, pp.144-160.

Luyendyk, B., 1995. Hypothesis for Cretaceous rifting of east Gondwana caused by subducted slab capture. *Geology*, 23(4), p.373.

Maciel, I., Dettori, A., Balsamo, F., Bezerra, F., Vieira, M., Nogueira, F., Salvioli-Mariani, E. and Sousa, J., 2018. Structural Control on Clay Mineral Authigenesis in Faulted Arkosic Sandstone of the Rio do Peixe Basin, Brazil. *Minerals*, 8(9), p.408.

MacKinnon T 1983. Origin of the Torlesse terrane and coeval rocks, South Island, New Zealand. Geological Society of America Bulletin 94: 967-985.

Mair, K., Main, I. and Elphick, S., 2000. Sequential growth of deformation bands in the laboratory. *Journal of Structural Geology*, 22(1), pp.25-42.

Marone, C. and Scholz, C., 1989. Particle-size distribution and microstructures within simulated fault gouge. *Journal of Structural Geology*, 11(7), pp.799-814.

Matthews, A., 2003. *Small-scale faulting and fault sealing in Taratu Formation, Coastal Otago*. MSc thesis. University of Otago.

McCabe, P.J. (1984). Depositional Environments of Coal and Coal-Bearing Strata. In Sedimentology of Coal and Coal-Bearing Sequences (eds R.A. Rahmani and R.M. Flores).

Michael D. Wilson, Edward D. Pittman, 1977. Authigenic Clays in Sandstones: Recognition and Influence on Reservoir Properties and Paleoenvironmental Analysis. *SEPM Journal of Sedimentary Research*, Vol. 47.

Moore, T., and Li, Z., 2006. Controls on the formation of an anomalously thick Cretaceous-age coal mire. Special Paper of the Geological Society of America. 399. 269-290.

Mortimer, N., 2003. A provisional structural thickness map of the Otago Schist, New Zealand. *American Journal of Science*, 303(7), pp.603-621.

Mortimer, N., 2004. New Zealand's Geological Foundations. *Gondwana Research*, 7(1), pp.261-272.

Mortimer, N., Rattenbury, M., King, P., Bland, K., Barrell, D., Bache, F., Begg, J., Campbell, H., Cox, S., Crampton, J., Edbrooke, S., Forsyth, P., Johnston, M., Jongens, R., Lee, J., Leonard, G., Raine, J., Skinner, D., Timm, C., Townsend, D., Tulloch, A., Turnbull, I. and Turnbull, R., 2014. High-level stratigraphic scheme for New Zealand rocks. *New Zealand Journal of Geology and Geophysics*, 57(4), pp.402-419.

Mortimer, N., van den Bogaard, P., Hoernle, K., Timm, C., Gans, P., Werner, R. and Riefstahl, F., 2019. Late Cretaceous oceanic plate reorganization and the breakup of Zealandia and Gondwana. *Gondwana Research*, 65, pp.31-42.

Nicol, A., Childs, C., Walsh, J. and Schafer, K., 2013. A geometric model for the formation of deformation band clusters. *Journal of Structural Geology*, 55, pp.21-33.

Norris, R. and Cooper, A., 1995. Origin of small-scale segmentation and transpressional thrusting along the Alpine fault, New Zealand. *Geological Society of America Bulletin*, 107(2), p.231.

Ogilvie, S., Orribo, J. and Glover, P., 2001. The influence of deformation bands upon fluid flow using profile permeametry and positron emission tomography. *Geophysical Research Letters*, 28(1), pp.61-64.

O'Keefe, J., Bechtel, A., Christanis, K., Dai, S., DiMichele, W., Eble, C., Esterle, J., Mastalerz, M., Raymond, A., Valentim, B., Wagner, N., Ward, C. and Hower, J., 2013. On the fundamental difference between coal rank and coal type. *International Journal of Coal Geology*, 118, pp.58-87.

Olav Walderhaug (2), 1996. Kinetic Modeling of Quartz Cementation and Porosity Loss in Deeply Buried Sandstone Reservoirs. *AAPG Bulletin*, 80.

Peter R. King (2000) Tectonic reconstructions of New Zealand: 40 Ma to the Present, New Zealand. Journal of Geology and Geophysics, 43:4, 611-638,

Philit, S., Soliva, R., Castilla, R., Ballas, G., and Taillefer, A. (2018). Clusters of Cataclastic Deformation Bands in Porous Sandstones. *Journal Structural Geology*. 114, 235–250.

Pickel, W., Kus, J., Flores, D., Kalaitzidis, S., Christanis, K., Cardott, B., Misz-Kennan, M., Rodrigues, S., Hentschel, A., Hamor-Vido, M., Crosdale, P. and Wagner, N., 2017. Classification of liptinite – ICCP System 1994. *International Journal of Coal Geology*, 169, pp.40-61.

Pole, M., 1994. An Eocene Macroflora From the Taratu Formation at Livingstone, North Otago, New Zealand. *Australian Journal of Botany*, 42(3), p.341.

Psyrillos, A., 1999. Geological Controls on Kaolin Particle Shape and Consequences for Mineral Processing. *Clay Minerals*, 34(1), pp.193-208.

Rawling, G. and Goodwin, L., 2003. Cataclasis and particulate flow in faulted, poorly lithified sediments. *Journal of Structural Geology*, 25(3), pp.317-331.

Robertson, A., Campbell, H., Johnston, M. and Mortimer, N., 2019. Chapter 1 Introduction to Paleozoic–Mesozoic geology of South Island, New Zealand: subduction-related processes adjacent to SE Gondwana. *Geological Society, London, Memoirs*, 49(1), pp.1-14.

Robertson, A., Campbell, H., Johnston, M. and Palamakumbra, R., 2019. Chapter 15 Construction of a Paleozoic–Mesozoic accretionary orogen along the active continental margin of SE Gondwana (South Island, New Zealand): summary and overview. *Geological Society, London, Memoirs*, 49(1), pp.331-372.

Rong, L., Xiao, J., Wang, X., Sun, J., Jia, F. and Chu, M., 2020. Low-rank coal drying behaviors under negative pressure: Thermal fragmentation, volume shrinkage and changes in pore structure. *Journal of Cleaner Production*, 272, p.122572.

Rotevatn, A., Sandve, T., Keilegavlen, E., Kolyukhin, D. and Fossen, H., 2013. Deformation bands and their impact on fluid flow in sandstone reservoirs: the role of natural thickness variations. *Geofluids*, 13(3), pp.359-371.

Rotevatn, A., Torabi, A., Fossen, H. and Braathen, A., 2008. Slipped deformation bands: A new type of cataclastic deformation bands in Western Sinai, Suez rift, Egypt. *Journal of Structural Geology*, 30(11), pp.1317-1331.

S. Dai, A. Bechtel, C.F. Eble, R.M. Flores, D. French, I.T. Graham, J.M.K. O'Keefe., 2021. Recognition of peat depositional environments in coal: a review. Int. J Coal Geol. 94, 3-21

Sahoo, T., Nicol, A., Browne, G. and Strogen, D., 2020. Evolution of a Normal Fault System Along Eastern Gondwana, New Zealand. *Tectonics*, 39(10).

Sammis, C., King, G. and Biegel, R., 1987. The kinematics of gouge deformation. *Pure and Applied Geophysics PAGEOPH*, 125(5), pp.777-812.

Sarkisyan, S., 1972. Origin of authigenic clay minerals and their significance in petroleum geology. *Sedimentary Geology*, 7(1), pp.1-22.

Scott, A., 2002. Coal petrology and the origin of coal macerals: a way ahead?. *International Journal of Coal Geology*, 50(1-4), pp.119-134.

Shipton, Z. and Cowie, P., 2001. Damage zone and slip-surface evolution over μm to km scales in high-porosity Navajo sandstone, Utah. *Journal of Structural Geology*, 23(12), pp.1825-1844.

Sivrikaya, O., 2014. Cleaning study of a low-rank lignite with DMS, Reichert spiral and flotation. *Fuel*, 119, pp.252-258.

Souvick, S., and Steve Co., "Coaly Sandstones: Reservoir Evaluation Problems and Solutions." Paper presented at the SPE Asia Pacific Oil and Gas Conference and Exhibition, Jakarta, Indonesia, April 2001.

Souvick, S., and Steve, C., (2001). Coaly Sandstones: Reservoir Evaluation Problems and Solutions.

Sternlof, K., Karimi-Fard, M., Pollard, D. and Durlofsky, L., 2006. Flow and transport effects of compaction bands in sandstone at scales relevant to aquifer and reservoir management. *Water Resources Research*, 42(7).

Strogen, D., Seebeck, H., Nicol, A. and King, P., 2017. Two-phase Cretaceous–Paleocene rifting in the Taranaki Basin region, New Zealand; implications for Gondwana break-up. *Journal of the Geological Society*, 174(5), pp.929-946.

Sun, Q., 2002. The variation of structural characteristics of macerals during pyrolysis⋆. *Fuel*, 82(6), pp.669-676.

Sun, W., Andrade, J., Rudnicki, J. and Eichhubl, P., 2011. Connecting microstructural attributes and permeability from 3D tomographic images of in situ shear-enhanced compaction bands using multiscale computations. *Geophysical Research Letters*, 38(10), p.n/a-n/a.

Sutherland, R., 1995. The Australia-Pacific boundary and Cenozoic plate motions in the SW Pacific: Some constraints from Geosat data. *Tectonics*, 14(4), pp.819-831.

Suuberg, E., Otake, Y., Yun, Y. and Deevi, S., 1993. Role of moisture in coal structure and the effects of drying upon the accessibility of coal structure. *Energy & Fuels*, 7(3), pp.384-392.

Svensen, H., Torsvik, T., Callegaro, S., Augland, L., Heimdal, T., Jerram, D., Planke, S. and Pereira, E., 2017. Gondwana Large Igneous Provinces: plate reconstructions, volcanic basins and sill volumes. *Geological Society, London, Special Publications*, 463(1), pp.17-40.

Teichmüller, M., 1987. Recent advances in coalification studies and their application to geology. *Geological Society, London, Special Publications*, 32(1), pp.127-169.

Thakur, N. and Rajput, S., 2016. *Geological Controls for Gas Hydrates and Unconventionals*. Elsevier.

Thomas, L., 2012. *Coal geology*. Wiley and Sons, Incorporated.

Thorsheim, E. (2015). The geometry and evolution of deformation bands in carbonate grainstones along the Maghlaq fault, Malta. *Msc thesis*, University of Bergen.

Torabi, A. and Fossen, H., 2009. Spatial variation of microstructure and petrophysical properties along deformation bands in reservoir sandstones. *AAPG Bulletin*, 93(7), pp.919-938.

Torabi, A., Braathen, A., Cuisiat, F. and Fossen, H., 2007. Shear zones in porous sand: Insights from ring-shear experiments and naturally deformed sandstones. *Tectonophysics*, 437(1-4), pp.37-50.

Torabi, A., Fossen, H. and Braathen, A., 2013. Insight into petrophysical properties of deformed sandstone reservoirs. *AAPG Bulletin*, 97(4), pp.619-637.

Tulloch, A., Mortimer, N., Ireland, T., Waight, T., Maas, R., Palin, J., Sahoo, T., Seebeck, H., Sagar, M., Barrier, A. and Turnbull, R., 2019. Reconnaissance Basement Geology and Tectonics of South Zealandia. *Tectonics*, 38(2), pp.516-551.

Twiss, R.J. and Moores, E.M. (1992) Structural Geology. W.H. Freeman and Company, New York, 532.

Vajdova, V., Baud, P. and Wong, T., 2004. Compaction, dilatancy, and failure in porous carbonate rocks. *Journal of Geophysical Research: Solid Earth*, 109(B5).

van der Meer, Q., Waight, T., Scott, J. and Münker, C., 2017. Variable sources for Cretaceous to recent HIMU and HIMU-like intraplate magmatism in New Zealand. *Earth and Planetary Science Letters*, 469, pp.27-41.

Vranjes, S., Misch, D., Schöberl, T., Kiener, D., Gross, D. and Sachsenhofer, R., 2018. Nanoindentation study of macerals in coals from the Ukrainian Donets Basin. *Advances in Geosciences*, 45, pp.73-83.

Vrolijk, P., Urai, J. and Kettermann, M., 2016. Clay smear: Review of mechanisms and applications. *Journal of Structural Geology*, 86, pp.95-152.

Wallace, L., Barnes, P., Beavan, J., Van Dissen, R., Litchfield, N., Mountjoy, J., Langridge, R., Lamarche, G. and Pondard, N., 2012. The kinematics of a transition from subduction to strike-slip: An example from the central New Zealand plate boundary. *Journal of Geophysical Research: Solid Earth*, 117(B2),

Wanas, H. and Soliman, H., 2001. Allogenic and authigenic clays of the Lower Palæozoic sandstones of the Naqus Formation at Gebel Gunna, central Sinai, Egypt: their recognition and geological significance. *Journal of African Earth Sciences*, 32(1), pp.47-60.

Wandres, A. and Bradshaw, J., 2005. New Zealand tectonostratigraphy and implications from conglomeratic rocks for the configuration of the SW Pacific margin of Gondwana. *Geological Society, London, Special Publications*, 246(1), pp.179-216.

Wandres, A., 2004. Provenance of the sedimentary Rakaia sub-terrane, Torlesse Terrane, South Island, New Zealand: the use of igneous clast compositions to define the source. *Sedimentary Geology*,.

Ward, C.R., Li, Z.S., French, D., 2005. Geological sources of metals in coal and coal products. In: Moore, T.A., Black, A., Centeno, J., Harding, J., Trumm, D. (Eds.), Metal Contaminants in New Zealand, Resolutionz Press, Christchurch, New Zealand, pp. 49–79.

Xie, K.-C. Coal Pyrolysis Reactions. *Structure and Reactivity of Coal* 2015, 119– 179

Zhang, H., Cen, K., Yan, J. and Ni, M., 2002. The fragmentation of coal particles during the coal combustion in a fluidized bed. *Fuel*, 81(14), pp.1835-1840.

Zhou, W., Apkarian, R., Wang, Z., and Joyd, D., 2007, Fundamentals of Scanning Electron Microscopy (SEM), *in* Zhou, W., and Wang, Z., eds., *Scanning Microscopy for Nanotechnology*, Springer New York, p. 1-40.

10 Appendix

Porosity measurements

Table 10.1: Porosity measurements of both host rock and deformation band in each sample.

Sample ID	*Location*	*Magnification*	*Porosity*
W1-06	DB	110	11.96
W1-09	DB	130	11.92
W1-10	DB	130	10.55
W1-11	DB	130	13.93
W1-12	HR	131	10.89
W1-13	HR	131	17.14
W1-16	HR	130	11.34
W1-17	HR	130	14.74
W1-19	DB	130	11.47
W2-01	DB	130	22.02
W2-03	DB	130	26.83
W2-04	HR	130	13.35
W2-06	HR	399	13.38
W2-08	HR	133	17.24
W2-09	HR	133	15.64
W2-12	DB	130	16.94
W2-15	DB	131	34.72
W2-16	DB	131	34.01
W2-17	DB	118	13.66
W2-18	HR	130	20.62
W3-01	DB	128	19.99
W3-02	DB	130	23.74
W3-03	DB	130	22.58
W3-04	HR	130	15.43
W3-05	HR	130	21.8
W3-06	DB	130	23.45
W3-07	DB	133	24.71
W3-10	DB	130	21.14
W4-02	DB	115	22.46
W4-04	DB	115	29.85
W4-05	DB	115	23.89
W4-06	DB	115	31.44
W4-07	DB	130	29.64
W4-08	DB	135	33.41
W4-11	DB	113	31.12
W4-12	HR	123	30.65
W4-15	HR	105	35.08
W4-16	DB	130	23.7
W4-17	DB	130	28.02
W4-18	HR	130	27.92
W4-19	HR	130	27.19
W4-20	DB	130	18.69
W5-08	DB	131	23.65
W5-13	HR	131	15.8
W5-36	HR	131	13.35
W5-37	DB	131	23.34
W6-07	DB	130	21.818

Sample ID	Location	Magnification	Porosity
W6-10	DB	130	19.02
W6-11	DB	130	16.45
W6-12	HR	130	16.84
W6-15	HR	131	18.13
W6-17	HR	131	17.51
W6-18	HR	131	17.05
W6-19	HR	130	17.46
W6-20	HR	130	17.11
W6-21	DB	130	15.09
W7-09	HR	130	21.13
W7-10	DB	130	17.33
W7-11	HR	130	21.17
W7-14	HR	128	18.29
W7-15	HR	128	23.18
W7-16	DB	128	41.5
W7-20	HR	130	22.36
W7-21	HR	130	38.88
W7-22	HR	130	41.5
W7-27	HR	130	38.03
W7-28	HR	130	24.9
W7-29	DB	130	34.9
W10-21	DB	131	21.12
W10-25	HR	139	27.5
W10-35	DB	131	22.15
W10-37	HR	139	34.55
W10-45	DB	131	20.45
W11-14	HR	130	22.41
W11-15	HR	130	11.88
W11-16	DB	130	21.01
W11-17	DB	130	16.61
W11-18	DB	130	17.57
W11-21	DB	130	18.15
W11-25	DB	130	19.53
W11-26	HR	130	14.4
W11-27	HR	130	25.68
W11-28	HR	130	15.11
W11-29	HR	130	25.16
W11-33	HR	130	22.02
W12-01	HR	130	18.37
W12-03	HR	149	21.96
W12-09	DB	131	19.03
W12-12	DB	130	24.88
W12-13	DB	130	16.51
W12-15	HR	130	16.3
W12-16	HR	130	10.57
W12-17	HR	130	26.85
W12-18	HR	130	19.49
W13-01	DB	130	18.52
W13-05	DB	131	21.75
W13-06	DB	131	15.19
W13-07	DB	130	23.06
W13-09	DB	130	17.54
W13-10	HR	130	20.4
W13-13	HR	130	24.87
W13-14	HR	130	20.02
W13-15	HR	130	19.71
W13-16	HR	130	23.19
W13-17	DB	130	12.16

Sample ID	Location	Magnification	Porosity
W14-04	DB	151	12.8
W14-08	DB	151	17.06
W14-18	DB	131	19.03
W14-28	HR	131	24.43
W14-29	HR	131	24.81
W14-32	HR	129	23.45
W14-34	DB	131	15.37
W15-02	DB	130	16.45
W15-04	HR	133	17.07
W15-06	HR	130	18.22
W15-07	DB	128	17.64
W15-09	DB	130	15.9
W16-14	DB	154	24.3
W16-17	DB	130	22.93
W16-18	DB	130	22.45
W16-19	DB	130	21.44
W16-20	HR	130	24.8
W16-21	HR	130	30.9
W16-24	HR	131	25.93
W16-25	HR	131	26.06
W16-26	HR	131	24.01
W16-27	DB	131	17.16
W17-11	HR	130	15.12
W17-12	HR	130	21.11
W17-15	HR	130	18.44
W17-16	HR	130	17.67
W17-17	HR	130	16.67
W17-19	DB	131	15.24
W17-22	DB	130	14.63
W17-23	DB	130	11.02
W17-24	DB	130	14.84
W17-41	HR	130	32.09
W17-42	HR	130	22.26
W18-17	DB	130	27.97
W18-20	DB	130	33.56
W18-21	DB	130	28.07
W18-22	DB	130	34.23
W18-23	HR	130	16.65
W18-24	HR	130	18.77
W18-28	HR	107	17.78
W18-29	HR	131	33
W18-30	DB	131	23.24
W18-31	HR	131	30.67